

**SYNTHESIS OF MODIFIED ZINC OXIDE NANOPARTICLES
USING PNEUMATIC SPRAY PYROLYSIS FOR SOLAR CELL
APPLICATION**

BY

LUYOLO NTOZAKHE

201006908

**A dissertation submitted in fulfilment of the requirements for the
award of the degree of**

MASTERS OF SCIENCE

IN

CHEMISTRY

Faculty of Science and Agriculture

University of Fort Hare

Supervisor: Dr. David M. Katwire

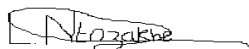
Co-supervisor: Prof. Edson L. Meyer

Co-supervisor: Dr. Raymond T. Taziwa

JANUARY 2017

DECLARATION

I, *Luyolo Ntozakhe* declare that “SYNTHESIS OF MODIFIED ZINC OXIDE NANOPARTICLES USING PNEUMATIC SPRAY PYROLYSIS FOR SOLAR CELL APPLICATION” is my own work, submitted in fulfilment for a Master of Science (MSc) degree in the Department of Chemistry at the University of Fort Hare. I further declare that this work has not been submitted in any other institution of higher learning and all the sources cited or quoted are indicated and acknowledged by means of complete references.



Signature.....

31-03-2017

Date.....

DEDICATION

This thesis is dedicated to the lovely memories of the late Masiguba Ji (1934/06/29-2015/01/23) and Hlumelo Silinga (2015/06/03-2015/06/06).



Signature.....

31-03-2017

Date.....

ACKNOWLEDGEMENTS

First and foremost, I would like to thank God Almighty for the gift of life, and for giving me courage and strength during these years.

I would like to express my special appreciation and thanks to my supervisors, Dr D.M Katwire, Department of Chemistry; Prof. E. L Meyer, Fort Hare Institute of Technology (FHIT); and Dr R. T Taziwa, Department of Chemistry and Fort Hare Institute of Technology (FHIT) for their research guidance, encouragements, and support during this work. Without their supervision and constant help this research would not have been possible.

My gratitude also goes to the Department of Chemistry and Fort Hare Institute of Technology (FHIT) for providing me with the chemicals and other equipment required to conduct this research. Many thanks also go to all research group members (Photovoltaic research group) at Fort Hare Institute of Technology for their support.

My special thanks goes to Dr R. T Taziwa (Chemistry Department and Fort Hare Institute of Technology, UFH) and Mr K. Tshapu (Chemistry Department, UFH) for technical assistance in Raman spectroscopy measurements and X-ray diffraction, respectively. Many thanks go to the DST/CSIR Nanotechnology Innovation Centre, National Centre for Nanostructured Materials, CSIR and Electron Microscope Unit, University of Cape Town for providing technical support.

Last but not least, my appreciation goes to South African National Research Foundation (NRF), Govani Beki Research and Development Centre (GMRDC) of the University of Fort Hare and Sasol Inzalo Foundation for their financial support. Without their assistance none of this would have been possible.

ABSTRACT

In this work, the pneumatic spray pyrolysis was used to synthesize un-doped and carbon doped zinc oxide (ZnO) nanoparticles. The zinc acetate, tetrabutylammonium bromide and ethanol were used as starting materials for the desired ZnO nanoparticles and the prepared samples were annealed at 400 °C in the furnace. The as synthesized un-doped and carbon doped ZnO NPs were evaluated using X-ray diffraction (XRD), Scanning electron microscope (SEM), Energy dispersive x-ray spectroscopy (EDX), High-resolution transmission electron microscopy (HRTEM), Raman spectroscopy (RS) and Ultraviolet-visible spectroscopy (UV-Vis). XRD analysis of the synthesized NPs revealed peaks at 31.90°, 34.50°, 36.34°, 47.73°, 56.88°, 63.04°, 68.20°, and 77.33° belonging to the hexagonal Wurtzite ZnO crystal structure. The incorporation of C species into ZnO lattice was cross examined by monitoring the peak positions of the (100), (002) and (001) planes. These three main peaks of C-ZnO NPs show a peak shift to higher 2θ values which indicates substitutional carbon doping in ZnO NPs. SEM analysis has revealed that the as synthesized NPs have spherical shape and the morphology of the NPs change as the concentration of carbon increases. The EDX spectra of both un-doped and doped ZnO nanoparticles have revealed prominent peaks at 0.51 keV, 1.01 keV, 1.49 keV, 8.87 keV and 9.86 keV. Peaks at X-ray energies of 0.51 keV and 1.01 keV respectively represent the emissions from the K-shell of oxygen and L-shell of zinc. The L-shell emission at 1.01 keV is considered as convolution of Zn 2p_{3/2} and Zn 2p_{1/2} photoelectron energies. The occurrence of these peaks in the EDX endorses the existence of Zn and O atoms in the PSP prepared samples. HRTEM analysis has revealed NPs size modal range from 6.65-14.21 nm for the PSP synthesized samples which is in mutual agreement with the XRD data calculated values. Moreover the selected area diffraction images displaying the fact that only the diffraction planes of (101), (002) and (100) are responsible for the diffraction pattern belonging to Wurtzite ZnO. RS analysis has revealed that the un-doped ZnO and doped ZnO samples have characteristic Raman vibration modes at 325 cm⁻¹, and 434 cm⁻¹ belonging to Wurtzite ZnO structure. Moreover, the prominent peak at 434 cm⁻¹ which is the characteristic peak of E₂⁽²⁾ (high) mode of the Wurtzite ZnO and the E₂⁽²⁾ (high) has been red shifted by 4 cm⁻¹, as compared to that found in the bulk ZnO. Additionally, the effect of carbon doping through Raman spectroscopy peak shifts of the E₂⁽²⁾ (high) mode, A₁(LO) mode and multi-phonon has also been considered and discussed in detail. UV-Vis diffuse reflectance spectroscopy has revealed a red shift of the absorption edge with increase in C doping. Finally, the effect of

nano-crystallite size and gradual prominence of C into ZnO lattice due to increase in C doping concentration in the PSP prepared nanoparticles was meticulously elaborated through Raman Spectroscopy analysis.

Key words: Spray pyrolysis, ZnO Nanoparticles, Dye sensitized solar cells, Doping

PREFACE

In the past decades, there has been a major shift away from pursuing conventional fossil fuel energy sources. Previous studies have revealed that fossil fuels are responsible for a host of environmental problems for example, releasing carcinogenic substances into the air and emitting greenhouse gases into the atmosphere. Another motivation behind why this shift has occurred is because conventional sources of fossil fuels are finite and non-renewable. Once all the remaining investments start to diminish, they will no longer be able to keep up with the current demand of energy consumption. As a result of this approaching energy crisis, various renewable energy sources have been investigated as alternatives to fossil fuels. One of these promising sources is solar energy, the collection of solar radiation by means of solar panels which convert the energy into electricity. Solar energy is a promising alternative source of energy because it is readily available and inexhaustible. The solar energy technologies have emerged as a better method for minimizing environmental problems as well as economic cost in the field of renewable energy.

Zinc oxide (ZnO) presents a remarkable material system for investigation due to its wide band gap ($E_g = 3.37$ eV) with a high exciton binding energy (60 meV). More particularly, ZnO semiconductor nanostructures have attracted considerable interest during the past decades in terms of new technological applications, mainly because of the unique properties observed at nanoscale. Nano-sized ZnO has been intensively studied because of its unique advantages, such as its high photosensitivity, nontoxic nature, large bandgap, and presents a low cost material for solar cell electrodes. Moreover, synthesis of ZnO is more cost effective than other various alternative semiconductors such as III-V semiconductors. Its low price compared with other wide band semiconductor nanomaterials makes it a good candidate for industrial applications. Therefore, the present study deals with the development of spray pyrolysis technique for preparation of carbon doped zinc oxide nanoparticles for solar cell applications.

This study relies on the excellent structural, morphological and optical properties of ZnO nanoparticles synthesized by pneumatic spray pyrolysis. The structure of this thesis is presented as follows: *Chapter 1* provides a general summary of the work done in the present study. An overview of the physical, optical, structural and morphological properties as well as the theoretical background of the pneumatic spray pyrolysis technique and models governing the

droplet formation in the PSP technique are presented in the literature in *Chapter 2*. *Chapter 3* outlines the experimental methodologies as well as an overview of the research techniques used for the synthesis of ZnO nanostructures. *Chapter 4* gives a brief background on the characterization techniques used in the study. *Chapter 5* reveals the results and discussion of the synthesized material. *Chapter 6* concludes the findings of this work and highlights suggestions for future work. Lastly the appendix presents the research outputs of the study which include oral and poster presentations in local conferences as well as future presentations that are going to be attended.

TABLE OF CONTENTS

DECLARATION	ii
DEDICATION	iii
ACKNOWLEDGEMENTS	iv
ABSTRACT	v
PREFACE	vii
LIST OF SYMBOLS	xiii
ACRONYMS	xiv
CHAPTER 1	1
INTRODUCTION	1
1.1. OVERVIEW	1
1.2. SOLAR CELLS	3
1.3. SPRAY PYROLYSIS	4
1.4. ZINC OXIDE	4
1.5. PROBLEM STATEMENT	5
1.5. RATIONALE AND MOTIVATION	6
1.6. AIMS AND OBJECTIVES	6
1.6.1. AIMS	6
1.6.2. OBJECTIVES	6
1.7. RESEARCH QUESTIONS	7
1.8. REFERENCES	8
CHAPTER 2	12
LITERATURE REVIEW	12
2.1. OVERVIEW	12
2.2. STRUCTURAL AND OPTO-ELECTRICAL PROPERTIES OF ZINC OXIDE ...	12
2.3. CRYSTAL STRUCTURE	14
2.4. DOPING	17

2.5.	LATTICE PARAMETERS.....	18
2.6.	APPLICATIONS	20
2.7.	ZINC OXIDE NANOSTRUCTURES	21
2.8.	ZINC OXIDE DEPOSITION METHODS	23
2.8.1.	CHEMICAL VAPOUR DEPOSITION.....	24
2.8.2.	SOL-GEL TECHNIQUE	27
2.8.3.	PLASMA ENHANCED CHEMICAL VAPOR DEPOSITION	31
2.8.4.	LASER ABLATION	31
2.9.	SPRAY PYROLYSIS	33
2.10.	PNEUMATIC SPRAY PYROLYSIS SYSTEM.	34
2.10.1	SPRAY PYROLYSIS VESSEL	35
2.10.2	SPRAY REACTOR (SPLIT TUBE FURNACE)	36
2.10.3	DESIGN OF A SUBSTRATE HOLDER.....	37
2.11.	PYROLYSIS OF ZINC OXIDE.....	39
2.12.	REACTION MECHANISMS FOR PRODUCTION OF ZINC OXIDE NANOPARTICLES.....	41
2.13.	PRECURSOR.....	43
2.14.	PNEUMATIC SPRAY PYROLYSIS MECHANISMS.....	43
2.14.1	CAPILLARY WAVE MECHANISM.....	46
2.14.2	CAVITATION MECHANISM	49
2.15.	CONCLUSION	51
2.16.	REFERENCES	52
CHAPTER 3	57
METHODOLOGY	57
3.1.	INTRODUCTION.....	57
3.2.	EXPERIMENTAL	57
3.2.1.	REAGENTS AND RAW MATERIALS.....	57
3.2.2.	SUBSTRATE CLEANING PROCEDURE	59
3.3.	OPERATION OF THE PSP SYSTEM.....	59
3.4.	PROCEDURE.....	62

3.4.1.	SYNTHESIS OF UN-DOPED ZINC OXIDE NANOPARTICLES	62
3.4.2.	SYNTHESIS OF DOPED ZINC OXIDE NANOPARTICLES	63
3.5.	CHARACTERIZATION OF ZINC OXIDE NANOPARTICLES.....	65
3.5.1.	X-RAY DIFFRACTION ANALYSIS	65
3.5.2.	SCANNING ELECTRON MICROSCOPY (SEM).....	67
3.5.3.	ENERGY DISPERSIVE X-RAY SPECTROSCOPY (EDS or EDX)	69
3.5.4.	HIGH RESOLUTION TRANSMISSION ELECTRON MICROSCOPE (HRTEM)	70
3.5.5.	RAMAN SPECTROSCOPY (RS)	72
3.5.6.	ULTRAVIOLET VISIBLE SPECTROSCOPY (UV-VIS)	74
3.5.7.	DIFFUSE REFLECTANCE SPECTROSCOPY (DRS).....	76
3.6.	CONCLUSION	78
3.7.	REFERENCES.....	79
CHAPTER 4	81
RESULTS AND DISCUSSION	81
4.1.	INTRODUCTION.....	81
4.2.	STRUCTURAL CHARACTERIZATION	81
4.2.1.	X-RAY DIFFRACTION ANALYSIS	81
4.2.2.	SCANNING ELECTRON MICROSCOPY (SEM)	88
4.2.3.	HIGH RESOLUTION TRANSMISSION ELECTRON MICROSCOPE (HRTEM).....	94
4.2.4.	RAMAN SPECTROSCOPY ANALYSIS	101
4.3.	OPTICAL CHARACTERIZATION.....	110
4.3.1.	DIFFUSE REFLECTANCE SPECTROSCOPY	110
4.4.	CONCLUSION	113
4.5.	REFERENCES.....	114
CHAPTER 5	117
CONCLUSIONS AND RECOMMENDATIONS	117
5.1.	SPRAY PYROLYSIS	117
5.2.	X-RAY DIFFRACTION (XRD) ANALYSIS	117

5.3.	SCANNING ELECTRON MICROSCOPY (SEM)	117
5.4.	HIGH RESOLUTION TRANSMISSION ELECTRON MICROSCOPE (HRTEM)	118
5.5.	RAMAN SPECTROSCOPY ANALYSIS.....	118
5.6.	UV-VISIBLE SPECTROSCOPY	119
5.7.	RECOMMENDATIONS	119
	APPENDIX A.....	I
	RESEARCH OUTPUTS.....	I
A.1.	LOCAL CONFERENCES	I
A.2.	LIST OF PUBLICATIONS	II
A.3.	MANUSCRIPT IN PROGRESS IN PEER REVIEWED JOURNALS	II
A.4.	GENERAL PRESENTATIONS	II
A.5.	ACCEPTED ABSTRACTS	III

LIST OF SYMBOLS

\AA	Angstrom
meV	Milli-electron volts
σ	Surface tension coefficient
μ	Mu
θ	Theta
f	Frequency
λ	Wavelength
τ	Mean particle size
β	Full width at half maximum
K	Shape factor
r	radius
d	distance
Γ	Brillouin zone
A_1	Phonon modes allowed in Raman Spectroscopy
B_1	Phonon modes allowed in Raman Spectroscopy
E_1	Phonon modes allowed in Raman Spectroscopy
E_2	Phonon modes allowed in Raman Spectroscopy
η	Liquid viscosity
Q	Volumetric flow rate
F	Forcing sound frequency
ρ	Liquid density
We	Weber number
Re	Reynolds number
Oh	Ohnesorge number
u	Liquid velocity

ACRONYMS

CVD	Chemical vapor deposition
PSP	Pneumatic spray pyrolysis
PECVD	Plasma enhanced chemical vapor deposition
LPCVD	Low pressure chemical vapor deposition
APCVD	Atmospheric pressure chemical vapor deposition
MOCVD	Metal organic chemical vapor deposition
E_g	Energy band gap
QDs	Quantum dots
DSSC	Dye sensitized solar cell
PV	Photovoltaic
ITO	Indium tin oxide
HRXRD	High resolution X-ray diffraction
F: SnO ₂	Fluorine doped tin oxide
TBA	Tetrabutylammonium
XRD	X-ray diffraction
SEM	Scanning electron microscope
EDS	Energy dispersive x-ray spectroscopy
FE-SEM	Field emission scanning electron microscope
HRTEM	High-resolution transmission electron microscopy
SAED	Selected area electron diffraction
RS	Raman spectroscopy
UV-Vis	Ultraviolet-visible spectroscopy
DRS	Diffuse reflectance spectroscopy
FWHM	Full width at half maximum

CHAPTER 1

INTRODUCTION

1.1. OVERVIEW

Development of efficient semiconductor metal oxides has become an area of significant research interest because it is considered as a potential approach to solve energy crisis [1]. More particularly, ZnO semiconductor nanostructures have attracted considerable interest during the past decades in terms of new technological applications, mainly because of the unique properties observed at nanoscale [2, 3, 4]. Nano-sized ZnO has been intensively studied because of its high exciton binding energy (60 meV), high photosensitivity, nontoxic nature, large bandgap, and presents a low cost material for solar cell electrodes [3-5]. Moreover the morphologies of ZnO nanomaterials can be easily modified and controlled by a chemical reaction, which is an important factor influencing the performance of these nanomaterials for many technological applications [5-7]. It has been reported that modification of ZnO has an effect on its structural, electronic and optical properties [8]. Recently, great efforts have been devoted to synthesize doped ZnO nano crystallites in order to improve the electrical, optical, and catalytic properties of material by changing the surface properties, such as electronic band gap, O vacancies, crystal deficiencies, and specific surface area.

Doping with non-metallic elements such as carbon, nitrogen and sulphur has also been considered to reduce the bandgap of ZnO semiconductors [1, 8, 9, 10]. Specifically, carbon has been usually used as the dopant to change the electronic structures of ZnO semiconductors because of its equivalent size with oxygen and the low energy requirement for the substitution of oxygen atom as compared to other non-metal dopants. However, to date, the use of C-doped ZnO nanomaterials has been modest because of the scarcity of scientific articles that report on the effect of change of nano-material properties due to introduction of dopants. It has been theorized that introduction of dopants improves both the optical and structural properties of ZnO. Therefore, to realize full potential of ZnO nanomaterials for applications in solar devices, it is very important to investigate changes in nanomaterials properties due to non-metal doping.

Many techniques have been developed to synthesize un-doped and doped ZnO nano-particles, including solid-state method, spray pyrolysis method, microwave heating process,

hydrothermal method, chemical coprecipitation method, chemical vapor deposition (CVD) and sol-gel methods [3,10,31–34]. The growth morphology, crystalline structure and stoichiometry of ZnO thin films are very sensitive to the deposition conditions [11]. These variations arise from small changes in the deposition conditions. The need for stoichiometric ZnO films suggests that a deposition method where the film stoichiometry is controlled by a chemical reaction would enable more consistent results. Moreover, it is an inherent requirement when developing new methods for deposition of electrodes for low cost solar cells to keep the deposition system as simple as possible, maximize throughput, and keep costs at a minimum. Spray pyrolysis methods offer such an opportunity.

Spray Pyrolysis methods offer the opportunity to precisely control the structural, optical and electronic properties of nanomaterials since the stoichiometry of the chemical precursors is governed by chemical reactions. Moreover, aerosol processes have the potential to replace primordial expensive and complicated solid state techniques for production of ZnO nanostructures like plasma enhanced chemical vapor deposition (PECVD) [12-14], low pressure chemical vapor deposition (LPCVD) [13,15], atmospheric pressure chemical vapor deposition (APCVD) [16-18], metal organic chemical vapor deposition (MOCVD) [19-22], evaporation [23], spin on methods [24-26], sputtering [27], ion assisted deposition [28], plasma anodization [29], reactive ion plating [30], laser ablation [31], filtered arc deposition [32], and atomic layer epitaxy [33]. These techniques have the essential disadvantage of high vacuum chambers which increases the cost of depositing ZnO nanostructures and the entire cost of the solar cell device. Moreover, SP systems have operational simplicity; the nanoparticles produced have consistent structural, optical and electronic properties. Also nano-particles are produced in a one step process without the need for further purification or excessive drying procedures which has impact of the total thermal budget and cost of production of ZnO nanostructures. Additionally, the technique can be used to coat large substrates and presents the opportunity for industrial scaling. Lastly, SP technique offers a very simple and relatively cost effective method unlike many other film deposition techniques. The present study exposes novel structural, optical and electronic properties of carbon doped ZnO deposited by pneumatic spray pyrolysis (PSP) technique. Furthermore, the dearth of specific research articles that report on the effect of doping on nanomaterial properties of ZnO deposited by a PSP technique was also the main motivation of the present compilation.

1.2. SOLAR CELLS

Among the renewable energy sources solar energy has a great importance. Solar radiation (sun's radiation) has always been the most powerful energy source on earth. It is clean, environmentally friendly and is for free. Sunlight can be transformed into electricity using solar cells [34]. The sun is our primary source of energy in the solar system, yet the solar devices that have been developed to harness the energy are among the weaker energy sources compared to other forms of renewable energy [35]. The efficiency of conventional solar cells manufactured from inorganic materials (i.e. silicon solar cells) have reached their theoretical and practical efficiency limit of 29 % using very expensive materials of high purity and energy intensive processing techniques.

New ways of manufacturing solar cells that can scale up to large volumes and low cost are required. In conventional p-n junction silicon solar cells, the current generation mechanism is far less efficient than that in dye sensitized solar cells (DSSC). Therefore, it seems reasonable to place more emphasis and effort into the research and development of DSSC [36, 37]. At current status, photovoltaics hardly contribute to the energy market because they are far too expensive [38]. The immense manufacturing costs for silicon solar cells originate from the energy intensive production of highly pure silicon and it is one of the major drawbacks for the large scale production of silicon solar cells for commercial purposes [39]. To ensure a sustainable technology path for photovoltaics, efforts to reduce the current silicon technology are urgently needed [39, 40]. In order to fabricate solar cells for practical use, an industrial procedure to prepare nanoparticles or thin films on a large scale should be developed immediately. The techniques for fabrication of ZnO such as chemical vapour deposition (CVD) [15], sol gel [3], laser ablation [31], reactive evaporation [12], magnetron sputtering technique [42], pulsed laser deposition [43] are of high cost and not commercially feasible. Hence there is a need to replace them with PSP. Spray pyrolysis deposition is one of the most promising techniques, since the film formation is carried out in air using less sophisticated equipment [36, 40, 41]. SP techniques offer numerous advantages: i.e. low-cost, simplicity and adaptation for large-scale production. This makes PSP the most attractive technique, for possible commercial production.

1.3. SPRAY PYROLYSIS

Spray pyrolysis (liquid to particle conversion) is an aerosol process that atomizes a precursor solution, evaporates solvent vapour molecules in a furnace or heats source and generates semiconductor nanoparticles and thin films. Spray pyrolysis using pneumatic nebulizer technique is a very easy, low cost, safe and non-vacuum system. Despite its simplicity SP methods provide a relatively simple way to introduce non-metal dopants at ration required through the proportions of the precursor solutions. Moreover, SP technique offers a very easy way for the synthesis of some metal oxide nanomaterials, mixed metal oxides and metals on metal oxides. Spray pyrolysis system is controlled by the following parameters namely furnace temperature and ambient environment, pneumatic nebulizer, distance between nozzle and substrate, droplet size, concentration of a precursor solution and the speed in which the solution flows.

Spray pyrolysis generation starts off when the pneumatic pump converts the starting solution to form small mist of droplets and those droplets of the sprayed solution are transferred into the heat zone (furnace or reactor) through a diffusion tube (Aluminium tube) into a reaction chamber and onto a heated substrate where solvent vapour molecules evaporate and generate semiconductor nanoparticles and thin films. Commonly, metal acetate, chloride and nitrate precursor solutions prepared by water or alcohol as a solvent are usually used to fabricate metal oxides nanoparticles. It is an attractive technique because it can produce nanoparticles that are more crystalline and less agglomerated with large specific surface areas.

1.4. ZINC OXIDE

Zinc oxide (ZnO) presents interesting material system for investigation due to its wide band gap ($E_g = 3.37$ eV in 300K) with a high exciton binding energy (60 meV) [1, 2, 42]. Moreover ZnO is a versatile II-VI semiconductor material with a variety of applications including field effect transistors, gas sensors, piezoelectric devices and solar cells [2-5].

Previously, its versatile applications have motivated a great deal of research on synthesis and investigation of properties of ZnO nanomaterials, such as quantum dots (QDs) [42, 43] nanoparticles (NPs) [44], nanofilms [45], nanostars [46]. In particular ZnO NPs are expected to become function and integration of nanostructure assembly for dye sensitized solar cell

electrodes and nanoscale devices [47]. As a crucial advantage, the synthesis of ZnO is more cost effective than other various alternative semiconductors such as III-V semiconductors [48]. Its low price compared with other wide band gap semiconductor nanomaterials makes it a good candidate for industrial applications. ZnO exhibits a broad range of properties that depend on doping including conductivity from metallic to insulating, high transparency, piezoelectricity, wide band gap semi-conductivity, room temperature ferromagnetism, huge magneto-optic, and chemical sensing effects [2, 3, 5, 48]. Additionally, ZnO is photo-responsive in the visible part of the electromagnetic spectrum, and hence it can be used as a transparent semiconducting oxide in solar cell devices. Despite its practical importance, current knowledge of structural, morphological and optical properties of doped ZnO nanostructures is rather limited. Understanding the specifics of properties of ZnO NPs can prove to be crucial in the development of DSSC employing doped ZnO NPs and nanoscale devices.

1.5. PROBLEM STATEMENT

In today's society, it is becoming ever important to find alternative sources of energy that are both cheap and efficient. Solar cells have become one of the most widely researched methods of obtaining energy in "greener" ways than burning fossil fuels. One of the new variants on the solar cell that is currently being researched is the DSSC. DSSCs offer a low cost means of harvesting the sun's energy as compared to silicon solar cells. However the peak power production of DSSCs is ~ 15 % which is still lower than the 29% offered by the silicon solar cells.

Typically the electron transport time constants in TiO₂ NPs in the DSSC are comparably slow (due to a trapping/de-trapping type of electron transport) while ZnO as a semiconductor has the highest exciton binding energy of 60 meV. Hence it is logical and reasonable to replace the current TiO₂ photo anode with a modified ZnO photo anode so that we can reduce the electron hole recombination rate in the current DSSC technology. Current technologies such as CVD and sol gel are of sophisticated and of high cost to fabricate ZnO nanostructures of high purity. Therefore, it is reasonable to replace the current technologies with the simple and relatively cost-effective technique such as spray pyrolysis and solution based methods for fabricating ZnO nanostructures. The current methods employ toxic, corrosive and explosive precursors.

1.5. RATIONALE AND MOTIVATION

Solar radiation is a plentiful, clean source of energy and harnessing the energy of the sun to replace fossil fuels holds great promise. Although the cost of electrical energy production on a per watt basis using silicon solar cells is quite high as compared to coal or nuclear based electricity production. The commercial availability of inorganic solar cells based on crystalline silicon solar cells is limited by the high financial and energy cost of production.

Only about 30% of solar energy is converted into useful electricity. The conversion of sunlight's energy by renewable energy technologies (RETs) provides good environmental technology possibilities for the electric industry. Renewable energy can increase access to clean energy and lower the greenhouse gas emissions. Photovoltaic (PV) conversion provides a remarkably straightforward and clean means of producing electricity from a raw resource in a one-step process that is carbon-neutral and has no by-products. The conventional techniques for fabrication of ZnO, like CVD, sol-gel and laser ablation are expensive and difficult for commercial or industrial scale. Hence PSP offers a cheaper and alternative form of producing ZnO nanostructures for solar application with the capability of industrial scale.

1.6. AIMS AND OBJECTIVES

1.6.1. AIMS

- Synthesize un-doped and carbon doped ZnO nanoparticles using pneumatic spray pyrolysis technique (PSP).
- Characterize the synthesized un-doped and carbon doped ZnO nanoparticles using XRD, SEM, HRTEM, RS and UV-Vis spectroscopy.

1.6.2. OBJECTIVES

- Synthesize un-doped and carbon doped ZnO nanoparticles using pneumatic spray pyrolysis (PSP).
- Characterize doped and un-doped ZnO nanoparticles for their morphological, structural and optical properties, using SEM-EDX, HRTEM, XRD, RS, and DRS.

- Determine the morphological changes in ZnO as the C-dopant level is varied using SEM.
- Determine the crystal structure of the carbon doped ZnO (C-ZnO) using XRD.
- Analyze the optical Raman modes of ZnO nanoparticles synthesized by PSP using RS.
- Determine whether there are any changes in the reflectance of the C-ZnO as doping level increases using DRS.
- Evaluate changes in nanoparticle size as doping levels change through TEM.

1.7. RESEARCH QUESTIONS

- What is the optimal assemble of pneumatic spray pyrolysis technique for fabrication of ZnO nanoparticles?
- How to synthesise un-doped and carbon doped ZnO nanoparticle using pneumatic spray pyrolysis technique?
- How to dope ZnO using tetrabutylammonium?
- What is the effect of carbon doping on the morphological, optical and structural properties of ZnO?

1.8. LIMITATIONS AND DELIMITATIONS OF THE STUDY

- The electronic properties of the synthesize un-doped and carbon doped ZnO nanoparticles using pneumatic spray pyrolysis were not investigated due to unavailability of the four point probe (I-V characterization)
- The solar cell device was not fabricated since the electronic properties of ZnO nanoparticles are one of the major properties to considered before fabricating a solar cell device.
- Characterization of solar cell device is beyond the scope at this level.

1.9. REFERENCES

1. X. Zhang, J. Qin, R. Hao, L. Wang, X. Shen, R. Yu, R. Liu, Carbon-Doped ZnO Nanostructures: Facile Synthesis and Visible Light Photocatalytic Applications, *J. Phys. Chem. C*. 119 (2015) 20544–20554.
2. H. Ghaffarian, M. Saiedi, M.A. Sayyadnejad, Synthesis of ZnO Nanoparticles by Spray Pyrolysis Method, *Iran. J. Chem. Eng* 30 (2011) 1–6.
3. S. Dai, Y. Li, Z. Du, K.R. Carter, Electrochemical deposition of ZnO hierarchical nanostructures from hydrogel coated electrodes, *J. Electrochem. Soc.* 160 (2013) 1–9.
4. S. P. Shrestha, R. Ghimire, J.J. Nakarmi, Y. Kim, Properties of ZnO: Al Films Prepared by Spin Coating of Aged Precursor Solution, *Bull. Korean Chem. Soc.* 31 (2010) 1-7
5. C. Tsay, K. Fan, Optimization of Zr-Doped ZnO Thin Films Prepared by Sol-Gel Method, *Mater Trans.* 49 (2008) 1900-1904.
6. H. R. Ghorbani, F.P. Mehr, H. Pazoki, B.M. Rahmani, Synthesis of ZnO Nanoparticles by Precipitation Method. *Adv. Mater.*31 (2015) 1220-1221.
7. S. Hori T. Suzuki, S. Miura, S. Nonomura, Effects of Deposition Temperature on the Electrochemical Deposition of Zinc Oxide Thin Films from a Chloride Solution. *Mater Trans.* 55 (2014) 728–734.
8. D. Zhang, M. Wang, J. Ma, G. Han, S. Li, Enhanced photocatalytic ability from carbon-doped ZnO photo-catalyst synthesized without an external carbon precursor, *F.Mater Lett.* 7 (2014) 1-5.
9. C. Yu. W. Lan, K. Huang, Indium-Nitrogen Co-doped Zinc Oxide Thin Film Deposited by Ultrasonic Spray Pyrolysis on n-(111) Si Substrate: The Effect of Film Thickness, *J.Nanomater.* 2014 (2014) 1-7
10. A. Bagabas, A. Alshammari, M.F. Aboud, H. Kosslick, Room-temperature synthesis of zinc oxide nanoparticles in different media and their application in cyanide photo degradation, *Nanosc. Res. Lett.* 8 (2013) 516.
11. M. Ghosh, D. Karmakar, S. Basu, S.N. Jha, D.Bhattacharyya, S.C. Gadkari, S.K. Gupta, Effect of size and aspect ratio on structural parameters and evidence of shape transition in zinc oxide nanostructures, *J. Phys. Chem.S.* 75 (2014) 543–549.
12. P. Kumar, Y. K Walia, Synthesis and Structural properties of Zinc Oxide Nano Particles A Review, *Asian J. of Adv. Basic Sci.* 2 (2014) 39-49.

13. B. P. Zhang, N. T. Binh, K. Wakatsuki, Y. Segawa, Y. Yamada, N. Usami, M. Kawasaki H. Koinuma, Pressure-Dependent ZnO Nanocrystal Growth in a Chemical Vapor Deposition Process, *J. Phys. Chem. B.* 108 (2004) 10899–10902.
14. D. Li, M. Carrette, A. Granier, J. P. Landesman, A. Goulet, *Appl. Surface Sci.* 283 (2013) 234-239.
15. H. Yoo, S. Bruckenstein, Synthesizing Nanoparticles Using Reactions Occurring in Aerosol Phases, *Adv.Nanopart.*, 2 (2013) 313–317.
16. A. A Oladiran, A. M. Olabisi, Synthesis and Characterization of ZnO nanoparticles with zinc Chloride as Zinc Source, *Asian J. natur.appl sci.* 2 (2013). 2186–8476.
17. S. Aydin, G. Turgut, M.Yilmaz, M. Ertrugul, Fabrication of ZnO nanorods by simplified spray pyrolysis, *Bitlis Eren University J.Sci.Technol.* 1 (2011) 11–30.
18. M. Takuji, K. Ken, T. Takanori, Y. Shinsuke, Thermal conductivity of titanium dioxide films grown by metal-organic chemical vapor deposition *Surface and Coatings Technology*, *J.phys.Chem.C.* 202 (2008) 3067-3071.
19. B. Hahn, G. Heindel, E. Pschorr-Schoberer W. Gebhardt, MOCVD layer growth of ZnO using DMZn and tertiary butanol, *Semicond. Sci. Technol.* 13 (1998) 788-791.
20. M. Nirmala, A. Anukaliani, Synthesis and characterization of un-doped and TM (Co, Mn) doped ZnO nanoparticles. *Mater Lett.* 65 (2011) 2645–2648.
21. O. Jung, S. Kim, K. Cheong, W. Li, S. Ismat Saha, Metallorganic Chemical Vapor Deposition and Characterization of TiO₂ Nanoparticles, *Bull. Korean Chem. Soc.* 24 (2003) 49-54.
22. N, Sadananda Kumar, K,V. Bangera, G.K. Shivakumar, Effect of annealing on the properties of Bi doped ZnO thin films grown by spray pyrolysis technique, *Sup. latt. Microstru.*75 (2014) 303–310.
23. R. Wallace, A.P. Brown, R. Brydson, K. Wegner, S.J. Milne. Synthesis of ZnO nanoparticles by flame spray pyrolysis and characterisation protocol, *J. Mater. Sci.* 48 (2013) 6393–6403.
24. D. Rathee, M. Kumar, K.A. Sandeep, Deposition of nanocrystalline thin TiO₂ films for MOS capacitors using Sol–Gel spin method with Pt and Al top electrode, *sol. state electro.* 76 (2012) 71-76.
25. S. Sharma, A. Tran, O. Nalamasu, P.S. Dutta, Spin-coated ZnO thin films using ZnO nano-colloid. *J. Electro. Mater.* 25 (2006) 1237–1240.
26. E. Zaleta-Alejandre, J. Camargo-Martinez A. Ramirez-Garibo M.L. Pérez-Arrieta, R. Balderas-Xicohténcatl, Z. Rivera-Alvarez, C. Falcony, C, Structural, electrical and

- optical properties of indium chloride doped ZnO films synthesized by ultrasonic spray pyrolysis technique, *Thin Sol. Film.*524 (2012) 44–49.
27. H. Y. Yoo, S. Bruckenstein, synthesizing nanoparticles using reactions occurring in aerosol phases, *Adv. Nanopart.* 2 (2013) 313–317.
 28. M. Hasanpoor, M. Aliofkhazraei, H. Delavari, Microwave-assisted synthesis of zinc oxide nanoparticles, *Procedia Mater.Sci.*11 (2015) 320-325.
 29. A. Shetty, K. Nanda, Synthesis of zinc oxide porous structures by anodisation with water as an electrolyte. *Appl. Phys. A.* 109 (2012) 151–157.
 30. M. Jyoti, D. Vijay, S. Radha, To study the role of temperature and sodium hydroxide concentration in the synthesis of zinc oxide nanoparticles, *Int. J.Sci. Res. Pub.* 3 (2013) 2250-3153.
 31. A. Gondala, Q.A. Drmosha, Z.H. Yamania, T.A. Salehb, Synthesis of ZnO nanoparticles by laser ablation in liquid and their annealing transformation into ZnO nanoparticles. *J. Mater. Sci.* 256 (2009) 298–304.
 32. R. J. Mendelsberg, S.H.N. Lim, Y.K. Zhu, J. Wallig, D. J. Milliron A. Anders, Achieving high mobility ZnO: Al at very high growth rates by dc filtered cathodic arc deposition, *J. Phys. D: Appl. Phys.* 44 (2011) 1-5.
 33. G. Kenanakis, N. Katsarakis, E. Koudoumas, Influence of precursor type, deposition time and doping concentration on the morphological, electrical and optical properties of ZnO and ZnO :Al thin films grown by ultrasonic spray pyrolysis. *Thin Sol. Film.* 555 (2014) 62–67.
 34. M. Miller, Maximum Power from a Solar Panel Mathematical modeling. *Chem. Rev.* 3(2010), 1–10.
 35. D. Hedberg, B. Kasemo, S. Kullander, R. Lundin, B. A. E. P. Nordén, B. Stridh, statements on solar Energy. *Solar Ener.* (2008) 1-5.
 36. M. Yusof, Analysis energy demand and design of solar energy in UMP mosque. *J. Chemical Infor. Mod.* 53 (2009), 160.
 37. F. T. Kong, S.Y. Dai, K. J. Wang, Review of recent progress in dye-sensitized solar cells. *Adv. OptoElectro.* 2007 (2007), 1–13.
 38. X. Xin, J. Wang, W. Han, M. Ye, Z. Lin, Dye-sensitized solar cells based on a nanoparticle/nanotube bilayer structure and their equivalent circuit analysis. *Nanosc.* (2011) 6595–6663.

39. S. Thomas, T. G. Deepak, G. S. Anjusree, T. A. Arun, S. V. Nair, A.S. Nair, A review on counter electrode materials in dye-sensitized solar cells. *J. Mater. Chem. A*, 2 (2014), 4474–4490.
40. A. Aimable, M. T. Buscaglia, V. Buscaglia, P. Bowen, Polymer-assisted precipitation of ZnO nanoparticles with narrow particle size distribution. *J. Euro. C. Soc.* 30 (2010), 591–598.
41. M. Nirmala, A. Anukaliani, Characterization of undoped and Co doped ZnO nanoparticles synthesized by DC thermal plasma method. *Physica B: Cond. Matt.* 406 (2011) 911–915.
42. R. Zhang, P. Yin, N. Wang, L. Guo, Photoluminescence and Raman scattering of ZnO nanorods. *Sol. Stat. Sci.* 11 (2009) 865.
43. J. Yu, X. Yu, Hydrothermal synthesis and photocatalytic activity of zinc oxide hollow spheres, *Environ. Sci. Technol.* 42 (2008) 4902.
44. J. J. Macías-Sánchez, L. Hinojosa-Reyes, A. Caballero-Quintero, W. de la Cruz, E. Ruiz-Ruiz, A. Hernández-Ramírez, J.L. Guzmán-Mar, Synthesis of nitrogen-doped ZnO by sol–gel method: characterization and its application on visible photocatalytic degradation of 2,4-D and picloram herbicides, *Photochem. Photobiol. Sci.* 14 (2015) 536.
45. X. M. Zhang, M. Y. Lu, Y. Zhang, L. J. Chen, Z. L. Wang, Fabrication of a high-brightness blue-light-emitting diode using a ZnO-nanowire array grown on p-GaN thin film, *Adv. Mater.* 21 (2009) 2767.
46. G. Shen, J. H. Cho, J. K. Yoo, G. Yi, C. J. Lee, Synthesis and optical properties of S-doped ZnO nanostructures: Nanonails and Nanowires, *J. Phys. Chem. B.* 109 (2005) 5491.
47. J. Mu, Z. Guo, H. Che, H. Electrospinning of C-doped ZnO nanofibers with high visible-light photocatalytic activity, *J Sol-Gel Sci Technol*, 78 (2016) 3925.
48. A. B. Lavand, Y. S. Malghe, Visible light photocatalytic degradation of 4-chlorophenol using C/ZnO/CdS nanocomposite, *J. Saudi Chem. Soc.* 19 (2015) 471.

CHAPTER 2

LITERATURE REVIEW

2.1. OVERVIEW

This chapter starts off by providing a theoretical framework on the structural properties of ZnO. The structural properties of ZnO are presented through close evaluation of ZnO crystal structure, and the various phases of ZnO found in nature are also presented. Moreover the lattice parameters of ZnO are also presented in detail. This chapter also providing a literature review of the current methods available for deposition of ZnO nanoparticles specifically chemical vapour deposition, sol-gel technique, plasma enhanced chemical vapour deposition and laser ablation. The challenges and triumphs of these methods like the vacuum assisted methods are discussed. Furthermore, the chapter presents the theoretical framework behind spray pyrolysis (SP). The mechanisms governing droplet formation in PSP technique are discussed in detail more specifically the theory of droplet generation using the capillary wave mechanism, cavitation mechanism and combined cavitation and capillary wave mechanism. Lastly, the chapter also presents the equation governing droplet formation in PSP.

2.2. STRUCTURAL AND OPTO-ELECTRICAL PROPERTIES OF ZINC OXIDE

Zinc oxide (ZnO) is an important industrial material because it is an inorganic and semiconducting material with significant properties that share its structure as Wurtzite, because of its significant properties it has been considered as a potential approach to solve current environmental and energy issues [1, 2]. ZnO and its derivatives forms (e.g.N-ZnO, Ag-ZnO, In-ZnO etc) have been intensively studied because of their physical, chemical, electrical and optical properties, such as availability in nature, absence of toxicity, low resistivity and high optical transparency in the visible region. It has a wide range applications in a number of fields ranging from water treatment by photocatalysis, solar applications such as semiconductor electrodes for dye synthesized solar cells (DSSC), liquid crystal displays and organic light emitting diodes [2-7]. However, the applicability of ZnO in visible light is limited because of the wide band gap of the material, which results in low efficiency during solar photoconversion [2, 8]. ZnO is one of the most important semiconductor materials in group II-VI, whose chemical bonding is on the boundary between ionic and covalent semiconductors [4.5]. It has

a direct energy band gap of 3.37 eV at room temperature, high exciton binding energy (approximately 60 meV) and high thermal and mechanical stability which make it attractive for potential use in electronics, optoelectronics and laser technology [3-6]. In addition, ZnO has availability of fairly high-quality bulk single crystals and high transparency of greater than 80% in the visible wavelength region which makes it feasible for various applications. Furthermore, its direct band gap implies a higher possibility of radiative recombination which is a two body process and hence more efficient than the three body process in indirect band gap materials [8]. Figure 2.1 below demonstrates the band to band transition in momentum space in the Brillouin zone for direct and indirect band gap materials.

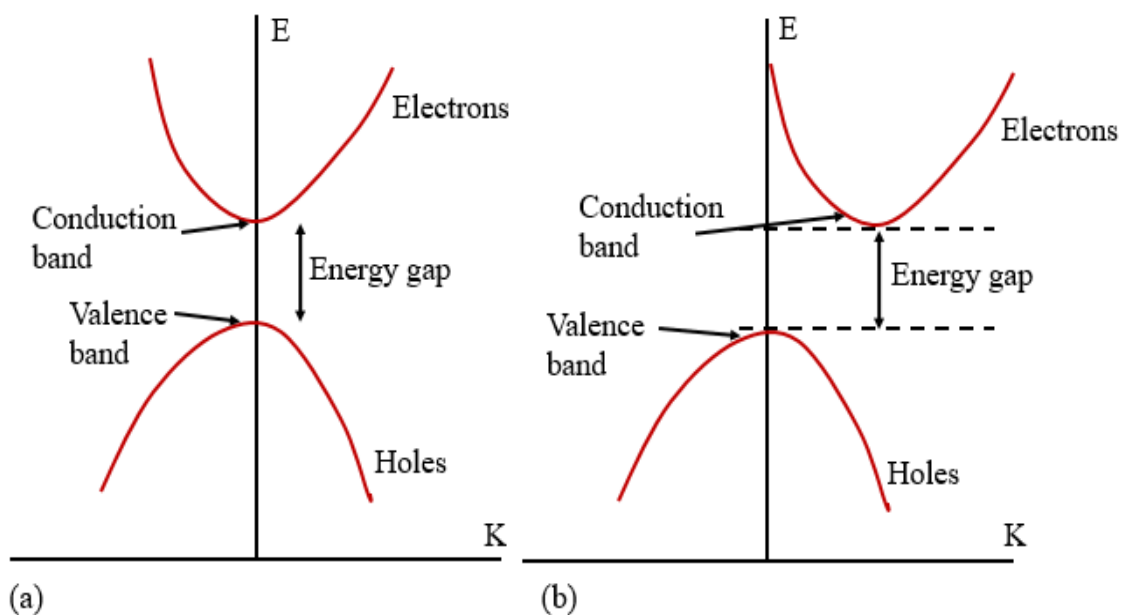


Figure 2.1: Schematic representation of transition in (a) direct and (b) indirect band gap semiconductor

Those materials for which maximum of valence band and minimum of conduction band at value of K are called direct band gap materials, such as GaAs, InP, CdS, ZnO, TiO₂ etc. They satisfy the condition of energy and momentum conservation. Those materials for which maximum of valence band and minimum of conduction band do not occur at same value of K are called indirect band gap materials such as Si and Ge. The indirect bandgap materials are not suitable for optical devices like LEDs and laser diodes. A clash in momentum space between the electron and hole conditions make the transition phonon intermediate in indirect

band gap semiconductors [8]. The excitation and relaxation between the conduction band and valence band extremes require the support of a crystal lattice vibration to conserve momentum. Radiative recombination of excited charge carriers is consequently a three body process and it is much less effective than the analogous two body recombination system in direct band gap semiconductors. The low probability of radiative recombination in indirect band gap favours a non-radiative decay processes and the excited electrons generally lose energy as heat and not by emitting photons [8].

Synthesis of ZnO is more cost effective than other alternative semiconductors such as III-V semiconductors [9]. ZnO has various fundamental advantages over other several semiconductors: (i) its free exciton is bound with energy 60 meV; (ii) it has a native substrate; (iii) wet chemical processing is possible and (iv) it is more resistant to radiation damage [8]. ZnO can be used as a sensor, converter, energy generator and photocatalyst in hydrogen production due to its piezo-and pyroelectric properties. It is an essential material in the ceramics industry because of its hardness, rigidity and piezoelectric constant while its biodegradability, biocompatibility and low toxicity make it a material of choice for biomedicine and in pro-ecological systems [4, 9]

2.3. CRYSTAL STRUCTURE

ZnO is also recognised as an II-VI compound semiconductor whose chemical binding character lies between covalent and ionic [10]. Due to the large ionicity of bonds, zinc and oxygen planes bear electric charge (positive and negative, respectively). The planes reconstruct at atomic level to maintain electrical neutrality in most of the relative materials, but not in ZnO because its surfaces are atomically flat, stable and exhibit no reconstruction. ZnO crystallize in either cubic zinc blende or hexagonal Wurtzite, where two binding partners of zinc (Zn^{2+}) and oxygen (O^{2-}) ions are arranged in a manner that each Zn^{2+} is surrounded by a tetrahedral of O^{2-} and vice-versa [8-10]. This tetrahedral coordination is characteristic of Sp^3 covalent bonding nature and it also gives rise to polar symmetry along the hexagonal axis, the polarity is liable for a number of the properties of ZnO such as its piezoelectricity and spontaneous polarization, and it is also a main aspect in crystal growth, etching and defect generation [8]. The crystal structure of ZnO is in three forms: hexagonal Wurtzite (B4), cubic zinc blende (B3) and the rarely observed cubic rocksalt (or Rochelle salt). At ambient pressure and temperature, the thermodynamically

most stable phase of ZnO is the Wurtzite (B4) structure. Under stress or at relatively high pressures of approximately 10 GPa, ZnO can only exhibit rock salt (NaCl) type structure. The zinc blende ZnO structure can be stabilized upon growth on cubic substrates [8- 11].

The hexagonal Wurtzite and zinc blende ZnO lattices have no inversion symmetry (reflection of a crystal at relatively any given point does not transform it into itself). In single crystal Wurtzite structure, 4 atoms per unit cell give rise to 12 phonon modes. These modes are essential in understanding the thermal, electrical and optical properties of the crystal. ZnO has a Wurtzite structure, which belong to the space group P63mc and has a point group 6 mm (Hermann-Mauguin notation) or C_{6V}^4 (Schoenflies notation), with two formula units per primitive cell where all atoms occupy C_{3V} [10, 12]. At ambient conditions, pure ordered ZnO has lattice constants of $a = 0.325$ nm and $c = 0.521$ nm with a c/a ratio of about 1.60 which is close to the hexagonal cell $c/a = 1.633$. The Wurtzite ZnO sample has an orientation indicated by four digit miller indices (hkil), with $h+k = -i$. In most samples with well-defined crystal orientation are c-plane oriented, for example, the surface is the hexagonal (0001) plane. Likewise, the directions parallel to the c-axis are represented with (0001) [10].

The lattice parameters are usually measured at room temperature by X-ray diffraction (XRD), which is considered to be the most accurate one, using Bragg's law. In ternary compounds, the technique can also be used for determining the composition although strain and relevant problems must be taken into consideration as the samples are in the form of epitaxial layers on foreign substrates. The lattice parameter can be affected by free charge, impurities, stress and temperature. Because the c/a ratio also relates with the difference of the electro-negativities of the two constituents, components with the greatest differences show largest departure from the ideal c/a ratio [13]. The schematic representation of the most common crystallization state of ZnO, the rocksalt, zinc blende and wurtzite structure is shown in Figure 2.2

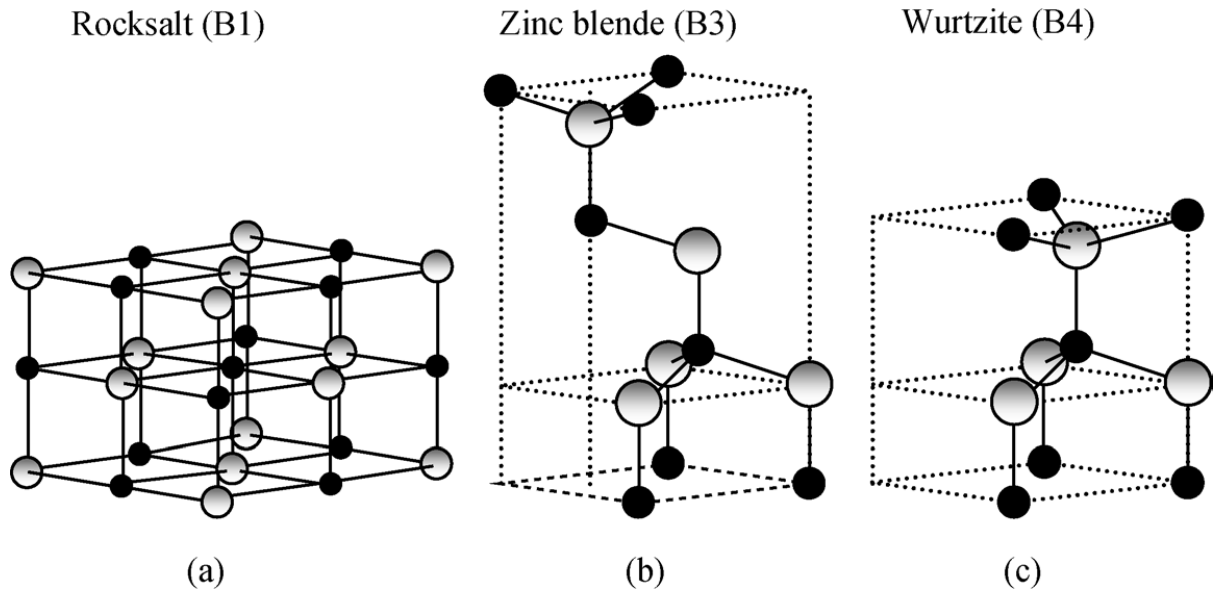


Figure 2.2: Stick-and-ball representation of ZnO crystal structures: (a) cubic rocksalt (B1), (b) cubic zinc blende (B3), and (c) hexagonal wurtzite (B4). Shaded gray and black spheres denote Zn and O atoms, respectively [8, 10, 11]

The lattice parameters of ZnO can be expressed as follows [11]

$$a = \sqrt{1/3} \frac{\lambda}{\sin\theta} \quad (2.1)$$

$$c = \frac{\lambda}{\sin\theta} \quad (2.2)$$

From “a” and “c” the volume of the unit cell can be calculated

$$V = 0.833 \times a^2 \times c \quad (2.3)$$

The lattice parameters for crystallographic systems can be calculated from the following equation using the (h k l) parameters and the inter-planar d-spacing. ZnO Wurtzite is known to be a hexagonal system [11].

$$\frac{1}{d_{hkl}^2} = \frac{4}{3} \left(\frac{h^2 + hk + k^2}{a^2} \right) + \frac{l^2}{c^2} \quad (2.4)$$

where “a” and “c” are the lattice constants and h, k, l are the miller indices along x, y, and z axis respectively.

2.4. DOPING

ZnO displays broad range of properties that depend on doping, including a range of conductivity from metallic to insulating (including n-type and p-type conductivity), high transparency, piezoelectricity, wide-band gap semiconductor, room-temperature ferromagnetism and huge magneto-optic and chemical sensing effects [9]. It has been reported that modification of ZnO has an effect on the structural, electronic and optical properties [8]. As grown ZnO is generally n-type with dominating shallow donors. This n-type character was found to be due to the presence of native point defects. The oxygen vacancy and the zinc interstitial act as donors and they are not expected to play a major role due to their high formation energy [9, 10, 15]. Other native defects donors, particularly complexes involving Zn, may have a more important effect on the n-type character of Zn. The dominant donor in as-grown ZnO is hydrogen, which is always a donor in ZnO and has a low formation energy [10]. Besides the n-type properties of the as-grown ZnO, also additional n-doping proves to be simple, as the group III elements Al, In and Ga can easily be incorporated on Zn sites, resulting in possible carrier concentrations above 10^{20} cm^{-3} . While n-type ZnO is clearly available without complications, p-doping is probably the primary technical issue of ZnO processing.

Low acceptor concentrations in as-grown ZnO can be simplified by zinc vacancies yet are clearly overcompensated by the displayed n-type properties. The group I elements Li and Na are expected to be shallow acceptors on Zn sites, both can be incorporated as donors (LiI, NaI) as well [10]. It is very important to fabricate both p-type and n-type semiconductors to realize the applications of ZnO for applications in devices. Recently, great efforts have been devoted to synthesize doped ZnO nano crystallites in order to improve the electrical, optical, and catalytic properties of materials by changing the surface properties, such as electronic band gap, O vacancies, crystal deficiencies, and specific surface area. Doping with non-metallic elements such as carbon, nitrogen and sulphur has also been considered to reduce the bandgap

of ZnO semiconductors [2, 14, 15, 16]. Specifically, carbon has been usually used as the dopant to change the electronic structures of oxide semiconductors because of its equivalent size with oxygen and the low energy requirement for the substitution of O. Other promising experiments towards p-doping of ZnO have been conducted with the other group V elements such as, N, P, As and Sb but still there are no straightforward procedure that have been constructed for fabricating reproducible and stable p-type ZnO of high quality [10, 14].

The interest in doping ZnO is to explore the possibility of tailoring its electrical, magnetic and optical properties. The doped ZnO thin films and/or nanoparticles can be used in areas such as electronics, optoelectronics and could be a potential contestant to other oxides like indium tin oxide (ITO), cadmium oxide (CdO), tin oxide (SnO₂) and titanium dioxide (TiO₂). The doping of ZnO offers a feasible means of fine tuning the band gap to make use as UV detector and light emitters [17]. Doped ZnO is photo-responsive in the visible part of the electromagnetic spectrum, and hence it can be used as a transparent semiconducting oxide, solar cell devices, blue/UV solid-state emitters, shield against high-energy radiation, organic light-emitting diodes (OLED) and transparent thin film transistors (TTFT) [9,17]. The photo-induced high electron hole pair recombination ratio limits the applications of the material to a significant extent as UV light account for only a small fraction (approximately 5%) of the solar radiation spectrum compared with visible light (approximately 45%). Therefore the components or mechanisms by which the bandgap of ZnO might be increased to extend its working range to the visible light region and use sunlight more efficiently are an important area of investigation in solar energy transformation and environmental cleaning [2, 5, 7].

2.5. LATTICE PARAMETERS

Lattice parameters of ZnO have been explored over several decades [11]. The lattice parameters of a semiconductor commonly depend on the following factors: (i) free electron concentration acting via deformation potential of a conduction band minimum occupied by these electrons, (ii) concentration of foreign atoms, defects and their difference of ionic radii with respect to the substituted matrix ion, (iii) external strains (for example, those induced by substrate), and (iv) temperature. The lattice parameters of any crystalline material are commonly and most precisely measured by high resolution X-ray diffraction (HRXRD) using the bond technique for a set of symmetrical and asymmetrical reflections [8]. The strict

periodicity of lattice can be disturbed by many imperfections or defects. These imperfections have a considerable effect on the mechanical, thermal, electrical and optical properties of semiconductors. They can determine plasticity, hardness, thermal, optical and electrical conductivities. The lattice constants a and c mostly range from 3.2475 to 3.2501 Å for the a -parameter and from 5.2042 to 5.2075 Å for the c -parameter. The c/a ratio and u parameter differ in a slightly wider range, from 1.593 to 1.6035 and 0.383 to 0.3856, respectively. The deviation from that of the ideal Wurtzite ZnO crystal is possibly due to lattice stability and ionicity. The point defects, for example, zinc antisites, oxygen vacancies, and extended defects, such as threading dislocations, additionally increase the lattice constant in ZnO crystal [8, 10]. Table 2.1 shows the important physical parameters of ZnO.

Table 2.1 Some important physical and electrical properties of ZnO

Parameter	Value
Stable phase at 300K	Wurtzite
Lattice Parameters	'a' = 3.2495 Å 'c' = 5.2069 Å
c/a ratio	1.601
u	0.383
Density	5.606 g/cm ³
Melting point	1975 °C
Static dielectric constant	8.656
Refractive index	For wurtzite – 2.049 For zinc blende – 2.008
Energy gap	3.37 eV, direct
Exciton Binding energy	60 meV
Electron effective mass	0.24
Hole effective mass	0.59

2.6. APPLICATIONS

ZnO and its derivatives have attracted great attention due to its wide applications in a number of fields ranging from water treatment by photocatalysis and solar applications such as semiconductor electrodes for Dye synthesized solar cells (DSSC). Due to progress in processing and theoretical understanding of its unique optical, semiconducting, and piezoelectric properties, conventional applications can be improved. For example, ZnO-based systems could represent an important light source or be used as a transparent conducting oxide for applications such as front electrodes in solar cells and liquid crystal displays [2, 8, 10].

Nanotechnology and specifically nanofabrication, offers a variety of tools to contribute to solving the energy crisis, since creating materials and devices smaller than 100 nanometers (nm) offers better approaches to capture, store, and transfer energy. The level of control that nanofabrication offers could help solve many of the issues that the world is facing related to the current generation of energy technologies, including an array of alternative, renewable energy approaches [11]. One of the new variants of solar cells that is currently being researched is the DSSC. DSSCs offer a low cost means of harvesting the sun's energy as compared to silicon solar cells. However the peak power production of DSSCs is ~ 15 % which is still lower than that of 29% offered by the silicon solar cell [2, 11]. In this study we fabricated C-ZnO so that we can replace the current TiO₂ photo anode with a modified ZnO photo anode so that we can reduce the electron hole recombination rate in the current DSSC technology. Since the electron transport time constants in TiO₂ nanoparticles in the DSSC are comparably slow (due to a trapping/de-trapping type of electron transport) while in the ZnO the electron transport is faster.

2.7. ZINC OXIDE NANOSTRUCTURES

Zinc oxide nanostructured materials have optical, electrical and photochemical activity, which can be used in photocatalysis, solar energy conversion cells, ultra violet (UV) detectors and UV emitting devices, chemical sensors sensitive to chemicals such as alcohol and benzene, and gas sensing materials for many gases such as ammonia, hydrogen and ozone [7]. The nanostructured materials have received considerable attention in recent years due to their potential application in nanoscale electronic and optoelectronic devices [18]. The nano ZnO have been found to have large specific area, high pore volume, nanostructured properties and it is inexpensive which makes it a promising candidate primarily in catalysts, chemical absorbents, polymer filler and additives, antiwear additives in oil lubricants and advanced ceramics [7]. The size reduction leads to novel electrical, mechanical, chemical and optical properties which are generally believed to be the consequence of surface and quantum confinement effects. Due to the wide range of optical and electrical properties, ZnO thin films have many advantages such as high chemical and mechanical stability, high abundance, and transparency over other oxide thin films like indium tin oxide (ITO), cadmium oxide (CdO), tin oxide (SnO₂) etc [7, 18]

ZnO is used as a transparent conductive oxide (TCO) thin films, mainly in solar cells, heat mirrors, and organic light emitting diodes [5]. Nanostructures of various different morphologies can be grown by straight forward fabrication techniques. These nanostructures with various shapes such as nanowires (quantum wires), nanoparticles (quantum dots), nanofilms (quantum films), nanobelts, nanorings, nanotubes, nanodonuts and nanopropellers, serve as model systems for studying transport mechanisms in low-dimensional systems. This renders immense benefit for understanding the fundamental phenomena in low dimensional systems and also for developing new generation nanodevices with high performance and efficiency [8]. Figure 2.3. shows the structures and morphologies of different ZnO nanostructures grown and characterized by various techniques in recent years.

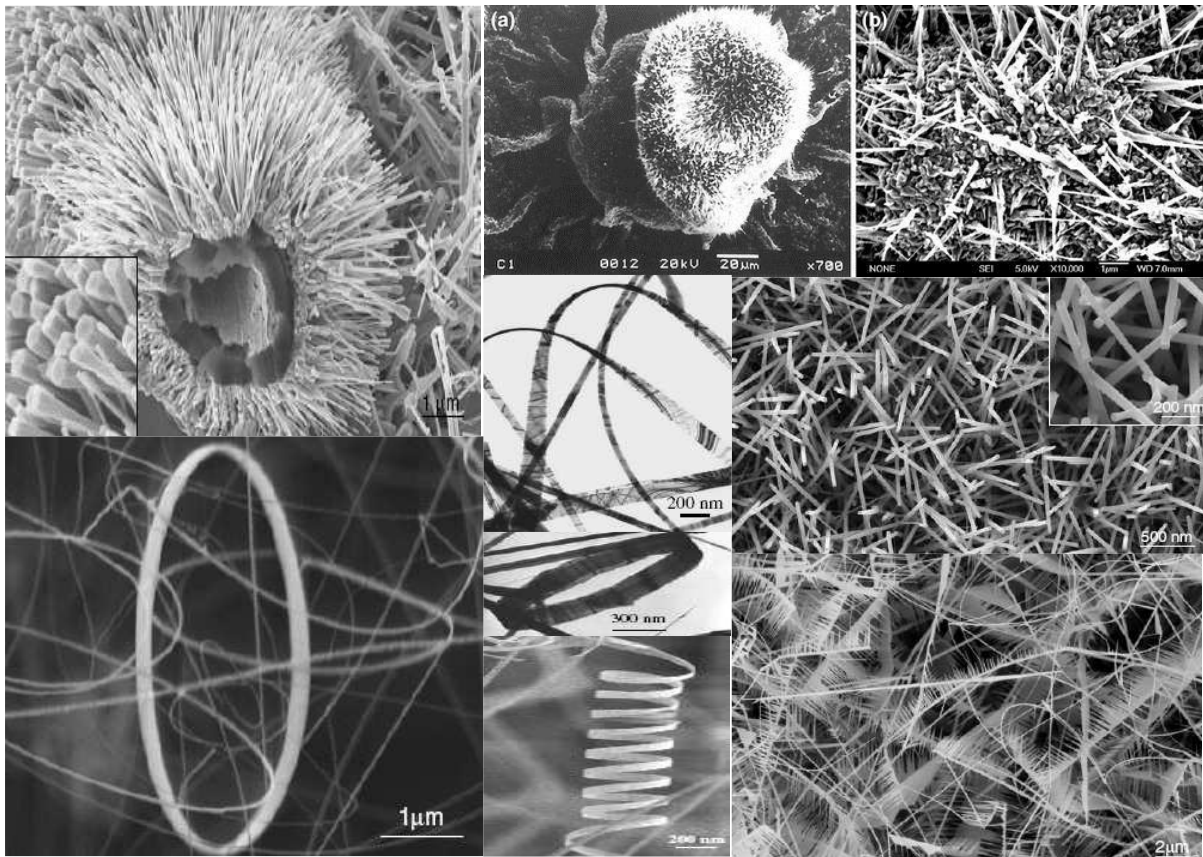


Figure 2.3: The structures and morphologies of different ZnO nanostructures fabricated and characterized by various techniques (Wang 2004). [8]

The ZnO nanostructures depend on their surface properties precisely on the surface roughness which are the basis of their application in technological devices. Currently, many researchers

are focused in the correlation of surface with deposition parameters and physical properties, and they also paid attention to specific properties of transparent metal oxide thin films. The thin film physical properties depend not only on the morphology of the sample but also on the preparation method, thickness of the sample and grain sizes. Reproducible properties are achieved only when the thickness and deposition parameters are kept constant.

Several deposition techniques have been used for the production of zinc oxide thin films in order to develop their properties [19]. Chemical synthesis techniques such as sol-gel, solvothermal and microemulsion, and physical methods including chemical vapor deposition, thermal decomposition of organometallic precursors, arc plasma, laser ablation, levitation gas condensation and spray pyrolysis are one of those techniques that were used for production of zinc oxide nanostructures. Physical methods like spray pyrolysis are useful compared to chemical ones, since they do not require several steps of wet chemistry (e.g. washing, drying and calcination) and can produce nanoparticles with controlled composition and morphology, good crystallinity and uniform size distribution. In this method different morphologies are achieved by variation of the growth parameters such as temperature, substrate and source material. Among the mentioned ZnO nanostructures, this study focuses on nanoparticles. The majority of the studied nanoparticles were prepared by wet chemical synthesis and very few by spray pyrolysis. In spray pyrolysis, precursors are sprayed on a heated substrate, where they react with each other forming nanoparticles.

2.8. ZINC OXIDE DEPOSITION METHODS

Zinc oxide has been deposited by many different techniques such as reactive evaporation, molecular beam epitaxy, magnetron sputtering technique, pulsed laser deposition, sol-gel technique, chemical vapor deposition, hydrolysis, filtered arc deposition, plasma anodization, ion assisted deposition, dip coating, plasma enhanced chemical vapour deposition, hydrothermal and solvothermal synthesis, microemulsions laser ablation, reactive ion plating and electrochemical deposition [20]. The main concern is that the growth morphology, crystalline structure, shapes, sizes and stoichiometry of ZnO thin film are very sensitive to the deposition conditions. This is a disadvantage for many physical vapour deposition methods, for example laser ablation where there are large variations in the optical and structural properties of the synthesized nano structures. These techniques do not have advantages in

producing nanocrystalline thin films, such as relatively homogeneous composition, simple deposition on glass substrate because of the low substrate temperatures involved. Furthermore, those techniques can not produce nanocrystalline thin films with controllable film thickness, fine and porous microstructure and they are not suitable for large scale production like pneumatic spray pyrolysis [21].

The combination of thermal evaporation and vapour transport method has emerged as a promising route to grow ZnO nanostructures since they have the ability to produce high yield, easy scalability and low cost. Wet chemistry, including precipitation, hydrothermal and solvothermal synthesis, microemulsions, and sol-gel processes have succeeded in the controlled synthesis of numerous shapes, sizes and morphologies, at low temperature. Among these routes, the low cost and simplicity of aqueous precipitation make this approach the most attractive, for possible commercial development [20, 21].

2.8.1. CHEMICAL VAPOUR DEPOSITION

Chemical vapour deposition (CVD) is a process where one or more volatile precursors are transported via the vapour phase to the reaction chamber, where they decompose on a heated substrate. The solid material is obtained as a coating, a powder, or as single crystals. This technique involves the dissociation and/or chemical reactions of gaseous reactants in an activated (heat, light, plasma) environment, followed by the formation of a stable solid product. The deposition involves homogeneous gas phase reactions, which occur in the gas phase, and/or heterogeneous chemical reactions which occur on or near the vicinity of a heated surface leading to the formation of powders or films. CVD is a commonly used materials processing technology. The majority of its applications include applying solid thin film coatings to surfaces, but it is also used to produce high purity bulk materials and powders, as well as fabricating composite materials through infiltration techniques [22, 23].

CVD technology consequently took on new dimensions with importance on the deposition aspects of the process. CVD is an essential technique in coating technology as made by such change of focus from extraction to deposition, for producing functional semiconducting thin films, and coatings with enhanced surface properties such as protection against wear, corrosion, oxidation, chemical reaction, thermal shock, and neutron adsorption. These coatings include III-V and II-VI materials, C, B, Si, borides, carbides, nitrides, oxides, silicides, and sulphides

[5]. Currently, in the fields of aerospace, military, science and engineering, the CVD technology has established increasing importance. It is well suitable for the preparation of several advanced products, including bulk materials as well as composites, coatings and films [5]. The present applications of CVD technology can be separated into four main categories:

1. Extraction and pyrometallurgy,
2. Electronic, and optoelectronic materials,
3. Surface modification coatings,
4. Ceramic fibres and ceramic matrix composites (CMCs).

CVD Mechanisms

In CVD the deposition can also take place due to a chemical reaction between some reactants on the substrate. Usually the reactant gases (precursors) are pumped into a reaction chamber (reactor). Under the right conditions of temperature and pressure they undergo a reaction at the substrate. One of the products of the reaction gets deposited on the substrate. The by-products are pumped out [24]. The key parameters are chemical reaction rates, gas transport, and diffusion as shown in the Figure 2.4 below.

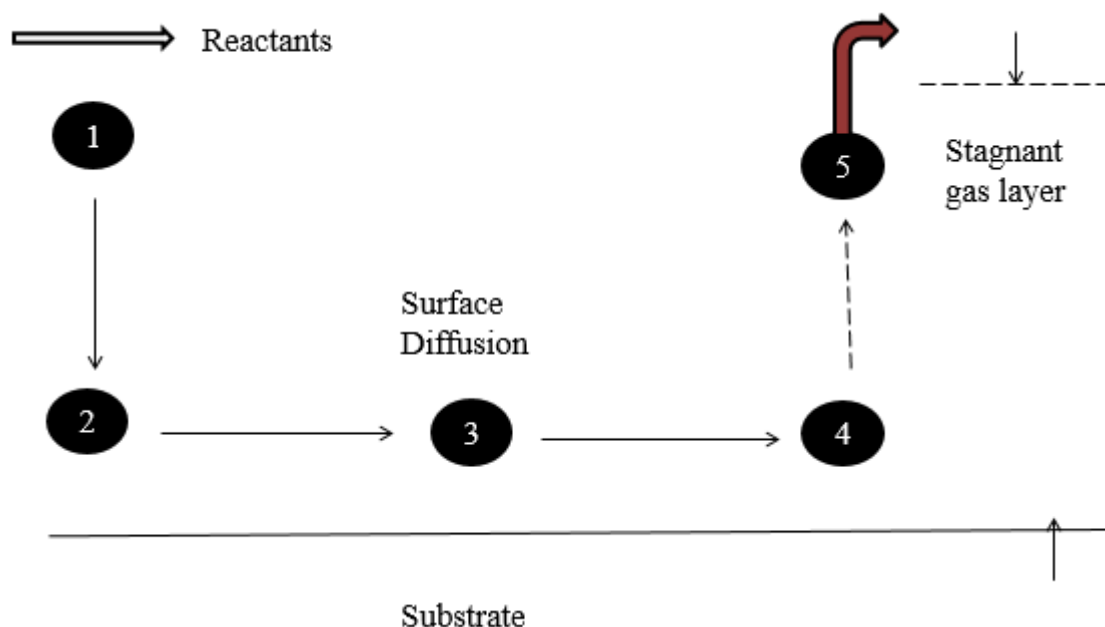


Figure 2.4: Showing the CVD mechanisms

- 1 = Diffusion of reactant to surface
- 2 = Absorption of reactant to surface
- 3 = Surface diffusion
- 4 = Desorption of gas by-products
- 5 = Out diffusion of by-product gas

The CVD system is affected by a number of factors: the reactants used in the process, the maximum acceptable leak rate of air into the system, purity of the deposit, size and shape of the substrate, process economy, etc. Many CVD processes are strongly affected by contaminants in the vapor. The contaminants can exist from the reactants themselves and from several chemical reactions between the gases and the materials in the gas dispensing system (in the tubes, evaporators, sublimators) and from air leakage [24]. The levels of contamination can be reduced by purifying the reactants and hydrogen. Argon can be purified to a level of 1 ppm in commercially available purifiers, having a low leak rate, using carrier gases which are non-reactive against the materials to be vaporized (in evaporators and sublimators), using materials in the tubes, vaporizers, reactors, etc., which are compatible with the gases used, using degassed O-rings, where they are used for vacuum seals, installing purge line, which is important when reactive gases, e.g., halides, are used [22, 24].

Deposition of semiconductor systems using CVD presents several distinctive advantages. CVD has the merit of producing highly dense and pure materials. Thin films from CVD like thin films produced by PSP technique have good reproducibility and adhesion at reasonably high deposition rates. Furthermore, CVD is a non-line-of-sight process with good throwing power. Therefore, it can be used to uniformly coat complex shaped components and deposit films with good conformal coverage. Such distinctive feature outweighs the PVD process. In addition, in CVD deposition rate can be adjusted readily. Low deposition rate is favoured for the growth of epitaxial thin films for microelectronic applications. However, for the deposition of thick protective coatings, a high deposition rate is preferred and it can be greater than tens of mm per hour. This is substantially exceeded only by techniques such as plasma spraying [24].

CVD technique has the ability of using wide range of chemical precursors such as halides, hydrides, organometallics which enable the deposition of a large spectrum of materials including, metal, carbides, nitrides, oxides, sulphides, III–V and II–VI materials. Lastly thin films can be deposited at relatively low temperatures. The desired phases can be deposited in-

situ at low energies through vapour phase reactions, and nucleation and growth on the substrate surface. This enables the deposition of refractory materials at a small fraction of their melting temperatures [23, 24]. For example, refractory materials such as SiC (melting point: 2700 °C) can be deposited at 1000 °C using the following chemical reaction:



However, deposition of thin films using CVD presents several disadvantages, which limits its application in the synthesis of ZnO thin films for solar cell applications. Firstly, it presents chemical and safety hazards because it employs toxic, corrosive, flammable and explosive precursors as contrasted to the PSP technique. Further deposition of multicomponent semiconductor materials with well controlled stoichiometry using multi-source precursors is almost impossible with CVD [3, 4, 5]. This is mainly because different precursors have different vaporization rates. Furthermore the use of sophisticated reactor, or vacuum systems by CVD variants such as low pressure or ultrahigh vacuum CVD, plasma assisted CVD and photo-assisted CVD tends to increase the cost of fabrication of solar devices employing ZnO. Hence due to the complicated nature of CVD systems it was not employed as a method of fabrication of ZnO thin films in this work [24].

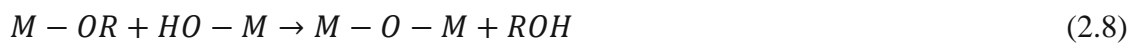
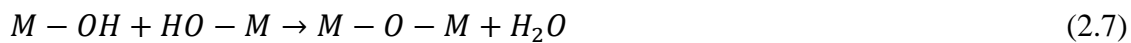
2.8.2. SOL-GEL TECHNIQUE

The sol-gel process is a wet-chemical technique widely employed in the fields of materials science and ceramic engineering. Such methods are utilized primarily for the fabrication of materials (typically a metal oxide) starting from a chemical solution which acts as the precursor for an integrated network (or gel) of either discrete particles or network polymers. This method also involves conversion of monomers into a colloidal solution (sol) that acts as the precursor for an integrated network (or gel) of either discrete particles or network polymers. A sol is a stable dispersion of colloidal particles or polymers in a solvent [25].

Usually, the precursor or starting compound is either an inorganic (no carbon) metal salt (chloride, nitrate, sulfate) or a metal organic compound such as an alkoxide, which undergoes several forms of hydrolysis and polycondensation reactions to form the final nanomaterial products. Metal alkoxides are the most widely used precursors, because they react readily with

water and are known for many metals. Some alkoxides commonly used in industry, are commercially available at low cost (Si, Ti, Al, Zr), whereas others are hardly available, or only at very high costs (Mn, Fe, Co, Ni, Cu, Y, Nb, Ta, etc) [25, 26].

The sol-gel conversion of metal alkoxides comprises of two main reaction types which are hydrolysis and condensation. The formation of a metal oxide involves connecting the metal centers with either oxo (M–O–M) or hydroxo (M–OH–M) bridges, and generating metal-oxo or metal-hydroxo polymers in solution [25]. During hydrolysis, the alkoxide groups (-OR) are replaced through the nucleophilic attack of the oxygen atom of a water molecule with release of alcohol and the formation of a metal hydroxide. Condensation reactions between two hydroxylated metal species leads to M-O-M bonds with release of water (oxolation), whereas the reaction between a hydroxide and an alkoxide leads to M-O-M bonds under release of an alcohol (alkoxolation) [26]. The equations below show the main reactions in the sol-gel process using metal alkoxides. Hydrolysis (Eq. 3.2) and condensation, involving oxolation (Eq. 3.3) and alkoxolation (Eq. 3.4).



Synthesis of thin films using the sol-gel technique involves (1) preparing a homogeneous solution of easily purified precursor(s) generally in an organic solvent miscible with water or the reagent used in the next step; (2) converting the solution to the ‘sol’ form by treating with a suitable reagent, e.g. water with HCl for oxide ceramics; (3) allowing or inducing the sol to change into a gel by polycondensation; (4) shaping the gel (or viscous sol) to the finally desired forms or shape such as thin film, fiber, spheres or grains and (5) finally converting (sintering) the shaped gel to the desired ceramic material at temperatures approximately 500 °C generally much lower than those required in the conventional procedure of melting oxides together [8]. The first step in a sol-gel reaction is the formation of an inorganic polymer by hydrolysis and condensation reactions i.e, the transformation of the molecular precursor into a highly cross-linked solid. Hydrolysis reaction results in a sol, a dispersion of colloidal particles in a liquid

and further condensation leads to a gel, an interconnected, rigid and porous inorganic network enclosing a continuous liquid phase [26, 27]. Sol-gel is one of the simplest technique to manufacture thin films. This method can provide almost any single or multi component oxide coating on glass or metal substrates. Sol gel derived coating can be employed as optical, electronic, magnetic or coating with chemical functions. Sol-gel derived ceramic films are usually used as a protected layer against corrosion and oxidation of stainless steel, Ag, Al, and Cu substrates [26]. Figure 2.5 shows the steps in the sol-gel process for ceramic materials.

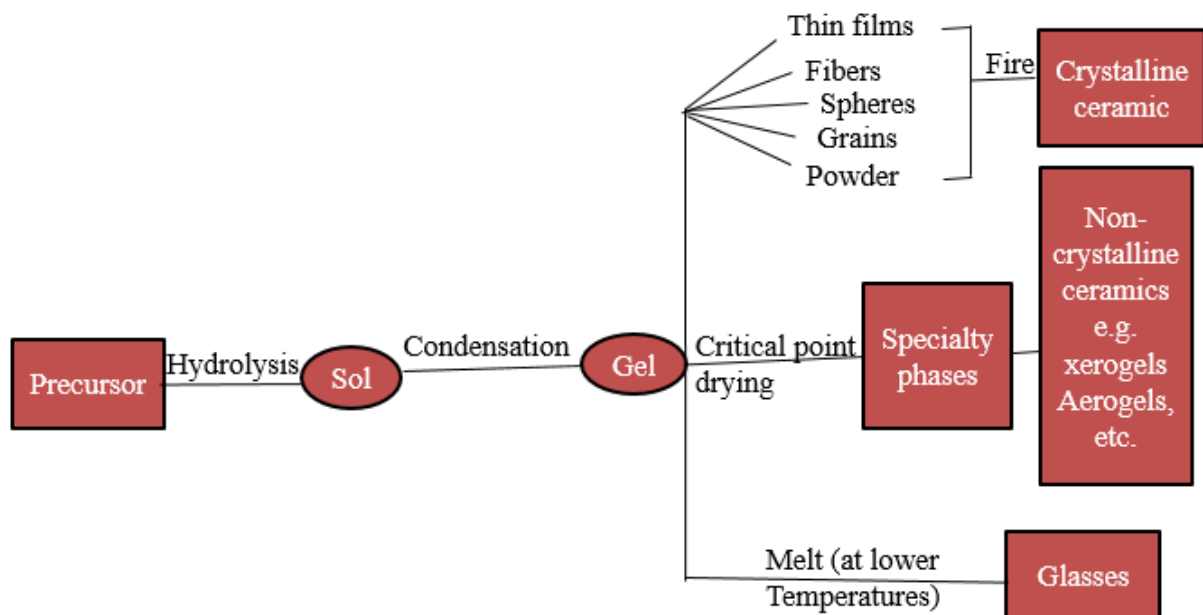


Figure 2.5: Steps in the sol-gel process for ceramic materials

The sol-gel method offers a resourceful way of synthesizing inorganic polymer and organic-inorganic hybrid materials. Sol-gel process can be applied under extremely mild conditions; therefore, it can be used to achieve products of different sizes, shapes and formats (e.g., fibers, films, monoliths, and nano-sized particles). Sol-gel technology has found increasing applications in the development of new materials for catalysis, chemical sensors, membranes, fibers, optical gain media, photochromic and non-linear applications, and in solid state electrochemical devices. The technology is utilized in a diverse range of scientific and engineering fields, such as the ceramic industry, nuclear field industry, and electronics industry [25, 26].

Sol-gel process has the following advantages:

- Better homogeneity from raw materials.
- Can produce high purity products because the organo-metallic precursor of the desired ceramic oxides can be mixed, dissolved in a specified solvent and hydrolyzed into a sol, and subsequently a gel, the composition can be highly controllable.
- Good mixing for multi-component systems.
- Effective control of particle size, shape, and properties.
- Better products from the special properties of the gel.
- The creation of special products such as films.
- The creation of new non-crystalline solids outside the range of normal glass formation.
- The fine tuning of chromatographic selectivity via the possibility of creating hybrid organic-inorganic materials.
- The possibility of designing the material structure and property through the proper selection of sol-gel precursor and other building blocks.
- The possibility of achieving enhanced stationary phase stability and performance in chromatographic separations.
- Can produce thin bond-coating to provide excellent adhesion between the metallic substrate and the topcoat.
- Can produce thick coating to provide corrosion protection performance.
- Can easily shape materials into complex geometries in a gel state.
- Can provide a simple, economic and effective method to produce high quality coatings.

Sol-gel method of fabricating thin films and nanoparticle presents several disadvantages. Despite its advantages, sol-gel technique never arrives at its full industrial potential due to some limitations, weak bonding, low wear-resistance, high permeability and difficult controlling of porosity. In addition, deposition of thin films is limited by the maximum coating thickness of 0.5 μm when the crack-free property is an indispensable requirement. The trapped organics with the thick coating often result in failure during thermal process. The present sol-gel technique is very substrate dependent, and the thermal expansion mismatch limits the wide application of sol-gel technique. This is serious limitation considering that in this work we have deposited ZnO nanoparticle for dye solar cell applications with a desired thin film thickness of 10 μm . However, the sol-gel technique can be used in preparation of the precursor solution in

combination with PSP technique to deposit the precursor solution onto the desired substrates [25].

2.8.3. PLASMA ENHANCED CHEMICAL VAPOR DEPOSITION

Plasma-enhanced chemical vapor deposition (PECVD) is a process used to deposit thin films from a gas state (vapor) to a solid state on a substrate. Chemical reactions are involved in the process, which occur after creation of a plasma of the reacting gases [28]. Plasma enhanced deposition processing can be done using electric discharge plasmas in which the energy to sustain the ionised state is supplied by an externally applied electric field. Low pressure (glow discharge) plasmas are used in most of the applications. The free electrons are energetic species in these plasmas [28].

They gain energy from the electric field faster than the ions do and are thermally isolated from the atoms and molecules, as far as elastic collisions are concerned, by the mass difference. Subsequently, the electrons accumulate sufficient kinetic energy to undergo inelastic collisions and to sustain the ionisation, while the heavy particle (molecule) temperature remains low. All types of electrical discharges have three elements in common: (1) they are sustained by a source of electric power, (2) the electric power is delivered by means of a coupling mechanism and (3) It is delivered to a plasma environment associated with a particular design [28]. The PECVD has the following advantages: high purity films can be achieved, great variety of compositions can be deposited, some films cannot be deposited with adequate film properties by any other method and good economy and process control are possible for many films. Lower substrate temperature is the major advantage of PECVD, and in fact, PECVD provides a method of depositing films on substrates that do not have the thermal stability to accept coating by other methods [29]. Regardless of its advantages PECVD has several disadvantages such as: high cost of equipment, toxic byproducts, plasma bombardment is stressful and it has small batch sizes: 1-4 wafers, one side.

2.8.4. LASER ABLATION

Laser pyrolysis is based on a resonant interaction between a laser beam and a gaseous or liquid precursor, where energy is transferred by multiphoton process between the emission line of the

laser and at least one absorption band of the precursor. An aerosol generator (ultrasonic nebulizer) produces droplets of the precursor into the laser beam. Multiphoton absorption by the precursor leads to dissociation; radicals are formed and subsequent reactions result in nanoparticles by homogeneous nucleation, exhibiting a narrow size distribution and high purity because the reaction takes place in an interaction zone without walls [30].

Laser ablation is the process of removing material from a solid (or occasionally liquid) surface by irradiating it with a laser beam. At low laser flux, the material is heated by the absorbed laser energy and evaporates or sublimates. At high laser flux, the material is typically converted to a plasma. Usually, laser ablation refers to removing material with a pulsed laser, but it is possible to ablate material with a continuous wave laser beam if the laser intensity is high enough [31, 32]. Figure 2.6 below shows a schematic representation of laser pyrolysis set up.

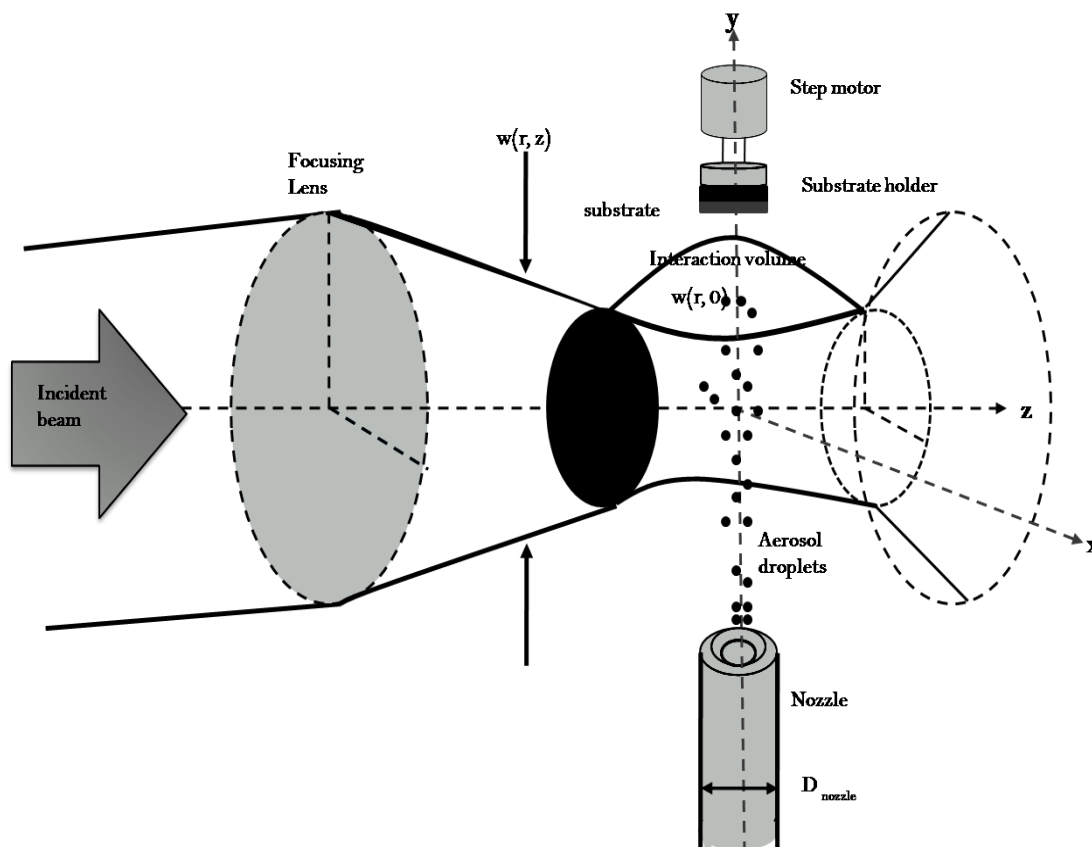


Figure 2.6: A schematic representation of laser pyrolysis set up [33].

The five most common microvia processing approaches are wet etching, reactive ion etching (RIE), laser ablation, photosensitive polymer lithography, and mechanical drilling. Laser ablation has several key advantages over the other methods, including the lowest number of process steps, the most desirable by shape for subsequent metallization steps (i.e., trapezoidal), and the capability of tight control over the wall angle (with the proper combination of focal plane ablation and tool parameters with wall angle up to 75° have been ablated). Another advantage of laser-based via generation is its high depth to diameter ratio [30, 31].

2.9. SPRAY PYROLYSIS

Spray pyrolysis is the aerosol process that atomizes a precursor solution, evaporates solvent vapour molecules in a furnace or heats source and generates semiconductor nanoparticles and thin films. This technique is often characterised as a liquid phase process because the precursor materials are in liquid form. This method can produce nanoparticles with controlled composition and morphology, good crystallinity and uniform size distribution, all of which can be readily obtained in only one step. It has been used for the past three decades as one of the major technique to deposit a wide variety of nanomaterials [43]. This technique shows a very simple and relatively cost-effective method, unlike many other film deposition techniques, such as reactive evaporation, molecular beam epitaxy, magnetron sputtering technique, pulsed laser deposition, sol-gel technique, chemical vapor deposition and electrochemical deposition. Because it has several advantages in producing nanocrystalline thin films, such as relatively homogeneous composition, simple deposition on glass substrate, low substrate temperatures involved, easy control of film thickness, fine and porous microstructure, it is suitable for large scale production [33].

The spray pyrolysis system consists of (i) a nebulizer that converts the starting solution to droplets, (ii) furnace or reactor, (iii) sample holder (i.e. filter, electrostatic precipitator, thermophoretic sampler) and an exhaust. Figure 2.7 shows the schematic diagram of PSP system.

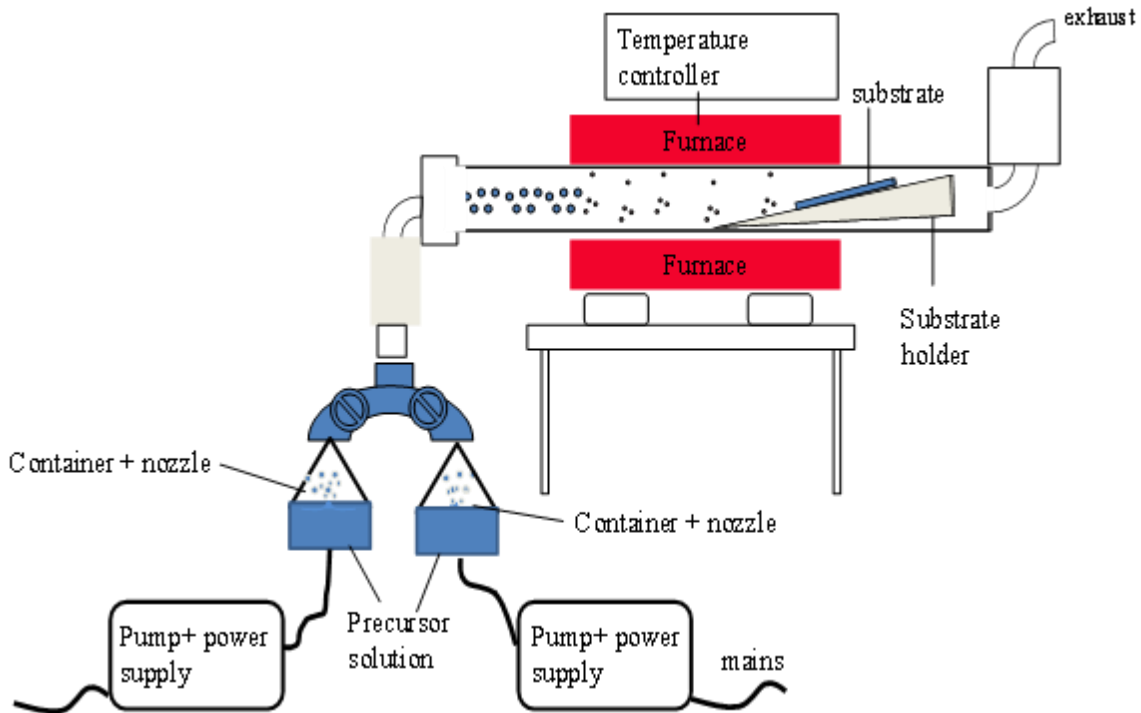


Figure 2.7: Schematic presentation of the pneumatic spray pyrolysis system [35].

There are five forms of spray pyrolysis technique which are electrostatic spray pyrolysis, flame spray pyrolysis, ultrasonic spray pyrolysis, pneumatic spray pyrolysis and low pressure ultrasonic spray pyrolysis. However, this dissertation is focusing on production of zinc oxide nanoparticles using pneumatic spray pyrolysis.

2.10. PNEUMATIC SPRAY PYROLYSIS SYSTEM.

Pneumatic spray pyrolysis system consists of a (1) Pneumatic spray pyrolysis vessel, (2) reactor (split tube furnace), (3) quartz tube as the reaction zone ,(4) Exhaust and (5) pneumatic pump, that converts the starting solution to droplets as shown here in Figure 2.7 above. Spray pyrolysis is done on the glass substrates lying horizontal on the floor of the Aluminium tube. Usually low cost materials such as nitrate, chloride and acetates are normally used as precursor solutions. The solvent that is usually used is water or alcohol. Pneumatic spray generation begins when air from the pneumatic pump is blown into the PSP vessel which contains the precursor solution to form droplets. The generated droplet of vapour are carried by the air from the pneumatic pump into the furnace or reactor. In the furnace, solvent vapour molecules evaporate as solid state semiconductor nanoparticles are formed. The semiconductor

nanoparticles are either collected on a substrate such as glass or collected in a solution. The generated nanoparticles are sintered during the solvent evaporation process. Inside the furnace the evaporation of the solvent, diffusion of solute, drying, precipitation, reaction between precursor, surrounding gas, pyrolysis, or sintering and decomposition may occur to form the solid product.

2.10.1 SPRAY PYROLYSIS VESSEL

The Figure 2.8 below shows the PSP reaction vessel used in this study. The precursor solution of zinc ethoxide is blown by the air from the pump to form mist of droplets inside the PSP vessel. The material used for the vessel provided a non-corrosive environment for housing the precursor solution of ZnO.



Figure 2.8: *Image of the PSP reaction vessel used in this study*

2.10.2 SPRAY REACTOR (SPLIT TUBE FURNACE)

Nano sized powders can be synthesized by wet chemical methods and gas phase processes. Gas phase processes are often advantageous compared to liquid phase processes since they do not require several steps like washing, drying and annealing process. Moreover, the use of high liquid volumes and surfactants, which are necessary to produce high purity materials, can be avoided [33, 35]. The tubular reactor used in spray pyrolysis provides a well-controlled temperature zone over long residence times for conversion of the precursor to the final product. The spray pyrolysis methods that employ tubular reactor systems (furnace) offer several advantages such as (a) Operation simplicity, (b) minimum through put (in terms of consumables), (c) lower thermal budget, (d) lower operation cost, (e) there is no need for subsequent heat treatment after sample synthesis. Additionally tubular reactor systems offer the opportunity of industrial scaling. Spray method draws on the advantage of the excellent spatial mixing of the reactants; the spray pyrolysis process was also established for multi component systems [34]. Figure 2.9 and Figure 2.10 shows the split tube furnace and the Aluminium tube that were employed in the synthesis of ZnO NPs respectively.



Figure 2.9: Photograph of the split tube furnace employed in the synthesis of ZnO nano structure in the study.



Figure 2.10: The aluminium reaction vessel employed in this study

2.10.3 DESIGN OF A SUBSTRATE HOLDER

The PSP system originates from the angle at which the substrate interacts with the incoming aerosol vapour. Most systems that have utilized a substrate holder with the substrate vertically parallel to the incoming aerosol beam. In our system, the substrate holder holds the substrate perpendicular to the incoming aerosol steam as shown in the schematic representation of Figure 2.11.

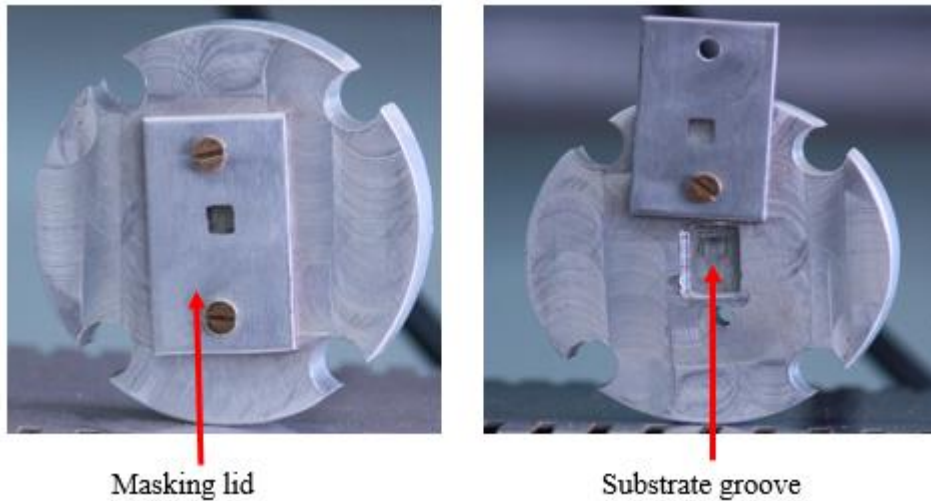


Figure 2.11: The aluminium substrate holder employed in open and closed configuration

The choice of the deposition angle $\theta = 0^\circ$ can be best explained by considering Figure 2.12 below. In this Figure the aerosol vapour stream is incident at an angle θ with the normal to the substrate surface. In most cases, the aerosol vapour stream has an incident angle, θ with respect to the substrate surface normal. At angle θ , the substrate will receive the precursor aerosol vapour stream from both the vertical and lateral directions. During pneumatic spray pyrolysis deposition of the thin film onto a flat substrate, initially the impinging nanoparticles randomly form islands on the substrate. As spray deposition proceeds, the preliminary nucleated islands act as shadowing centers and all of the tallest nanoparticle islands are expanded into columns and nano columnar films are formed [33].

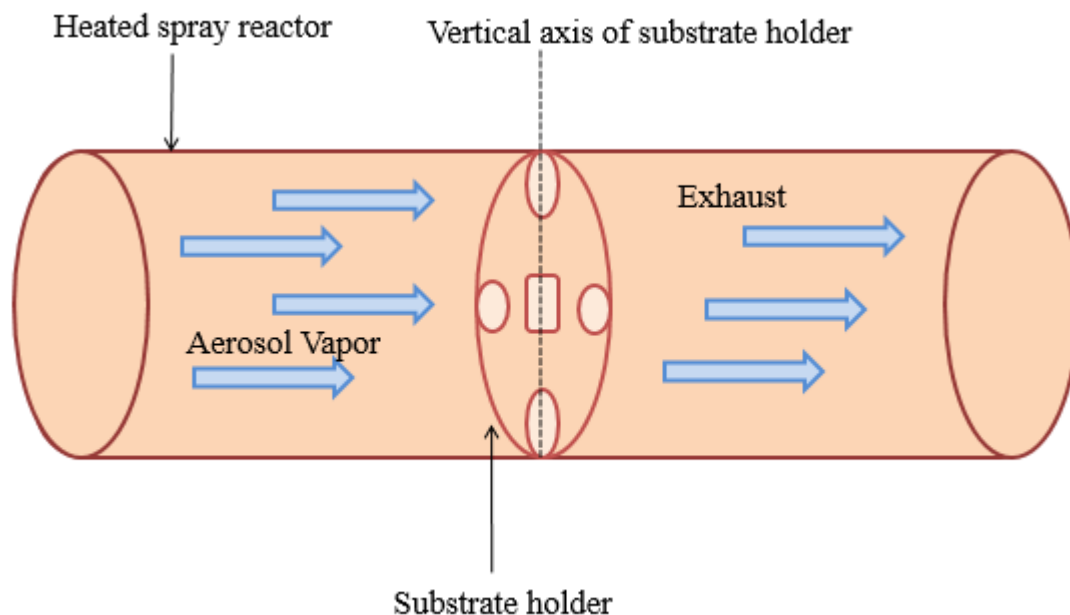


Figure 2.12: Schematic presentation of substrate holder position in the spray reactor.

2.11. PYROLYSIS OF ZINC OXIDE

Several processes occur simultaneously when a droplet strikes the surface of the substrate such as evaporation of residual solvent, spreading of the droplet, and salt decomposition. Many models exist for the decomposition of a precursor depending on the chemical environment. Viguie and Spitz proposed the following processes that occur with increasing substrate temperature [33]. At lowest temperature regime (process A) the droplet splashes onto the substrate and decomposes. The decomposition occurs at higher temperatures (process B) where the solvent evaporates completely during the flight of the droplet and dry precipitate hits the substrate [33]. Figure 2.13 shows the deposition processes initiated with increasing substrate temperature.

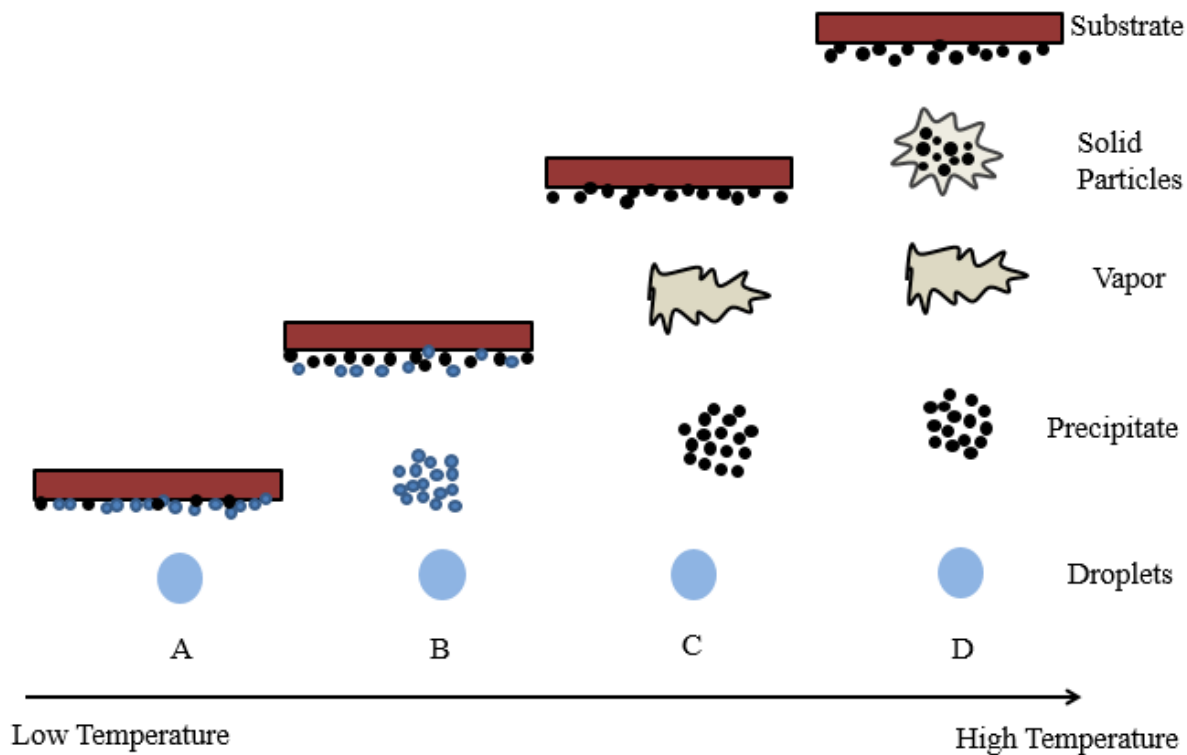


Figure 2.13: Description of the deposition processes initiated with increasing substrate temperature.

At higher temperatures (process C) the solvent also evaporates before the droplet reaches the substrate. Then the solid precipitate melts and vaporizes without decomposition and the vapor diffuses to the substrate to undergo a chemical vapor decomposition (CVD) process. The precursor vaporizes before it reaches the substrate, and consequently the solid particles are formed after the chemical reaction in the vapour phase at the highest temperatures (process D). It is assumed that the processes A and D can lead to rough or non-adherent films. At low temperatures (process C) that is where the adherent films are attained by CVD. Though, type A or B allows formation of high quality adherent films too. Furthermore, process C can scarcely occur in most spray pyrolysis depositions, because either the deposition temperature is too low for the vaporization of a precursor or the precursor salt decomposes without melting and vaporization [36].

The nebulizer can be used to atomize the precursor solution. Porous and amorphous cadmium sulphide (CdS) thin films can be obtained at temperatures below 300 °C. Powdery films can be produced due to the vaporization and decomposition of the precursor before reaching the

substrate at high substrate temperatures (> 450 °C). It can be estimated that the optimum temperature lies between 400 °C and 450 °C. The presence of large particles on the surface can be attributed to very large droplets, which might not decompose well when they arrive at the substrate [33, 36].

2.12. REACTION MECHANISMS FOR PRODUCTION OF ZINC OXIDE NANOPARTICLES

The focusing ultrasound waves of frequency f producing capillary waves of frequency f_{PSP} at the surface of the precursor solution are essentially involved in the PSP technique. This produces ultra-fine droplets of the precursor liquid. The droplet size decreases by increasing the frequency f . At higher f , the liquid is subjected to a higher number of compression phases; therefore the crest development is reduced causing the subsequent decrease of the droplets size [34]. The ultrasonic generator that is driven by a piezoelectric crystal at a fixed frequency, f was used to produce fine aerosol or medium from precursor solution by air from the pneumatic pump.

The surface of the liquid breaks down when the longitudinal waves propagate from the crystal to the liquid air interface, the pneumatic pump was used to transport the mist like aerosol, formed by various fine droplets into an oven and undergoes thermal decomposition to yield fine dispersed powder. Pneumatic spray pyrolysis method has a disadvantage of small production rate of few grams per hour [37, 38]. In this study the vapors generated from the precursor solution in the pneumatic vessel are transported to a heated zone (furnace) through an aluminium tube onto the F: SnO₂ glass substrate inside a furnace using the air from the pneumatic pump. The spray deposition was carried out for four hours. The forcing sound causes the precursor to erupt into droplets of mean diameter. The wavelength of the capillary waves will be governed by Rayleigh equation [38].

$$D_{PSP} = \left(\frac{8\pi\sigma}{\rho \cdot f_{PSP}^2} \right)^{\frac{1}{3}} \quad (2.9)$$

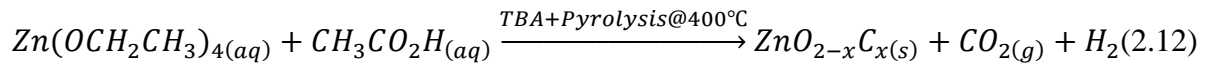
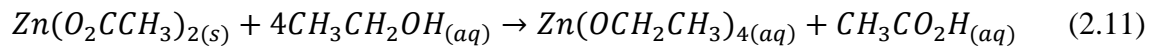
where σ the surface tension of precursor solutions

After the decomposition and deposition in the pyrolysis process the solid state particles obtained have a mean diameter that can be estimated as

$$d_{PSP} = \left(D_{PSP} \frac{C_{Pr} M_P}{\rho_P M_{Pr}} \right)^{\frac{1}{3}} \quad (2.10)$$

where C_{Pr} is the concentration of the precursor M_{Pr} and M_P are the molar masses of the precursor and deposited particles respectively ρ_P and ρ_{Pr} are the densities of the deposited particles and precursor liquid respectively [33, 39].

The chemical reaction sequence for production of C-ZnO NPs is similar to that proposed by Livage [34, 37] in the production of vanadium oxide NPs and more similar to the one adopted by Taziwa et al [33, 40] in the production of carbon doped titanium dioxide NPs and is as follows:



2.13. PRECURSOR

The precursor solution is one of the most important process variable in PSP technique. The physical and chemical properties of the precursor can be influenced by solvent, type of salt, concentration of salt and additives. Therefore, structure and properties of a deposited film can be tailored by changing composition of precursor solution. Pneumatic pump can be used to blow the precursor solution into an aluminium tube inside the furnace. The air from the pump makes the solutions to be aerosol and the aerosol can be transported to the substrate using the PSP pump at a desired flow rate, and the substrate can be kept at higher temperatures maybe about 500 °C [42]. In previous studies an aqueous precursor solution was used that contained polymerizable organic monomers with a radical initiator, colloidal silica nanoparticles and surfactant. In some cases a small amount of dicobalt octacarbonyl $[\text{Co}_2(\text{CO})_8]$ was also added to produce magnetic nanospheres [34]

2.14. PNEUMATIC SPRAY PYROLYSIS MECHANISMS

In order for the droplet to be formed, the liquid must have sufficiently high velocity of ejection. Very small droplet size can be produced by increasing the frequency hence the frequency of pneumatic vibration determines the droplet size in pneumatic atomization. The splitting of liquid occurs to form droplets and they are ejected from the liquid pneumatic source interface into the surrounding air as a very fine dense mist. This happens when a liquid is subjected to sufficiently high intensity of pneumatic field as shown in the Figure 2.14 below [44].

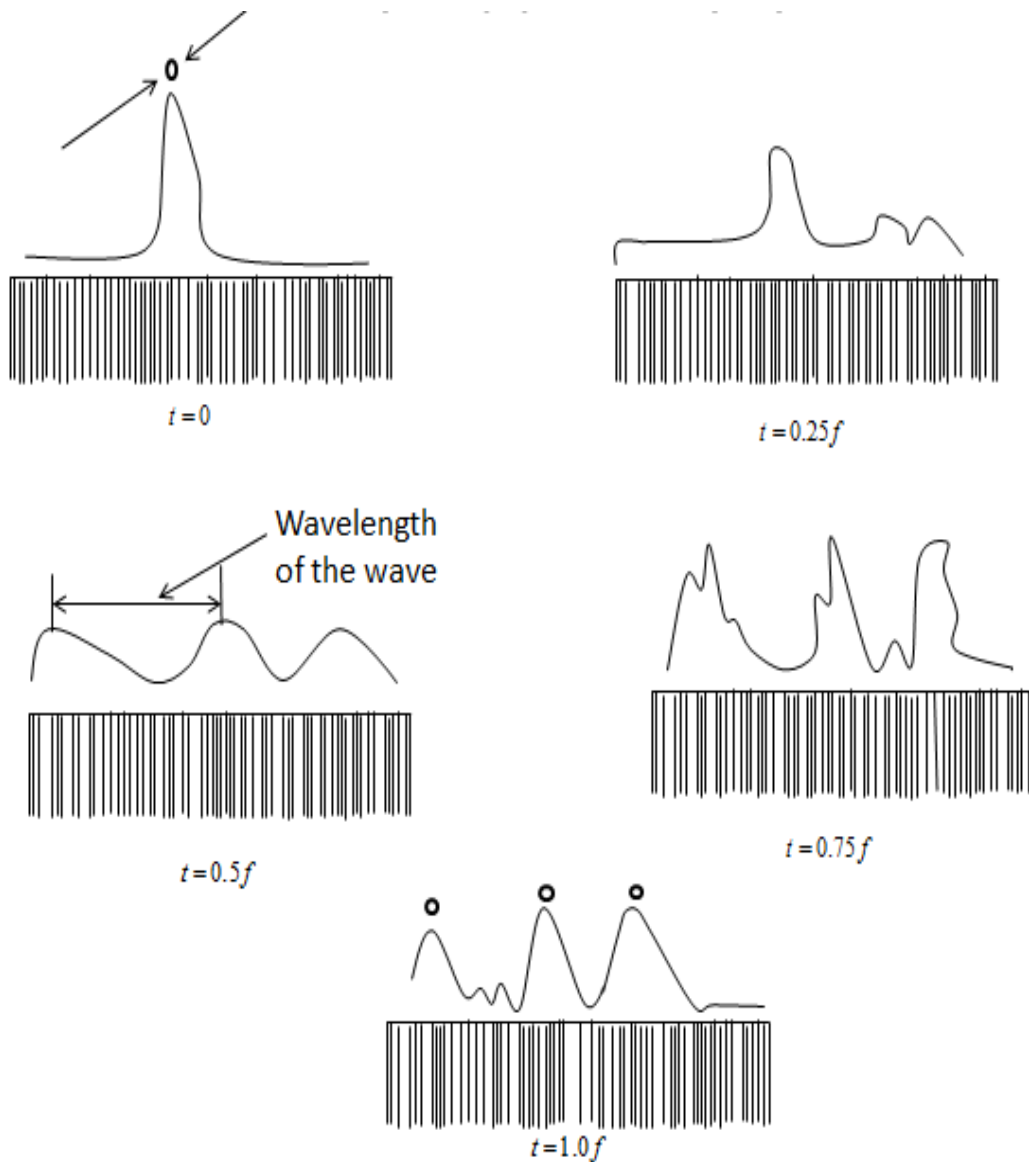


Figure 2.14: Schematic representation of the droplet formation from the standing wave crests displaying one period of wall vibration.

Pneumatic spray pyrolysis is a low priced method and quite a versatile technique for nanoparticle production. This method is based on an aerosol process to yield fine metallic, oxidic, composite nanoparticles of accurately controlled morphology and well-defined chemical compositions from aqueous solution using different metal salts and their mixture. This technique can be used for the preparation of metallic, oxidic and composite nanopowders from different organic and inorganic salts as precursor materials [45]. Fine grained, dense, porous or core-shell nanoparticles, which include metal oxide, sulfides, composites and especially metal can be produced by pneumatic spray pyrolysis, since it is possible to run the process under a reductive atmosphere.

PSP method has the advantage of ideally spherical particle, continuous and sample handling process with high flexibility of process parameter control and it has the disadvantage of small production rate of few grams per hour [45, 46]. Particularly in this method, spraying is done by the application of high frequency ultrasound to the precursor solution which in turn forms aerosols with constant droplet size and is dependent on the characteristic of the liquid and the frequency of the atomizer. The experience in nanoparticles synthesis by (PSP) was the basis to develop a system for industrial scale production [45]. The main features of the demonstration scale pneumatic spray pyrolysis are: aerosol pneumatic generator, high-temperature furnace with five wall heated reactors, electrostatic filter and vacuum system. The liquid sheet can be disrupted into droplet when the high velocity air imparts its energy to the liquid. Finer droplets with high sphericity and uniform size distribution can be achieved if the energy for liquid sheet fragmentation can be supplied by the use of pneumatic energy [47]. Pneumatic atomization is the ejection of fine droplets from a liquid film formed on an ultrasonically vibrating surface. A normal pneumatic atomizer contains a vibrating plate with a concentric hole for passage of the liquid. Sprays of very small droplets are appropriately produced by pneumatic atomization. Other traditional mechanical methods, like pressure or gas-assisted systems are not advantageous to generate sprays of very small droplets compared to pneumatic atomization because it has some specific characteristics that make it more valuable [45, 46, 48].

The physico-chemical properties such as density, viscosity and surface tension can be used to specify the droplet size controlled by pneumatic frequency for a liquid at a specific flow rate. Very small droplet size can be produced by increasing the frequency hence the frequency of pneumatic vibration determines the droplet size in pneumatic atomization [45, 46, 47]. Pneumatic atomization is a very productive method of generating small droplets. Nano powders are formed after the droplets have been generated. There are three approaches that are common in this technique. This includes (1) passing the flow of the liquid across standing pneumatic wave; (2) depositing the liquid over a pneumatic transducer; and (3) immersing a focusing pneumatic transducer in the liquid in such a way that the depth of liquid is equal to the focal length of the ultrasound lenses in the transducer [47, 49, 60].

The possibility of generating a cloud of droplets by means of pneumatic waves was first reported by Wood and Loomis (1927). There are two major mechanisms that are used for the ejection of the droplets from a vibrating surface which are capillary wave mechanism and

cavitation mechanism. The droplet size depends on the pneumatic frequency, and hence it is possible to generate droplets in the micron range by using MHz-order driving frequencies. With higher frequencies, capillary waves are excited on the free surface primary drop at shorter wavelengths, destabilization of these waves then results in smaller atomized droplets [47, 50]. Usually, around 5 mm frequencies in the MHz range are required to generate droplets enough to be inhaled in medical applications [48].

2.14.1 CAPILLARY WAVE MECHANISM

The droplet size can be estimated using the Lang equation when majority of the droplets are formed by the capillary wave mechanism [47, 48, 66]. Capillary wave mechanism is based on Taylor instability. The instability is the formation of capillary waves composed of crests and troughs on the vibrating surface. When the amplitude of the ultrasound is above the threshold value the droplets are ejected from the crests. Capillary waves are captured on the surface of the atomizer [46, 49, 54]. The atomization occurs when the unstable oscillations or vibrations tear off the crests of the capillary waves away from the bulk of the liquid body. Therefore, the droplets whose sizes are proportional to wavelength are produced at the crest. Figure 2.15 presents the schematic diagram of droplet generation at the crest of capillary waves.

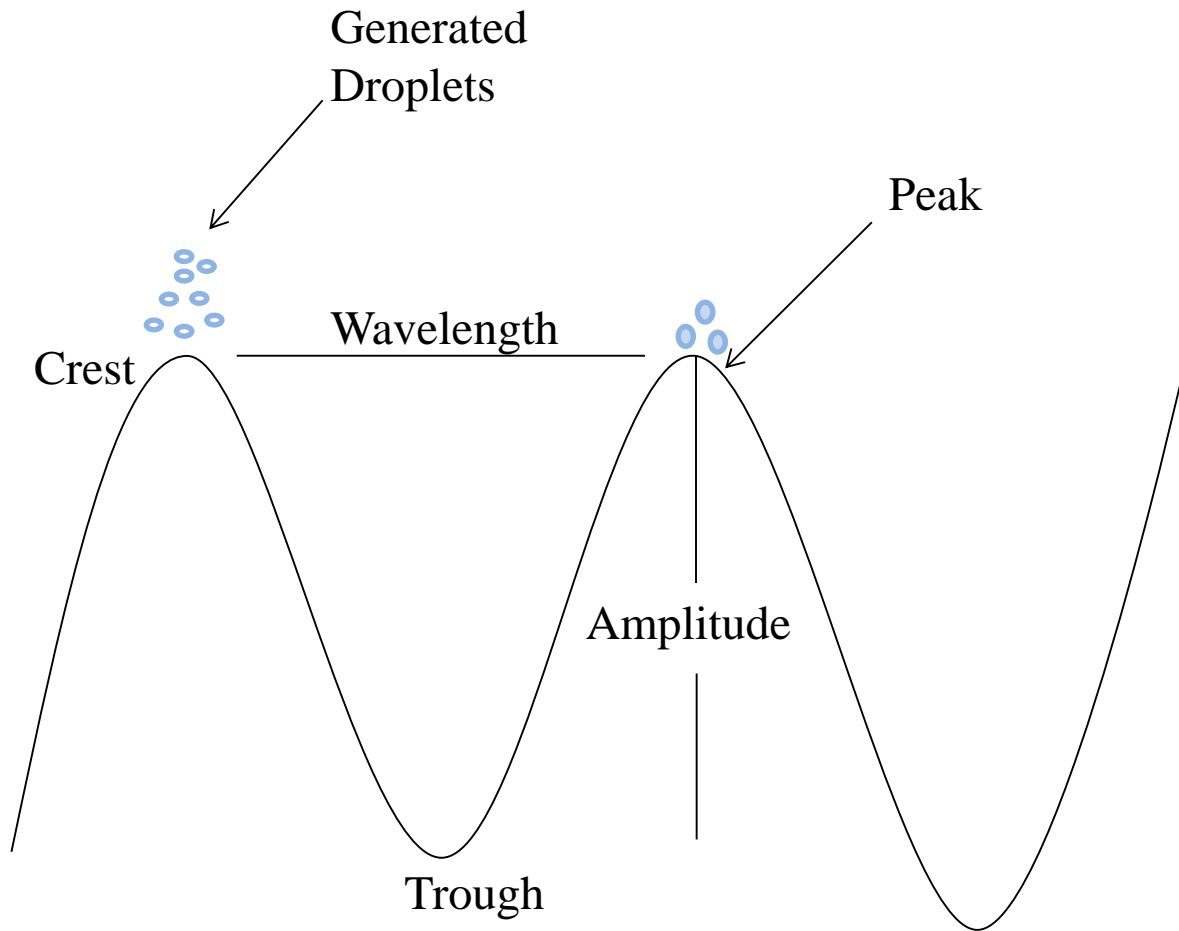


Figure 2.15: Schematic presentation of droplet generation at the crest of capillary waves.

The production of fine droplets at higher frequencies is the result of the capillary wavelength decrease with an increase in frequency of ultrasound. For sonically generated capillary waves whose wavelength can be calculated using Kelvin's equation, the surface wave frequency in this equation is equal to one half the exciting sound frequency. Roughly, 90% of the droplets were found to be smaller than twice the number median diameter as reported by Lang. Capillary wavelength indicates that the droplet size is a constant fraction of the capillary wave and this turned out to be 0.34 as compared to the number mean diameter [46, 50, 55, 66]. Correlation below has been proposed by Lang.

$$dp = 0.34 \left(\frac{8\pi\sigma}{\rho f} \right)^{\frac{1}{3}} \quad (2.13)$$

where σ is the surface tension (dyne/cm), ρ is density (g/ml), f is excitation frequency (Hz) and dp is the droplet size (cm). Lang's correlation indicates no dependence of liquid phase viscosity and the volumetric liquid flow rate which is contrary to the experimental observations.

$$dp = 0.34\lambda \quad (2.14)$$

The droplet produced can have a definite distribution as there is a variation as to how much portion of surface wave peak is ejected as droplet. The deviation can be due to collision and agglomeration of droplets after being ejected from the liquid surface. There is no dependence of liquid phase viscosity and volumetric flow rate which is opposing to experimental observations as indicated by Lang's correlation. It has been noticed that Lang's correlation is applicable only when the liquid flow rate has no effect on droplet size [52, 56, 59]. The particle size depends also on the vibration intensity. Usually, the particle sizes become large at high intensity vibration level [52, 53, 58]. This is not always true as there are experimental observations indicating a dependence on liquid phase viscosity and volumetric flow rate.

Faraday reported the first study on stationary waves of the free surface of a liquid mass subjected to periodic vertical forcing in 1831. The known equation for capillary waves was derived by Kelvin in 1871 [53, 56].

$$\lambda = \left(\frac{2\pi\sigma}{\rho f^2} \right)^{\frac{1}{3}} \quad (2.15)$$

where λ is the wavelength, σ is the surface tension coefficient, ρ is the liquid density, and f is the frequency of the surface waves. In 1883, Kelvin's equation was modified by Rayleigh in his research where he derived the expression.

$$\lambda = \left(\frac{8\pi\sigma}{\rho F^2} \right)^{\frac{1}{3}} \quad (2.16)$$

where F is the forcing sound frequency. It is to be noted that the relation $f = F/2$ was obtained empirically from experimental measurements [49, 61, 63]. An empirical equation to predict the droplet size (dp) at high liquid flow rates was proposed which is expressed as follows:

$$dp = 31.7 \left[\frac{\sigma}{\rho} \right]^{0.34} \cdot \eta^{0.03} \cdot Q^{0.139} \quad (2.17)$$

Here η is the liquid viscosity (cp) and Q is the volumetric flow rate (lpm). This correlation is dimensional in nature and is less than satisfactory as it does not account for the excitation frequency and the amplitude of oscillation [47, 61, 65].

The operating parameters such as the flow rate and the liquid properties on the droplet size have been considered and also the effect of different equipment parameters such as frequency and power dissipation have been studied. Photographic analysis based on the capture of the sudden ejection droplets with high velocity has been used for some mechanistic details about the atomization phenomena. The change in equipment and operating parameters in ultrasonic atomization can be used to obtain a good control over the droplet size [49, 51, 61].

2.14.2 CAVITATION MECHANISM

Cavitation theory is generally applied to high frequency and high energy intensity system and is essential in explaining the capillary wave hypothesis. The cavitation bubbles are formed through the implosive collapse of the generated liquid bubbles close to the surface of the liquid when a liquid is exposed to an intense ultrasound field. High intensity hydraulic shocks are generated which in turn start to breakdown into droplets. At large intensities, the excitation is outside the liquid surface but spreads into the liquid bulk, contrary to the capillary hypothesis. Properties of the liquid such as viscosity come into play as parameters affecting the nature of the final droplet [46, 51, 53].

Cavitation mechanism is essentially the formation of cavity bubbles in the liquid film on the surface of atomizer. Direct ejection of the droplets with very high velocity is the outcome of collapse of these bubbles especially near the surface. Rajan and Pandit (2001) noticed that the cavitation hypothesis is generally applied to high frequency and high energy intensity systems [47, 61, 65]. Cavitation bubbles are formed when a liquid film is sonicated. High intensity hydraulic shocks are generated during the implosive collapse of these bubbles, especially nonlinearly oscillating small bubbles near the surface of the liquid. Dimensionless numbers can

be used to resume the effect of the forces acting on the liquid as shown by the following equations:

$$Re = \frac{\rho \cdot u \cdot dp}{\mu} \quad (2.18)$$

$$We = \frac{\rho \cdot u^2 \cdot dp}{\sigma} \quad (2.19)$$

$$Oh = \sqrt{\frac{We}{Re}} = \frac{\mu}{\sqrt{\rho \cdot dp}} \quad (2.20)$$

Re = Reynolds number; We = Weber number; Oh = Ohnesorge number; ρ = liquid density; u = liquid velocity; dp = jet diameter (primary atomization) or drop diameter (secondary atomization); μ = liquid viscosity; σ = surface tension.

The Reynolds number expresses the ratio between inertial and viscous forces. The Weber number is a measure of the relative importance of the fluid's inertia compared to its surface tension. By combining the two dimensionless numbers to eliminate the liquid velocity, the Ohnesorge number, containing fluid properties, is obtained. Thus, droplets diameter can be predicted by correlations mainly based on liquid properties (density, viscosity, surface tension), on atomizer geometry (orifice size) and on operative parameters, such as liquid flow rate [54, 48, 66].

2.15. CONCLUSION

This chapter has provided an introduction on the structural, optical and morphological properties of zinc oxide including its applications. This chapter has presented in detail the theoretical background of the research techniques that are used for the synthesis of zinc oxide nanoparticles with their advantages and short comings. This chapter has also presented the essential theoretical frame work of spray pyrolysis. Furthermore the various forms of spray pyrolysis have been mentioned but not discussed into detail. Moreover, the PSP technique parameters used in this study are also mentioned and discussed in detail on how they work. Additionally, the design and structure of the PSP technique and how it operates are also offered. Lastly the chapter presents the mechanisms governing the generation of droplets such as capillary wave hypothesis and cavitation hypothesis.

2.16. REFERENCES

1. T. S. Vijayakumar, S. Karthikeyeni, S. Vasanth, A. Ganesh, G. Bupesh, R. Ramesh, P. Subramanian, Synthesis of Silver-Doped Zinc Oxide Nanocomposite by Pulse Mode ultrasonication and Its characterization Studies, *J.Nanosci.*, 2013 (2013) 1–7.
2. X. Zhang, J. Qin, R. Hao, L. Wang, X. Shen, R. Yu, R. Liu, Carbon-Doped ZnO Nanostructures: Facile Synthesis and Visible Light Photocatalytic Applications, *J. Phys. Chem. C*. 119 (2015) 20544–20554.
3. G. Kenanakis, N. Katsarakis, E. Koudoumas, Influence of precursor type, deposition time and doping concentration on the morphological, electrical and optical properties of ZnO and ZnO:Al thin films grown by ultrasonic spray pyrolysis, *Thin Sol. Film.*, 555 (2014) 62–67.
4. A. Kolodziejczak-Radzimska, T. Jesionowski, Zinc Oxide—from Synthesis to Application: A Review. *Mater.* 7. (2014) 2833–2881.
5. N. S. Kumar, K. V. Bangera, G. K. Shivakumar, Effect of annealing on the properties of zinc oxide nanofiber thin films grown by spray pyrolysis technique, *Appl. Nanosci.*, 4 (2014), 209-216.
6. S. Ozturk, N. Kılınc, N. Tasaltın, Z.Z. Ozturk, Fabrication of ZnO nanowires and nanorods, *Physica E: Low-dimensional Systems and Nanostructures* 44 (2012) 1062-1065.
7. H. Ghaffarian, M. Saiedi, M. A Sayyadnejad, Synthesis of ZnO Nanoparticles by Spray Pyrolysis Method, *Iran. J. Chem. Chem. Eng*, 30 (2011) 1–6.
8. M. M. Nmaya, Effect of quantum confinement, surface states and excitonic energy levels on photoluminescence of zinc oxide nanostructures, *J Phys. Chem.*(2014) 1-5.
9. R. Kumari, A. Sahai, N. Goswami, Effect of nitrogen doping on structural and optical properties of ZnO nanoparticles. *Progress in Natural Sci: Mater. Int.*, 25 (2015) 300–309.
10. M. Schumm, ZnO-based semiconductors studied by Raman spectroscopy: semimagnetic alloying, doping, and nanostructures, 2008, [PhD Thesis], Julius– Maximilians– Universität Würzburg, Germany.
11. G. L. Kabongo, Luminescence investigation of zinc oxide nanoparticles doped with rare earth ions, 2013, [MSc thesis], University of South Africa.
12. C. Charpentier, P. Prod, I. Maurin, M. Chaigneau, P. R. Cabarrocas, X-Ray diffraction and Raman spectroscopy for a better understanding of ZnO : Al growth process, *J. Mater. Chem.* 89 (2011) 25002.

13. H. Morkoc, U. Ozgur, General Properties of ZnO. Fundamentals, Materials and Device Technology, 2009.
14. D. Zhang, M. Wang, J. Ma, G. Han, S. Li, Enhanced photocatalytic ability from carbon-doped ZnO photo-catalyst synthesized without an external carbon precursor, F. Mater Lett. 7 (2014) 1-7
15. C. Yu. W. Lan, K. Huang, Indium-nitrogen Co-doped zinc oxide thin film deposited by ultrasonic spray pyrolysis on n-(111) Si substrate: the effect of film thickness, J. Nanomater. 2014 (2014) 1-5.
16. A. Bagabas, A. Alshammari, M.F. Aboud, H. Kosslick, Room-temperature synthesis of zinc oxide nanoparticles in different media and their application in cyanide photo-degradation, Nanoscal. Res. Lett. 8 (2013) 516.
17. K. Rajendran, S. Senthilkumaar, S. Banerjee, T. K. Chini, V. Sengodan, Influence of Mn doping on the microstructure and optical property of ZnO. Mater. Sci. Semiconductor Processing, 11 (2008) 6– 12.
18. S. Aydin, G. Turgut, M. Yilmaz, M. Ertrugul, Fabrication of ZnO nanorods by simplified spray pyrolysis. Bitlis Eren University J. Sci. Technol. 1 (2011) 1–3.
19. B. Godbole, N. Badera, S. Shrivastava, D. Jain, V. Ganesan, Growth Mechanism of ZnO Films Deposited by Spray Pyrolysis Technique, Mater. Sci. Appl. 2 (2011) 643–648.
20. P. S. Patil, Versatility of chemical spray pyrolysis technique, Mater. Chem. Phys., 59 (1999) 185-273. A. Aimable, M. T. Buscaglia, V. Buscaglia, P. Bowen, Polymer-assisted precipitation of ZnO nanoparticles with narrow particle size distribution, J. Euro. Ceramic Soc. 30 (2010) 591–598.
21. S. Benramache, B. Benhaoua, H. J. Bentrah, Preparation of transparent, conductive ZnO:Co and ZnO:In thin films by ultrasonic spray method, J. Nanostruc. Chem. 3 (2013) 54.
22. J. Carlsson, Chemical Vapor Deposition. Handbook of deposition technologies for films and coatings, Chem. Phys. Lett. 49 (2010) 400–459.
23. J. R. Creighton, P. Ho, Introduction to chemical vapor deposition (CVD). chemical vapor deposition, Chem. Int. Ed. 250 (2001) 1–13.
24. K. Choy, Chemical vapour deposition of coatings. Progress in Mater. Sci. 48 (2003), 57–170.
25. T. K Tseng, Y. S. Lin, Y. J. Chen, H. A. Chu, A review of photocatalysts prepared by sol-gel method for VOCs removal. Int. J. Molecular Sci. 11 (2010), 2336–2361.

26. Niederberger, M. Aqueous and nonaqueous sol-gel. metal oxide nanoparticles in organic solvents, *Acc. Chem.Res.*, 40 (2007) 793-800.
27. S. Attia, J. Wang, G. Wu, J. Shen, J. Ma, Review on sol-gel derived coatings: process, techniques and optical applications. *J. Mater. Sci. Technol.* 18 (2002) 211-217.
28. P. Carey, Plasma enhanced chemical vapour deposition of thin carbon films, 1989, [MSc thesis], School of Electronic Engineering, Dublin City University
29. A. Boogaard, Negative charge in plasma oxidized SiO₂ layers, *ECS trans.* 35 (2011) 259-272.
30. R. Setia, Modeling and diagnosis of excimer laser ablation. *Biomolecular Eng.* 13 (2005) 1-5.
31. M. S. Brown, C. B. Arnold, Laser precision microfabrication. *Springer Series in Mater. Sci.* 135 (2010), 91–120.
32. D. Von der Linde, K. Sokolowski-Tinten, Physical mechanisms of short pulse laser ablation, *Appl. Surf. Sci.* 10 (2000) 154–155.
33. R. Taziwa, E. Meyer, Carbon doped nano-crystalline TiO₂ photo-active thin film for solid state photochemical solar cells, *Adv. Nanopart.* 3 (2014) 54–63.
34. W. H. Suh, K. S. Suslick, Magnetic and porous nanospheres from ultrasonic spray pyrolysis, *J. Am. Chem. Soc.* 127 (2005) 12007–12010.
35. B. Ebin, S. Gurmen, Synthesis and characterization of nickel particles by hydrogen reduction assisted ultrasonic spray pyrolysis (USP-HR) method, *KONA Powd. Part. J.* 29 (2011), 134-140.
36. D. Perednis, L. J. Gauckler, Thin film deposition using spray pyrolysis, *J. Electroceramics.* 14 (2005) 103–111.
37. A. Dalmoro, M. d'Amore, A. A Barba, Droplet size prediction in the production of drug delivery microsystems by ultrasonic atomization, *Transl Med UniSa.* 7 (2013) 6-11.
38. J. Bogovic, A. Schwinger, S. Stopic, J. Schroeder, V. Gaukel, H. P. Schuchmann, B. Friedrich, Controlled droplet size distribution in ultrasonic spray pyrolysis, *Mater. Sci. Eng.* 65 (2011), 455-459.
39. B. W. Mwakikunga, Progress in ultrasonic spray pyrolysis for condensed matter sciences developed from ultrasonic nebulization theories since michael faraday, *Critical Reviews in Sol. Stat. Mater. Sci.* 39 (2014) 46-80.
40. C. Matei Ghimbeua, R.C. Van Landschoot, J. Schoonman, M. Lumbreras, Preparation and characterization of SnO₂ and Cu-doped SnO₂ thin films using electrostatic spray deposition (ESD). *J. Euro. Ceramic Soc.* 27 (2007) 207–213.

41. K. C. Pingali, D. Rockstraw, S. Deng, Silver nanoparticles from ultrasonic spray pyrolysis of aqueous silver nitrate. *Aerosol Sci. Technol.* 39 (2005), 1010–1014.
42. C. H. Hsu, L. C. Chen, X. Zhang, Effect of the Cu source on optical properties of CuZnO films deposited by ultrasonic spraying. *Mater.* 7 (2014) 1261–1270.
43. S. Benramache, B. Benhaoua, H. J. Bentrach, Preparation of transparent, conductive ZnO:Co and ZnO:In thin films by ultrasonic spray method, *J. Nanostruct. Chem.* 3 (2013) 54.
44. G. Matula, J. Bogovic, S. Stopic, B. Friedrich, Scale up of ultrasonic spray pyrolysis process for nano-powder production, *J. Phys. Chem.* (2013) 1-5.
45. J. Bogovic, A. Schwinger, S. Stopic, J. Schroeder, V. Gaukel, H. P. Schuchmann, B. Friedrich, Controlled droplet size distribution in ultrasonic spray pyrolysis, *Mater. Sci. Eng.* 65 (2011), 455-459.
46. R. Rajan, A. B. Pandit, Correlations to predict droplet size in ultrasonic atomization, *J. Phys Chem.* 39 (2001) 235-55.
47. A. Lozano, H. Amaveda, F. Barreras, X. Jorda, M. Lozano, High-frequency ultrasonic atomization with pulsed excitation, *J. Fluids Eng.* 125 (2004), 941-945.
48. F. Barreras, H. Amaveda, A. Lozano, Transient high-frequency ultrasonic water atomization, *Nature J. Editors.* 33 (2002) 405–413.
49. M. Alvarez, J. Friend, L. Yeo, L. D. Arifin, Microaerosol and nanoparticle synthesis for drug delivery via surface acoustic wave atomization, 2007, 16th Australasian Fluid Mechanics Conference, Crown Plaza, Gold Coast, Australia (621–624).
50. K. A. Ramisetty, K. Das, P. R. Gogate, A. B. Pandit, Investigations into ultrasound induced atomization, *Ultrasonics Sonochem.* 20 (2013), 254-264.
51. R. J. Lang, Ultrasonic atomization of liquids, *J Acoustic Soc Am*, 34 (1962) 6-8.
52. M. Kurosawa, A. Futami, T. Higuchi, Characteristics of liquids atomization using surface acoustic wave, *Mech. Eng.* 2 (1997) 801–804.
53. V. R. Shinde, T. P. Gujar, C. D. Lokhande, LPG sensing properties of ZnO films prepared by spray pyrolysis method: Effect of molarity of precursor solution. *Sensors and Actuators, B: Chem.* 120 (2006) 551–559.
54. Z. L. Wang, Zinc oxide nanostructures: growth, properties and applications. *J. Phys. Condensed Matt.*, 16 (2004) 829–858.
55. D. Zhang, M. Wang, J. Ma, G. Han, S. Li, Enhanced photocatalytic ability from carbon-doped ZnO photocatalyst synthesized without an external carbon precursor, *Mater. Lett.* 7 (2014) 2–5.

56. Y. Qiu, H. Fan, G. Tan, M. Yang, X. Yang, S. Yang, Effect of nitrogen doping on the photo-catalytic properties of nitrogen doped ZnO tetrapods. *Mater. Lett.* 131 (2014) 64–66.
57. A. Dalmoro, M. d'Amore, A. A Barba, Droplet size prediction in the production of drug delivery microsystems by ultrasonic atomization, *Transl Med UniSa.* 7 (2013) 6-11.
58. S. Ebin, S. Gurmen, synthesis and characterization of nickel particles by hydrogen reduction assisted ultrasonic spray pyrolysis (USP- HR) method, *KONA Powd. Part. J.* 29 (2011) 134-140.
59. M. C. Ghimbeu, R. C. van Landschoot, J. Schoonman, M. Lumbreras, Preparation and characterization of SnO₂ and Cu-doped SnO₂ thin films using electrostatic spray deposition (ESD), *J. Euro. Ceramic Soc.* 27 (2007) 207–213.
60. H. K. Grossmann, A. Grohn, F. Meierhofer, U. Fritsching, K. Wegner, L. Madler, Experimental characterization of the double flame spray pyrolysis process based on the deposition of Pt on a TiO₂ support, *J Nanopart Res.* 17 (2015) 1-16.
61. G. Korotcenkov, V. Brinzari, J. Schwank, M. Dibattista, A. Vasiliev, Peculiarities of SnO₂ thin film deposition by spray pyrolysis for gas sensor application, *Sensors and Actuators B: Chem.* 77 (2001), 244-252.
62. G. L. Messing, S. Zhang, G. V. Jayanthi, Ceramic powder synthesis by spray pyrolysis, *J. American Ceramic Soc.* 26 (1993), 2707.
63. K. Okuyama, W. I. Lenggoro, Preparation of nanoparticles via spray route, *Chem. Eng. Sci.* 58 (2003), 537-547.
64. D. Perednis, L. J. Gauckler, Thin Film Deposition Using Spray Pyrolysis, *J. Electroceramics*, 14 (2005) 103–111.
65. S. Stopic, P. Dvorak, B. Friedrich, Synthesis of spherical nanosized silver powder by ultrasonic spray pyrolysis, *Mater. Sci. Eng.* 6 (2006) 299-304.
66. W. N.Wang, Y. Itoh, I. W. Lenggoro, K. Okuyama, Nickel and nickel oxide nanoparticles prepared from nickel nitrate hexahydrate by a low pressure spray pyrolysis, *Mater. Sci. Eng. B*, 111 (2004) 69–76.

CHAPTER 3

METHODOLOGY

3.1. INTRODUCTION

This chapter provides a detailed report on the synthesis of zinc oxide (ZnO) nanoparticles by pneumatic spray pyrolysis (PSP) technique. It starts off by providing the reagents and raw materials used for the synthesis of both un-doped and carbon doped ZnO nanoparticles. The substrate cleaning procedure used in this research is presented into detail. Furthermore, the chapter presents the actual experimental procedure for fabrication of zinc oxide nanoparticles by PSP technique. Finally, this chapter provides a brief background of the analytical techniques that were used for characterization of the un-doped and carbon doped ZnO samples synthesized by pneumatic spray pyrolysis (PSP) and annealed at 400 °C. The synthesized samples were investigated for their optical, structural and morphological properties using XRD, SEM, HRTEM, RS, UV-Vis and FTIR.

3.2. EXPERIMENTAL

3.2.1. REAGENTS AND RAW MATERIALS

Analytical grade solid zinc acetate dihydrate [$\text{Zn}(\text{CH}_3\text{COO})_2 \cdot 2\text{H}_2\text{O}$] was used. Other reagents and chemicals that were used are tetrabutylammonium (TBA), ethanol (99.99% Aldrich), acetone (Aldrich), and acetic acid (CH_3COOH). The carbon doped and un-doped ZnO nanoparticles were deposited on the fluorine doped tin oxide (F: SnO_2) transparent glass substrate. This type of glass at temperatures less than 600 °C, has a lower cut-off wavelength (approximately 280 nm), which is far away from that of bulk zinc oxide (approximately 388 nm) and also not expensive which makes the produced nanoparticles and thin films more attractive for solar applications. Before the use of glass substrate, it was first washed as mentioned in 3.2.2 below. Then dried nanoparticle deposition was done on the F: SnO_2 glass

substrate at the furnace temperatures of 400 - 405 °C, at the same substrate positions inside the furnace using a pneumatic pump at a flow rate of 5-6 L/min. The PSP experimental set up is illustrated in Figure 3.1. The spray pyrolysis consist of a furnace (REX D100 supplied by RKC instruments, Inc., Tokyo, Japan) the carrier gas unit and exhaust.

3.2.2. SUBSTRATE CLEANING PROCEDURE

The clean substrate is needed for the base material to deposit the film on and also the source is needed for the film material. The substrates used are bare glasses. Only one type of substrate was used in this project which is the fluorine doped tin oxide (F: SnO₂). The F: SnO₂ glass substrates was carefully cut into pieces for the development of carbon doped and un-doped ZnO nanoparticles and thin film photo-electrodes. The developed substrate was fitted perfectly into the groove of the aluminium substrate holder illustrated in Chapter 2 Figure 2.11. Before deposition, the F: SnO₂ glass substrate was first washed with detergent, to remove any paraffin, and then thoroughly rinsed with hot tap water, then with soap, distilled water and at last abundantly rinsed by acetone, for eliminating any greasy track. Finally, they were dried in nitrogen gas at a flow rate of 5-6 L/min. Cleaning of the substrate is a critical factor for both correct homogeneity and adhesion of the future coating deposited over them and it is absolutely necessary to follow strict cleaning protocols in order to ensure there are no impurities on the surface of the substrate.

3.3. OPERATION OF THE PSP SYSTEM

Table 3.1 outlines the standard deposition parameters for the precursors chosen.

Table 3.1: Showing operation conditions for PSP system

PROCESS PARAMETERS	PNEUMATIC SPRAY PYROLYSIS
	@400°C
PSP pump air flow rate	5-6 ml/min
PSP vessel pressure (Atm)	1
Precursor temperature (°C)	25
Precursor pH	1.27
Substrate type & temperature (°C)	Glass /400 °C
Deposition time (h)	4

Deposition Angle (°)	90
Annealing temperature (°C)	400

Pneumatic spray pyrolysis may be employed to generate an aerosol from a dilute aqueous metal salt solution (ZnO precursor solution), resulting in the production of particles with a narrow size distribution. The reaction was carried out at room temperature unlike in ultrasonic spray pyrolysis where the reaction is carried out in an oxygen-free environment using nitrogen as a carrier gas to avoid oxide formation and to assure reduction to metal occurs in the high temperature reaction zone. The reaction was run at a constant flow rate, automatically controlled by the pneumatic pump. The average flow rate of 5-6 ml/min. Pneumatic spray deposition was performed at the system operating temperature of 400 °C, this is because of high enough residence times spent by aerosol vapour droplets inside the heating zone.

In its final form shown here in Figure 3.1, the pneumatic spray system incorporated all of the components as well as those listed in Chapter 2 Section 2.9. The diagram in Figure 3.2 indicates the necessary steps to set-up and perform depositions of ZnO using pneumatic spray pyrolysis system employing a horizontal reactor. The aluminium substrate holder was used in most cases for thin film synthesis.

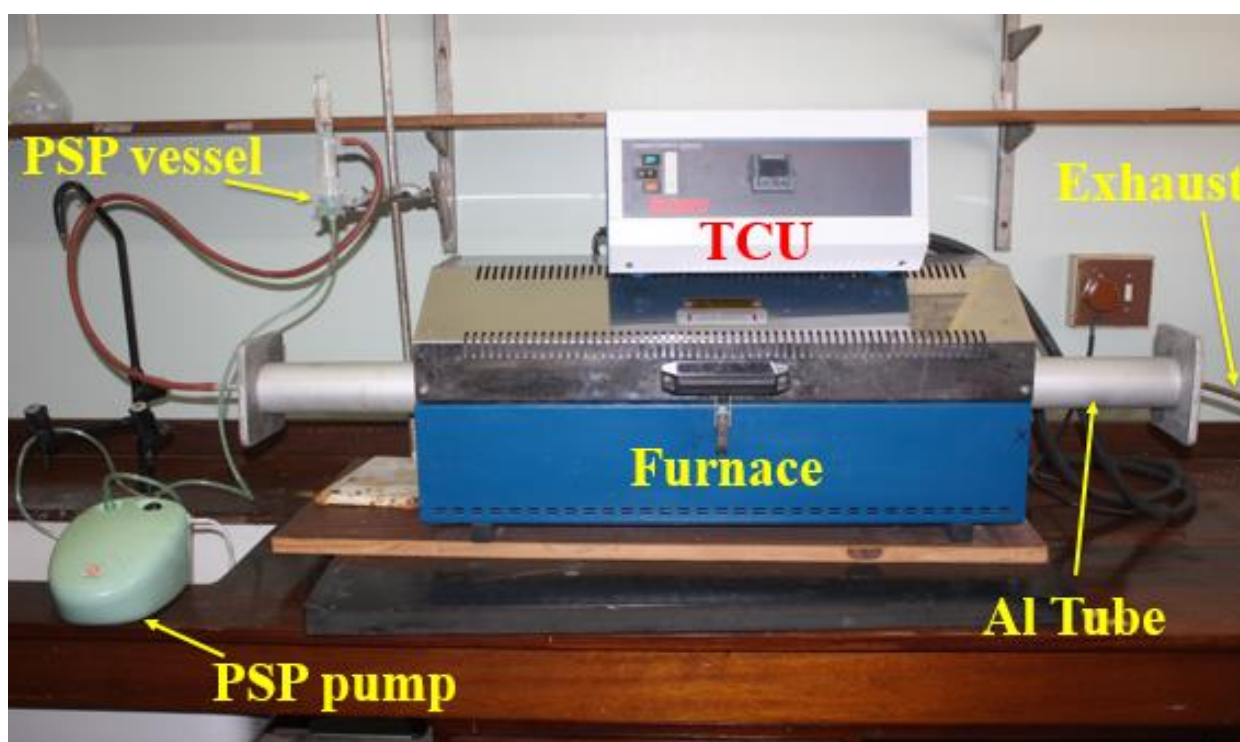


Figure 3.1: Actual photo-graph of the horizontal pneumatic spray pyrolysis system utilized in the study in its final form.

1. Prepare the desired precursor solution as outlined in table 3.1 above in a 250 ml volumetric flask

2. Transfer the precursor solution into a Pneumatic spray pyrolysis vessel. Ensure that the PSP vessel is completely closed to avoid leakage of the precursor solution.

3. Into an Aluminum tubing/quartz tubing insert the aluminum substrate holder housing the F: SnO₂ glass substrate. Set the furnace to the desired temperature. Allow it to stand for 10-15 minutes. Until the substrate has reached the furnace temperature

4. Connect the inlet of the aluminum/quartz tubing to the outlet of the Pneumatic vessel and the outlet to the (1) exhaust for thin film synthesis and/or (2) to the nano powder collection system

5. Switch on the PSP pump to the desired flow rate and then carry out spray deposition.

6. To finish pneumatic spray deposition, simultaneously switch off the furnace and the PSP pump. Anneal the sample until they are ready for collection

Figure 3.2: Shows a schematic indicating the necessary steps to set-up and perform Pneumatic spray depositions for synthesis of pure ZnO and Carbon doped ZnO

3.4. PROCEDURE

3.4.1. SYNTHESIS OF UN-DOPED ZINC OXIDE NANOPARTICLES

In typical synthesis procedure 0.1 M ZnO precursor solution was prepared by dissolving 5.4923 g of zinc acetate dihydrate [Zn (CH₃COO)₂·2H₂O] into a 250 ml volumetric flask containing minimum amount of ethanol (99.99%), Sigma Aldrich resulting in the formation of zinc ethoxide as depicted by equation (2.11) in Chapter 2 and then few drops of acetic acid (CH₃COOH) solution were added as a stabilizer, and the solution was mixed vigorously at 40 °C for 3 h to yield a clear and transparent solution. The precursor solution was then poured into a pneumatic spray pyrolysis vessel where it was blown by air from the pneumatic pump which transforms the liquid to a stream formed with uniform and fine droplets of 35 μm average diameter. The deposition was performed at a substrate temperature of 400 °C with 4 hours of deposition time.

3.4.2. SYNTHESIS OF DOPED ZINC OXIDE NANOPARTICLES

The ZnO doped precursor solution was prepared by adding 5.4927 g $\text{Zn}(\text{O}_2\text{CH}_3)_2$ to a 250 ml volumetric flask, containing minimum amount of ethanol (99.99 %), Sigma Aldrich resulting in the formation of zinc ethoxide as depicted by equation 2.12 in Chapter 2. A few drops of acetic acid (CH_3COOH) were added to the volumetric flask containing zinc ethoxide. The zinc ethoxide solution was sonicated on an ultrasonicator at 40 °C for 2 hour. 0.78 ml of tetrabutylammonium bromide (TBA) ($\text{C}_{16}\text{H}_{36}\text{BrN}$) was added to the resulting colourless solution of $\text{Zn}(\text{O}_2\text{CH}_3)_2$ in a 250 ml volumetric flask. The volumetric flask containing $\text{Zn}(\text{O}_2\text{CH}_3)_2$ and $\text{C}_{16}\text{H}_{36}\text{BrN}$ was topped up to the mark with absolute ethanol. Other precursor solutions containing different levels of the carbon dopant, $\text{C}_{16}\text{H}_{36}\text{BrN}$, were prepared in much the same way. The only difference was the volumes of the dopant solution as shown in Table 3.2.

Table 3.2: Preparation of precursor solutions.

Concentration of TBA	Volume of TBA	Millimoles of TBA
0.005 M	0.78 ml	1.26
0.010 M	1.55 ml	2.51
0.015 M	2.33 ml	3.78
0.020 M	3.10 ml	5.04
0.025 M	3.88 ml	6.30

The precursor solution was then decanted into a chamber connected to a pneumatic pump prior to spray deposition. F:SnO₂ transparent glass substrates were first washed with detergent then thoroughly rinsed with distilled water, isopropanol, distilled water and finally acetone. The glass substrates were then dried under hot air to evaporate the acetone. Deposition of un-doped and carbon doped ZnO nanoparticles was done on F:SnO₂ glass substrate at a deposition temperature of 400 °C. A flow diagram for the preparation of un-doped and C-ZnO nanoparticles is shown in Figure 3.3.

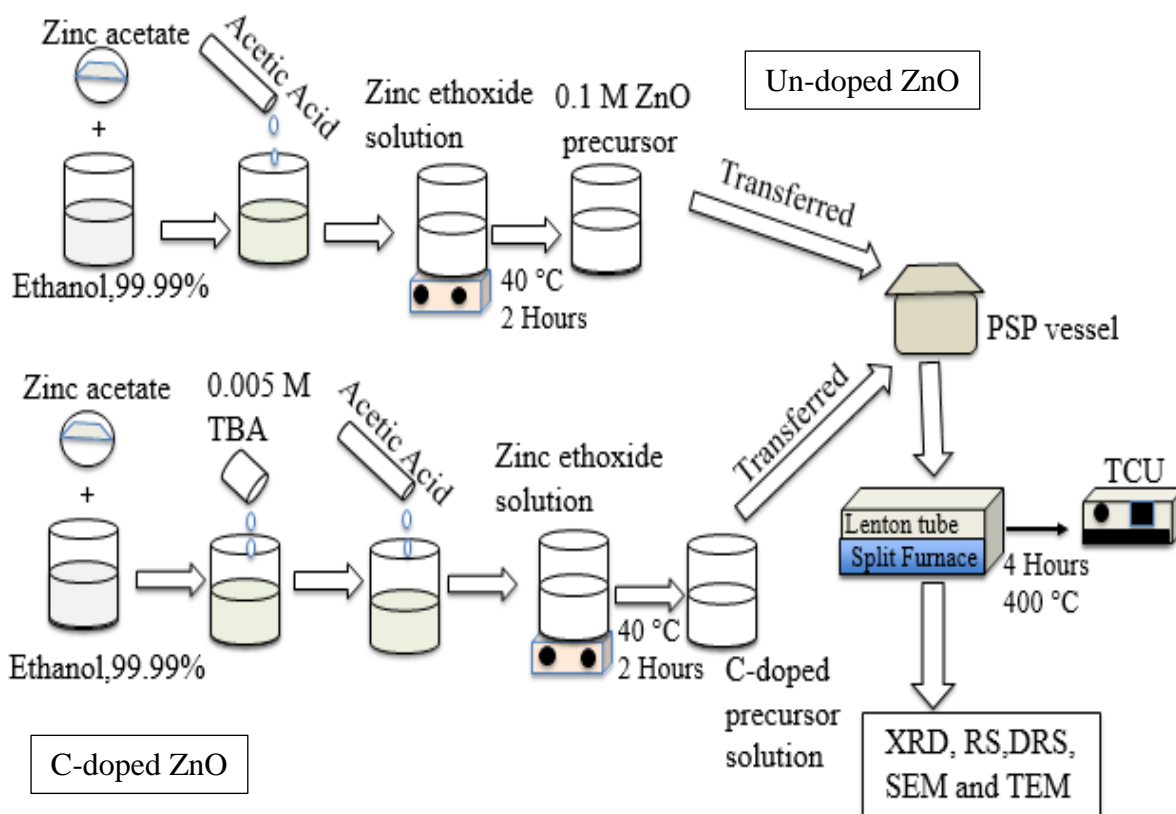


Figure 3.3: A flow diagram of the pneumatic spray pyrolysis preparation of un-doped and C-ZnO nanoparticles.

3.5. CHARACTERIZATION OF ZINC OXIDE NANOPARTICLES

3.5.1. X-RAY DIFFRACTION ANALYSIS

X-ray diffraction (XRD) is a high-tech, non-destructive analytical technique for qualitative and quantitative analysis of the crystalline structure of compounds by their diffraction pattern [1]. It is one of the most important non-destructive tools to analyse all kinds of matter ranging from fluids, to powders and crystals. A diffraction pattern is produced when a material is irradiated with a collimated beam of X-rays. The atomic planes of a crystal cause an incident beam of X-rays to interfere with one another as they leave the crystal. This technique uses X-ray (or neutron) diffraction on powder or microcrystalline samples, where ideally every possible crystalline orientation is represented equally. General X-ray diffraction phase or composition identification will distinguish the major, minor, and trace compounds present in a sample. XRD can be used to measure the average spacing between layers or rows of atoms and determine the

orientation of a single crystal or grain. It can also be used to find the crystal structure of an unknown material. The intensity of the diffracted x-rays is measured as a function of diffraction angle 2θ and the specimen's orientation. Bragg's law is used to describe the interference pattern of X-rays scattered by crystals. Furthermore, Bragg's law can also be used to describe diffraction developed in determining the structure of all states of matter with any beam, for example, ions, electrons, neutrons and protons with a wavelength similar to the distance between the atomic or molecular structure of interest. The process is presented by the equation:

$$n\lambda = 2d\sin\theta \quad (3.1)$$

where n is diffraction series, θ is diffraction angle, λ is the wavelength of X-ray, d is interplanar distance [2].

1. The distance between similar atomic planes in a mineral (the interatomic spacing) which is called the d-spacing and measured in angstroms.
2. The angle of diffraction which is called the theta angle and measured in degrees. For practical reasons the diffractometer measures an angle twice that of the theta angle. Not surprisingly, we call the measured angle 2 theta.
3. The wavelength of the incident X-radiation, symbolized by the Greek letter lambda and, in our case, equal to 1.54 angstroms.

In this study, to obtain the crystallographic phase and associated parameters of the synthesized ZnO samples, XRD spectra were obtained using a Bruker D8 Advance X-Ray diffractometer (XRD) with a Cu anode, generating $K\alpha$ radiation of wavelength 1.544 Å and operating at 40 kV and 40 mA. XRD θ - 2θ patterns of ZnO nano-powders synthesized by PSP were recorded in the 2θ range of 30° - 100° at room temperature. From XRD, the crystallite size can be calculated using Debye-Scherrer formula [3].

$$\tau = \frac{K\lambda}{\beta\cos\theta} \quad (3.2)$$

where τ is the mean particle size which is a volume average, K is a shape factor, λ the wavelength of the X-rays, β the full width at half maximum in radians, and θ the angle between the X-ray source and the detector. The value of K depend on the shape of the particles and here

the value 0.9 has been used which is a standard value for spherical particles. Figure 3.4 presents the basic principle of the XRD.

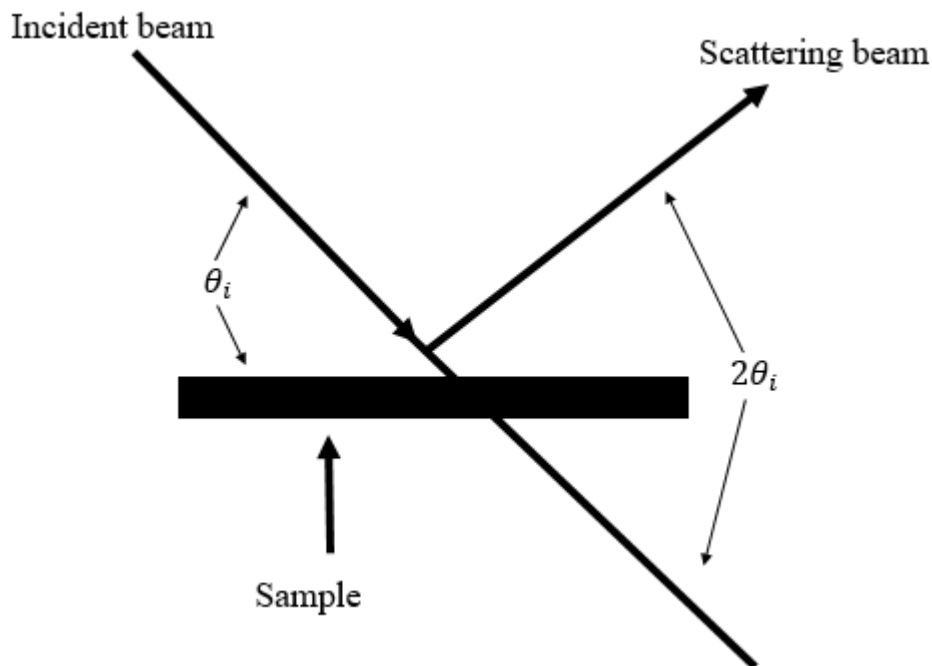


Figure 3.4: The basic principle of XRD through the Bragg's law [6].

3.5.2. SCANNING ELECTRON MICROSCOPY (SEM)

The scanning electron microscope (SEM) is a method used for high resolution imaging of the surfaces. When the specimen is irradiated with a fine electron beam (called an electron probe), secondary electrons are emitted from the specimen surface. The signals that derive from electrons sample interactions reveal information about the sample including microstructure morphology, chemical composition, crystalline structure and orientation of materials making up the sample [4]. Therefore, the image formation in the SEM is dependent on the acquisition of signals produced from the electron beam and specimen interactions. These interactions can be divided into two major categories: elastic interactions and inelastic interactions. Elastic scattering results from the deflection of the incident electron by the specimen atomic nucleus or by outer shell electrons of similar energy. Inelastic scattering occurs through a variety of interactions between the incident electrons and the electrons and atoms of the sample, and results in the primary beam electron transferring substantial energy to that atom [5,6]

The incident electron cause electrons to be radiated from the sample due to elastic and inelastic scattering actions inside the sample's surface and near-surface material. High-energy electrons that are ejected by an elastic collision of an incident electron, normally with a sample atom's nucleus are referred to as backscattered electrons. The energy of backscattered electrons are equivalent to that of the incident electrons [4, 6, 8]. Emitted lower-energy electrons resulting from inelastic scattering are called secondary electrons. Secondary electrons can be formed by collisions with the nucleus where substantial energy loss occurs or by the expulsion of loosely bound electrons from the sample atoms. The energy of secondary electrons is typically 50 eV or less [6-8]. In most applications, data are collected over a selected area of the surface of the sample and a 2-dimensional image is generated that displays spatial variations in these properties. The advantage of SEM over light microscopy is contain much higher magnification ranging from 20X to approximately 30,000X, and greater depth of field up to 100 times that of light microscopy.

The SEM is capable of performing analyses of selected point locations on the sample, this technique is especially useful in qualitative and quantitative chemical analysis information is also obtained using an energy dispersive x-ray spectrometer (EDS). SEM uses a focused electron probe to extract structural and chemical information point-by-point from a region of interest in the sample [8]. The high spatial resolution of an SEM makes it a powerful tool to characterise a wide range of specimens at the nanometre to micrometre scales. In this study, Field Emission Scanning Electron Microscope (FE-SEM) Zeiss Auriga SEM equipped with EDS with Smart SEM software was used to study the elemental, structural and morphological properties of ZnO nanostructures at an accelerating voltage of 30 KV. Gold coating was used in order to avoid sample charging effects during the scanning electron microscopy (SEM) analysis [7, 8]. Figure 3.5 shows the schematic diagram of the SEM.

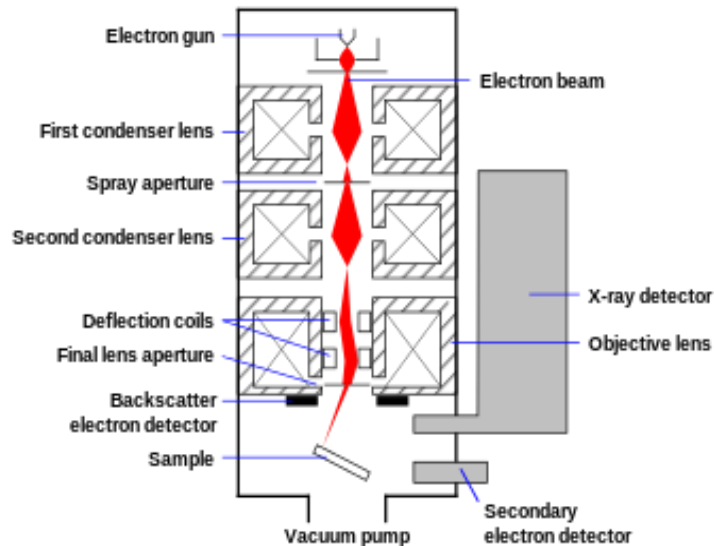


Figure 3.5: The schematic diagram of SEM [7]

3.5.3. ENERGY DISPERSIVE X-RAY SPECTROSCOPY (EDS OR EDX)

Energy dispersive X-ray spectroscopy (EDS or EDX) is an analytical technique used for the elemental analysis or chemical characterization of a sample [9]. It is used to provide qualitative information about the sample. This technique depends on the investigation of a sample through interactions between electromagnetic radiation and matter, analysing X-rays emitted by the matter in response to being hit with charged particles. Its characterization abilities are due in large part to the fundamental principle that every element has a unique atomic structure allowing X-rays that are characteristic of an element's atomic structure to be recognized uniquely from each other [6, 9]. A high energy beam of charged particles such as electrons or protons or a beam of X-rays is focused into the sample being investigated in order to stimulate the emission of characteristic X-ray from a specimen. At rest, an atom inside the sample contains ground state electrons in discrete energy levels or electron shells bound to the nucleus [9]. The incident beam may excite an electron in an inner shell, ejecting it from the shell while making an electron hole where the electron was. An electron from an outer, higher energy shell then fills the hole and the difference in energy between the higher-energy shell and the lower energy shell might be released or discharged. The number and energy of the X-rays emitted from a specimen can be measured by an energy dispersive spectrometer. As the energy of the X-rays are characteristic of the difference in energy between the two shells, and the atomic

structure of the element from which they were emitted, this allows the elemental composition of the specimen to be measured [6].

This technique uses the characteristic spectrum of x-rays emitted by the specimen after excitation by high-energy electrons to find information about the elemental composition of a sample. In this study, the EDX of the ZnO samples was done by the Field Emission Scanning Electron Microscope (FE-SEM) Zeiss Auriga SEM machine. The EDX has shown that both zinc (Zn) and oxygen (O) are present in the sample being investigated. The graph shows the presence of C and Al. C was due to the carbon double sided tape over which the sample was held to do the SEM characterization and Al occurred due to the aluminium tube that was used in our PSP system. Figure 3.6 shows the EDX of the un-doped ZnO sample.

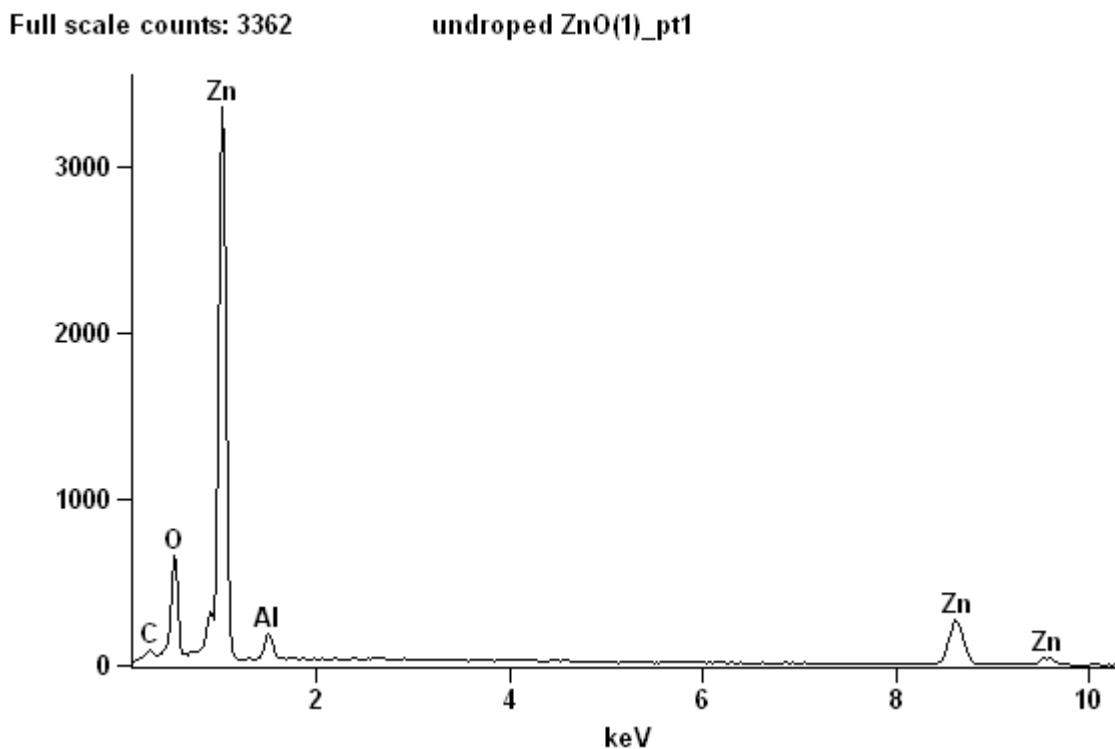


Figure 3.6: *The EDX of the synthesized un-doped ZnO sample*

3.5.4. HIGH RESOLUTION TRANSMISSION ELECTRON MICROSCOPE (HRTEM)

High-resolution transmission electron microscopy (HRTEM) is an imaging technique whereby a beam of electrons is transmitted through a specimen, and then an image is formed. The image is then magnified and focused onto an imaging device, such as a fluorescent screen, on a layer

of photographic film, where the final image is observed [10]. This system can study small details in the cell or different materials down to near atomic levels. HRTEM can examine the size, shape and arrangement of the particles which make up the specimen and their relationship to each other on the scale of atomic diameters. The materials to be measured with this method need to have dimensions small enough to be electron transparent and that can be formed by the deposition of a dilute sample containing the specimen onto support grids [6,10]. The suspension is typically a volatile solvent, for example, ethanol, ensuring that the solvent quickly evaporates allowing a sample that can be rapidly analyzed. The possibility for high magnification has made the HRTEM a valuable instrument in medicinal, organic and material sciences research.

The specimens must be very thin and ready to withstand the high vacuum present inside the device in all cases. For organic or biological specimens the maximum specimen thickness is around 1 micrometer. Biological specimens are held at liquid nitrogen temperatures in order to withstand the instrument vacuum [11, 13]. In materials science, the specimens tend to be naturally resistant to vacuum and need to be prepared as a thin foil, or carved so that some part of the specimen is thin enough for the beam to penetrate. This technique can also be used for determination of the electron diffraction patterns of the crystalline structures. A crystalline material connects with the electron beam normally by diffraction instead of absorption or retention. The intensity of the transmitted beam is influenced by the volume and density of the material through which it passes.

The intensity of the diffraction relies upon the orientation of the planes of atoms in a crystal relative to electron beam [6, 11, 14]. At specific points the electron beam is diffracted strongly from the axis of the incoming beam, while at other angles the beam is largely transmitted. TEMs are capable of imaging at a significantly higher resolution than light microscopes and can give higher resolution images of the inner structure of the sample contrasted with the SEM. In this study, the transmission electron microscopy bright field (TEM) and high resolution images (HRTEM) coupled with selected area electron diffraction (SAED) performed on a JEOL- JEM 2100 from CSIR was used to determine structure, lattice parameters and particle morphology of the C:ZnO NPs. The HRTEM was also equipped with the energy dispersive x-ray spectroscopy (EDXS) accessory setup using a Thermo Fisher Scientific detector cooled at liquid nitrogen temperature. Figure 3.7 shows the schematic diagram of a TEM.

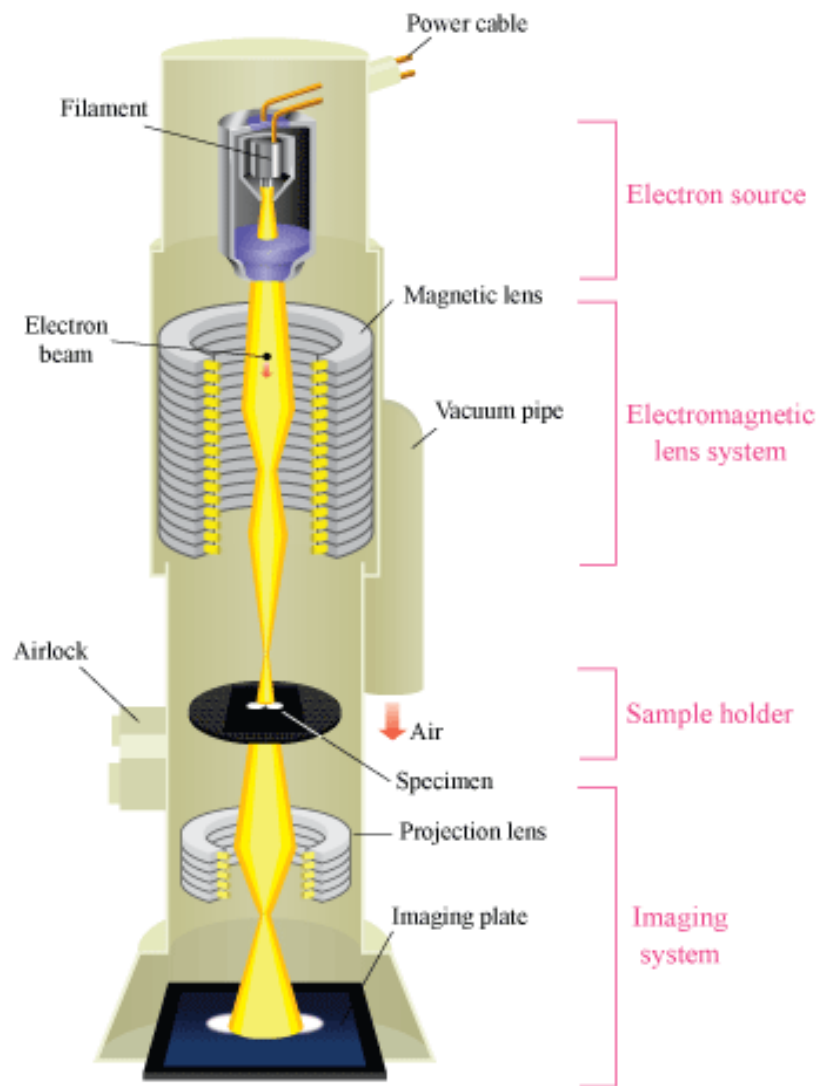


Figure 3.7: Schematic diagram of a TEM [12]

3.5.5. RAMAN SPECTROSCOPY (RS)

Raman spectroscopy is a non-destructive technique commonly used for optical investigation, in most cases for chemical analysis or in solid state physics. This is a powerful technique to analyse materials microstructures in semiconductors [15]. It is usually used for the characterization of semiconductor systems. However, in most of the experiments, the studied elementary excitations are phonons [16]. In solids, the vibrations which are quantum of energies caused by the collective vibrations of the atoms in lattice are usually called phonons, and they have a large impact on properties like transport of heat, electricity and sound [15, 17].

This technique is specified to analyse material crystallinity because it can be done at room temperature, in air, without physical interaction and is thereby considered a non-destructive technique [15].

Raman spectroscopy is based on inelastic scattering of monochromatic light, usually from a laser source. Inelastic scattering means that the frequency of photons in monochromatic light changes upon interaction with a sample. Photons of the laser light are absorbed by the sample and then reemitted. It measures the vibrational motion of a molecule like infrared spectroscopy. The physical method of observing the vibrations are however different from the infrared spectroscopy. Raman is a light scattering technique, so all that is required for the collection of a spectrum is to place the sample into the excitation beam and collect the scattered light. There is no need for high-vacuum or desiccated sample holders since there are few concerns with sample thickness and little interference from the ambient atmosphere [15]

In this study, Raman spectroscopy is used to examine the vibrations, if any, in Raman active vibrational modes of ZnO nanoparticles. Raman scattering is sensitive to crystal symmetry and disorders in micro and nano-crystalline structures due to defects or impurities [18]. Scattering occurs when a monochromatic light beam passes through a crystal or solid involving Rayleigh scattering and Raman scattering. The Rayleigh scattering occurs if there is an elastic collision between the incident photons with the phonons in the material, and generates the light with the same vibration frequency while Raman scattering occurs when there is an inelastic collision between the incident photons with the phonons of the material [15, 16, 17].

In a typical spectrum, the intensity (a.u) is plotted against the Raman shift (cm^{-1}), which is a function of photons population of a certain frequency reaching the detector. Likewise, the Raman shift is given by the frequency difference between the scattered light and the monochromatic excitation source. Generally, the Raman shift is designated positive (Stokes Raman scattering) in the case whereby the inelastic light scattering generates an elementary excitation and the scattered light hence exhibiting a lower frequency. The wavenumber value becomes negative (anti-Stokes Raman scattering) in the case of an annihilated elementary excitation. The measurements taken in this study were at room temperature, to reduce the thermally excited phonons resulting in an important Stokes process. In the current study, the Raman spectra of the ZnO samples was done using a Confocal RAMAN Imaging system (WITec GmbH, Ulm, Germany) alpha300RS. A fiber coupled DPSS laser 532 nm with

maximum output power after single mode fiber coupling of 44 mW was used as the excitation source. Data was then collected using a multimode fiber into a high throughput lens based spectrograph (UHTS 300) with 300 mm focal length and two gratings 600 g/mm & 1800 g/mm, both blazed at 550 nm. The UHTS 300 spectrograph is connected with a peltier cooled back illuminated CCD camera with better than 90% QE in the visible excitation. Each spectrum was acquired at an integration time of 1.09667s and about 200 accumulations were collected per each spectrum in the scan range 100-1100 cm^{-1} . Figure 3.8 presents a typical schematic of a Raman spectrometer.

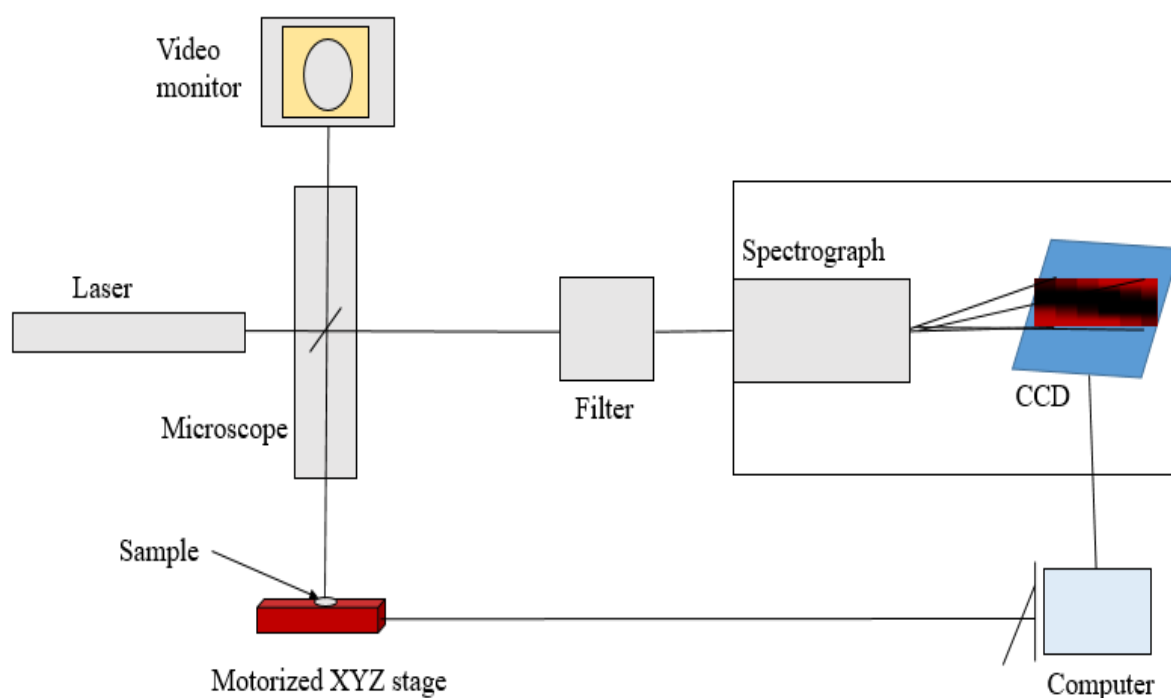


Figure 3.8: Typical schematic of a Raman spectrometer [6].

3.5.6. ULTRAVIOLET VISIBLE SPECTROSCOPY (UV-VIS)

Ultraviolet-visible spectroscopy (UV-Vis) is an analytical technique that is widely employed for the quantitative analysis of a variety of analytes [19]. The UV-Vis spectra of ions and molecules are associated with the transitions between electronic energy levels of certain types or functional groups of molecules and do not characterize the entire molecule. The energies involved in these transitions are in the range of 30 to several hundred kcal/mole. The UV-Vis spectra are usually measured in very dilute solutions and the most important criterion in the

choice of solvent is that the solvent must be transparent within the wavelength range being observed [19].

The optical properties of ZnO samples were evaluated in terms of UV-Vis absorption spectra (Varian Cary 50 UV-Vis spectrophotometer) at room temperature. UV-Vis requires shooting a focused, monochromatic beam of light through a sample and recording how much of the light is transmitted via a light sensitive detector. A beam of light from a visible and/or UV light source is separated into its component wavelengths by a prism or diffraction grating. Each monochromatic (single wavelength) beam in turn is split into two equal intensity beams by a half-mirrored device. One beam, the sample beam (colored magenta), passes through a small transparent container (cuvette) containing a solution of the compound being studied in a transparent solvent. The sample may be suspended in solution, pressed into a solid disc, or a thin film on a transparent substrate [19].

In this study, the technique was used to characterize the intensity of light passing through a sample in the ultraviolet and visible regions in terms of wavelength expressed in nanometers. It is almost completely used for quantitative analysis, that is, the estimation of the amount of a compound known to be present in the sample [6, 19]. The procedures concerned in absorption spectrometry are absorption and transmission based on the Beer Lambert's Law which expresses that every layer of equivalent thickness of an absorbing medium absorbs an equal fraction of the radiant energy that traverses it [19]. If the intensity of the incident radiation is I_o and that of the transmitted light is I , then the fraction transmitted is:

$$I/I_o = T \quad (3.3)$$

The percentage transmission is:

$$\%T = I/I_o \times 100 \quad (3.4)$$

The absorbance:

$$\begin{aligned} A &= \log_{10}(I/I_o) \\ &= \log_{10}\left(\frac{100}{T}\right) \end{aligned}$$

$$A = \epsilon cL$$

where L expressed in m is the length of the radiation path through the sample, c expressed in per molar is the concentration of absorbing molecules in that path and ϵ expressed in per mol meter squared is the molar extinction coefficient. In this study, the Lamda 750S UV-VIS spectrophotometer, from the CSIR-NCNSM was used to study the absorption properties of the ZnO samples synthesized by pneumatic spray pyrolysis technique. Figure 3.9 shows the schematic diagram of a double-beam UV-VIS spectrophotometer.

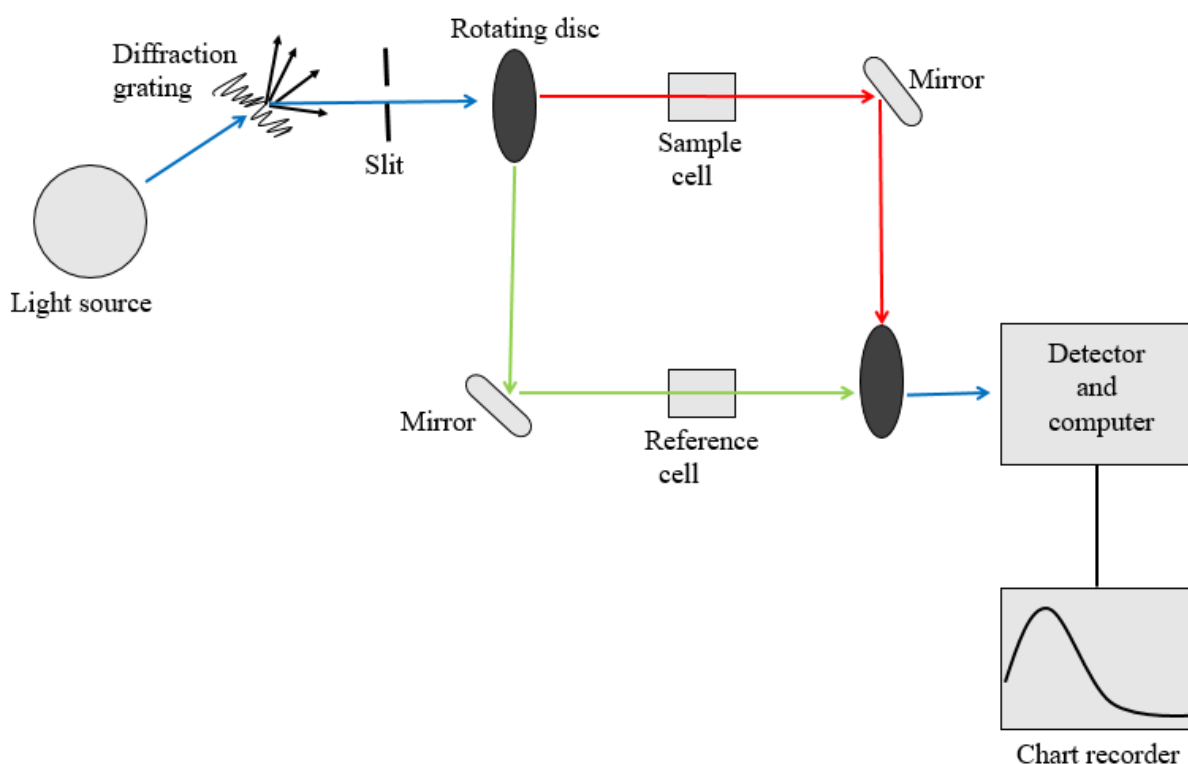


Figure 3.9 Double-beam UV-Vis absorption spectrophotometer [6]

3.5.7. DIFFUSE REFLECTANCE SPECTROSCOPY (DRS)

The UV-Vis diffuse reflectance spectroscopy is one of the most commonly used optical methods for explaining the electronic behaviour present in the structure of a solid material. The spectra obtained give information about the electronic transitions of the different orbitals of the solid sample [20]. It involves shooting a focused monochromatic beam of light through a

sample and recording how much of the light is passed through a light sensitive detector. The sample can be suspended in solution, pressed into a disc or a thin film on a transparent substrate.

In this study, the diffuse reflectance (DRS) measurements were carried out with a double beam Lambda 35 Perkin-Elmer UV-Vis spectrometer equipped with an integrated sphere accessory. Diffuse reflectance spectroscopy was used to determine the shift in the optical absorption band of the synthesized un-doped and carbon doped ZnO nanoparticles. The samples were analysed at room temperature in the wavelength range of 100 to 1500 nm. Figure 3.10 shows the layout of a standard spectrometer for analyses of electromagnetic radiation in the UV-Visible –IR regions.

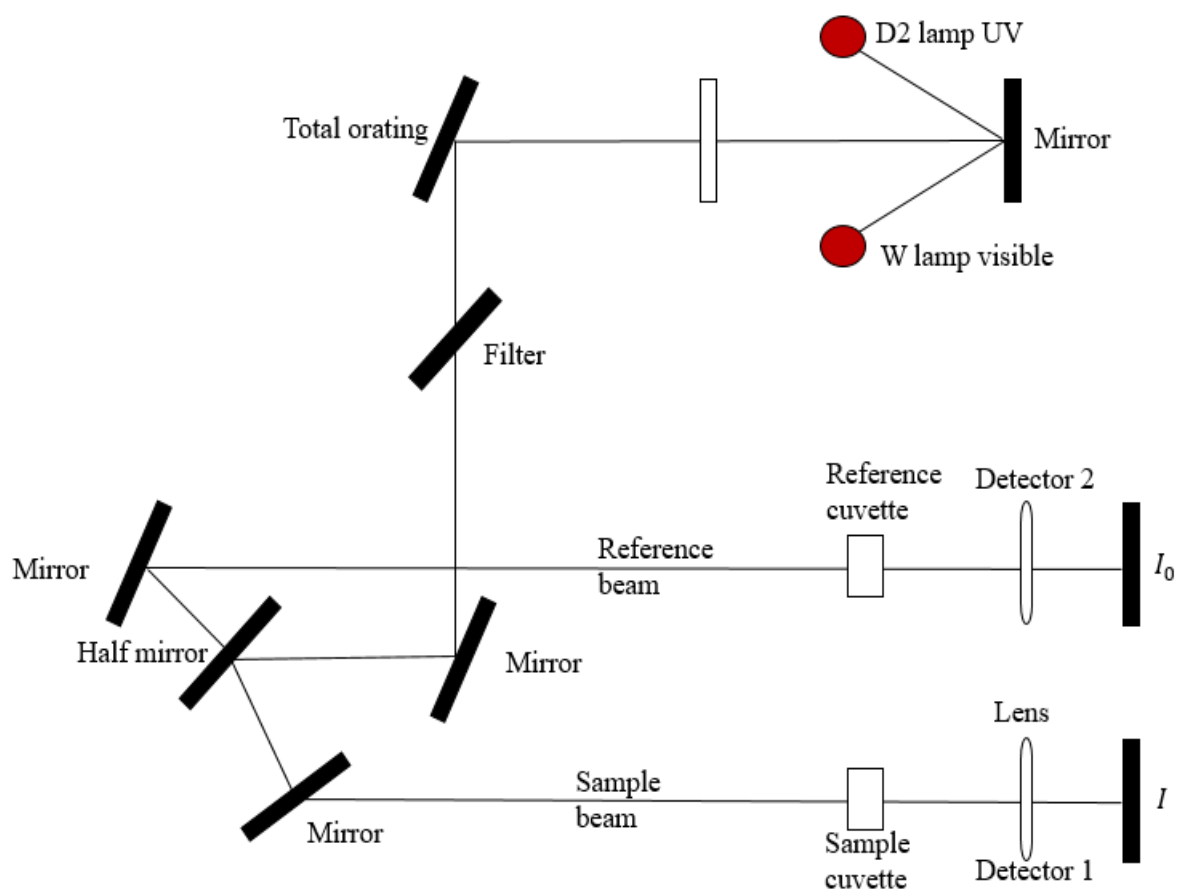


Figure 3.10: A layout of a standard spectrometer for analyses of electromagnetic radiation in the UV-Visible –IR regions [6. 19].

3.6. CONCLUSION

The chapter has provided a detailed report on the synthesis of zinc oxide (ZnO) nanoparticles by pneumatic spray pyrolysis (PSP) technique. The reagents and raw materials used in this research were specified into detail. Moreover, the chapter has offered a clear presentation of the experimental procedure used for the synthesis of un-doped and C-ZnO nanoparticles. Lastly, the analytical techniques that were used for characterization of the synthesized ZnO samples are well presented in this chapter.

3.7. REFERENCES

1. G. Cao , Nanostructures and nanomaterials: Synthesis, properties & applications, 6th edition, London, (2004) 1-5.
2. T. L. Tan, C.W. Lai, S.B.A. Hamid, Tunable band gap energy of Mn-doped ZnO nanoparticles using the coprecipitation technique, *J. Nano.* 2014 (2014) 1-6.
3. E. Zaleta-Alejandre, J. Camargo-Martinez, A. Ramirez-Garibo, M. L. Pérez-Arrieta, R. Balderas-Xicohténcatl, Z. Rivera-Alvarez, C. Falcony, Structural, electrical and optical properties of indium chloride doped ZnO films synthesized by ultrasonic spray pyrolysis technique. *Thin Sol. Film.* 524 (2012), 44–49.
4. J. K. Behera, synthesis and characterization of ZnO nano-particles, 2009, [MSc thesis], National Institute of Technology, Rourkela-769008, Orissa, India.
5. S. Charurvedi, P. N. Dave, Microscopy in Nanotechnology, Current microscopy contributions to Adv. Sci. Technol. In: Mendez-Vilas A (ed) (2012) 946 -952.
6. G. L. Kabongo, Luminescence investigation of zinc oxide nanoparticles doped with rare earth ions, 2013, [MSc thesis], University of South Africa.
7. Handbook of analytical methods for materials, http://www.cientificosaficionados.com/microscopio/MICROSCOPIO%20ELECTRONICO_archivos/hamm72d.pdf , [Accessed, 7 November 2016].
8. W. Zhou, R. P. Apkarian, Z. L. Wang, Fundamentals of scanning electron microscopy. scanning microscopy for nanotechnology, *J. Chem. Phys. C.7* (2007) 1–40.
9. A. R. Ocwelwang, photocatalytic activity and antibacterial properties of Ag/N-doped TiO₂ nanoparticles on PVAE-CS nanofiber support, 2012, [MSc thesis], University of Fort Hare.
10. Z. L. Wang, Y. Liu, Z. Zhang, handbook of nanophase and nanostructured materials, 4th edition, New York, (2003).
11. TransmissionElectronMicroscopy:http://en.wikipedia.org/wiki/Transmission_Electron_Microscopy, [Accessed, 9 November 2016] .
12. BasicprincipleofTransmissionElectronMicroscope:http://www.hkphy.org/atomic_world/tem/tem02_e.html, [Accessed, 9 November 2016].
13. G. D. Guthrie, D.R. Veblen, High resolution transmission electron microscopy of mixed layer illite /smectite: computer simulations. *Clays and clay minerals.* 37 (1989), 1–11.
14. D. Tyutyunnikov, High resolution transmission electron microscopy investigations of Fe Pt and Au nanoparticles, 2010, [Diploma thesis], University of Duisburg-Essen.

15. I. A. S Carvalho, R. L. Ribeiro, A. L. P. Faria, E. P. Muniz, J. R. T. Branco, Raman spectroscopy mapping of plasma thermally sprayed silicon sheet for solar cell substrate, *J. Mater. Sci. Eng.* 5 (2011) 561–569.
16. M. Schumm, ZnO-based semiconductors studied by Raman spectroscopy: semimagnetic alloying, doping, and nanostructures, 2008, [PhD Thesis], Julius– Maximilians– Universitat Wurzburg, Germany.
17. T. J. Jacobsson, Synthesis and characterisation of ZnO an experimental investigation of some of their size dependent quantum effects, *Mater. Chem.* (2009) 1–73.
18. R. Kumari, A. Sahai, N. Goswami, Effect of nitrogen doping on structural and optical properties of ZnO nanoparticles. *Progress in natural science: Mater. Int.* 25(2015), 300–309.
19. Basic UV-Vis Theory, Concepts and Applications.
20. T. M. L. Goeme, M. A. A. Lemus, V. A. Morales, E. G. Lopez, P, C. Ocampo, Study of bacterial sensitivity to Ag-TiO₂ nanoparticles, *J. Nanomed.Nanotechnol.* (2012), 1-7.

CHAPTER 4

RESULTS AND DISCUSSION

4.1. INTRODUCTION

This chapter presents and discusses in detail the experimental findings of the zinc oxide nanoparticles (NPs) synthesised by pneumatic spray pyrolysis (PSP) technique. The chapter begins by presenting the structural properties of the ZnO particles determined through XRD analysis to elucidate more on the crystalline structure of un-doped and carbon doped ZnO (C-ZnO) NPs. The morphological properties were determined through SEM to reveal the effect of carbon modification on the surface of the ZnO NPs. HRTEM has been used to reveal the effect of carbon doping on the structural, NPs size and lattice properties of ZnO NPs. Furthermore the chapter discuss the optical Raman modes present in the synthesized ZnO samples using Raman spectroscopy. Additionally, the Raman spectroscopy peak shifts of the E_2 high mode, $A_1(\text{LO})$ mode and multi-phonon due to the effect of carbon doping were also examined. Finally this chapter closes by determining whether there are any changes in the reflectance of the carbon doped ZnO nanoparticles as dopant level increases.

4.2. STRUCTURAL CHARACTERIZATION

4.2.1. X-RAY DIFFRACTION ANALYSIS

The size of small particles can be estimated by using the peak broadening of the peaks in the XRD pattern. This has been done according to the method of Scherrer [1], which is considered as a standard method. The mean particle size, τ , which is a volume average, is given by Equation 4.1 where K is a shape factor, λ the wavelength of the X-rays, β the full width at half maximum in radians and θ the angle between the X-ray source and the detector. The value of K depends on the shape of the particles and in this work the value 0.9 has been used which is a standard value for spherical particles [2]

$$\tau = \frac{K\lambda}{\beta \cos \theta} \quad (4.1)$$

The calculated particles size for the un-doped, 0.005 M, 0.01 M, 0.015 M, 0.02 M and 0.025 M are presented in Table 4.1. The XRD analysis has revealed that the size of the NPs increases with dopant concentration as highlighted in Table 1.

Table 4.1: Position of the main diffraction peaks and average crystallite size calculated from XRD patterns of the fabricated ZnO nanoparticles.

Sample #	ZnO(100) peak position (°)	ZnO(002) peak position (°)	ZnO(101) peak position (°)	XRD (100) crystallite Size (nm)	XRD (002) crystallite Size (nm)	XRD (101) crystallite Size (nm)
Un-doped	31.90	34.43	36.34	11.30	12.50	9.60
0.005 M C-ZnO	31.98	34.53	36.42	16.56	17.38	16.28
0.01 M C-ZnO	31.81	34.43	36.25	10.69	13.68	9.99
0.015 M C-ZnO	31.98	34.43	36.25	10.70	12.40	9.96
0.02 M C-ZnO	31.82	34.53	36.25	10.84	12.63	9.98
0.025 M C-ZnO	31.99	34.43	36.34	11.42	14.63	10.22

The X-ray Diffraction patterns of the un-doped and C-ZnO NPs are presented in Figure 4.1. XRD patterns of the as PSP synthesized ZnO NPs were recorded in the 2θ range of $30-80^\circ$ at room temperature. The NPs were deposited at substrate temperature of 400°C and annealed for 1 hour in the split tube furnace at the same temperature. The XRD analysis of the synthesized un-doped NPs has revealed the peaks at 31.90° , 34.43° , 36.34° , 47.73° , 56.88° , 63.04° , 68.20° , and 77.33° . The XRD peaks are indexed (100), (002), (101), (102), (110), (103), (200), and (112) respectively, belonging to the hexagonal Wurtzite structure of ZnO. All these peaks can be indexed to ZnO structure and peaks with miller indices given belong to the standard ones from the JPDFS card no: 36-1451 [3, 4,]. Moreover, the presence of these peaks in the carbon doped Zinc oxide (C-ZnO) samples confirms that the as synthesized C-ZnO NPs

have the hexagonal Wurtzite structure. Furthermore, the XRD diffractograms have revealed a sharp and intense peak for the dominant peak at 36.34° indexed (101) which reveals the samples are highly crystalline as shown in Figure 4.1. In addition the XRD diffractograms of the C-ZnO NPs has revealed additional peaks at 2θ positions of (72.72°) and (77.15°) indexed (004) and (202) respectively which were due to the incorporation of carbon in the ZnO matrix. Moreover the 0.005 TBA C-ZnO sample has also revealed the existence of the peaks indexed (200) and (201) which are possible due to other impurities in the sample [3]. The presence of the dominant peaks at 2θ positions of 31.90° , 34.43° and 36.34° indexed (100), (002) and (101) respectively, has confirmed the existence of Wurtzite ZnO structure in both the un-doped and C-ZnO samples. Furthermore, a dominant diffraction peak at 36.34° indexed (101) with high intensity was revealed by XRD analysis of both un-doped and C-ZnO PSP fabricated samples, a high intensity peak at this position indicates that the ZnO NPs have preferential **a**-axis orientation perpendicular to the crystallographic plane (101) and it is similar to the one observed by Rekha *et al* 2010, where they reported that the high intensity of (101) peak suggests that the growth of nanoparticles has taken place along the easy direction of crystallization of ZnO [3]. Figure 4.1 shows the X-ray diffraction patterns of the synthesized ZnO nanoparticles by PSP technique.

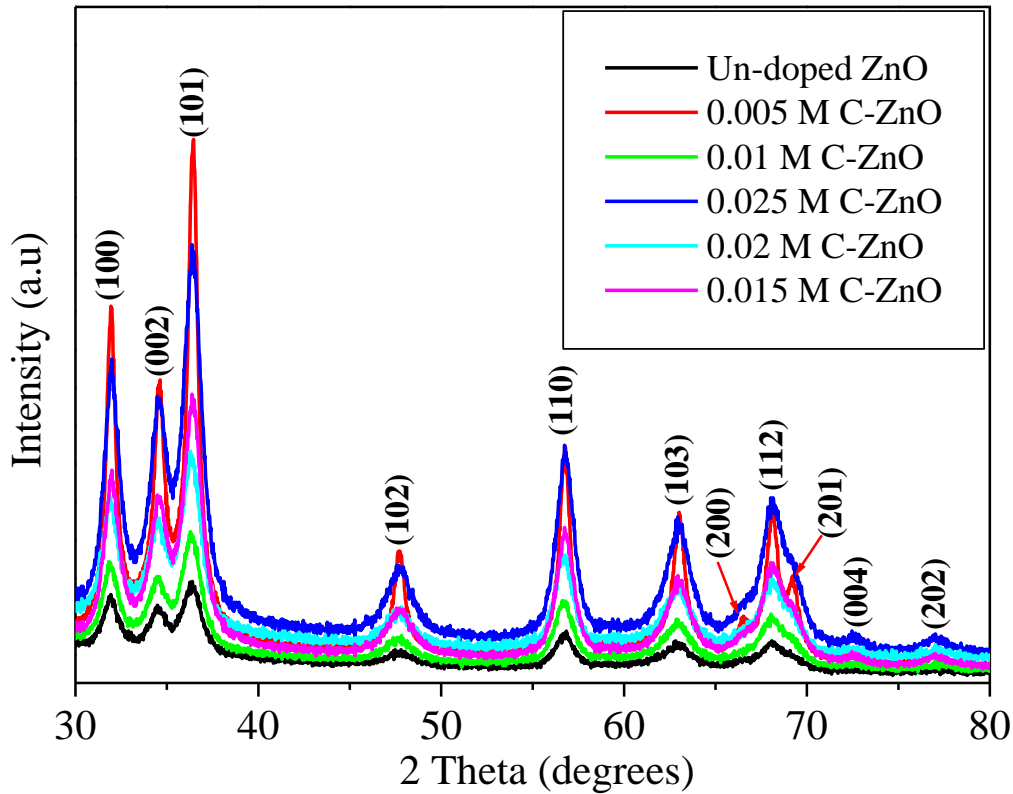


Figure 4.1: XRD patterns of ZnO nanoparticle deposited by a PSP technique.

It is well established that the lattice distortion due to defects may cause shift in the XRD peaks positions depending on the type of strain in the crystal structure. Tensile or compressive strain causes the XRD peak positions to shift either to higher or lower angle [5]. Since the atomic radii of C $r = 0.77 \text{ \AA}$ is bigger than that of O $r = 0.65 \text{ \AA}$, C substitution in ZnO lattice results in tensile strain along with increase of crystallite size. The XRD diffractograms have revealed peak positions of 31.90° , 34.43° , 36.34° un-doped; 31.98° , 34.53° , 36.42° 0.005 M C-ZnO; 31.81° , 34.43° , 36.25° 0.01 C-ZnO; 31.98° , 34.43° , 36.42° 0.015 M C-ZnO; 31.82° , 34.53° , 36.25° 0.02 M C-ZnO; 31.99° , 34.43° , 36.34° 0.025 M C-ZnO. The calculated NPs sizes from Equation 4.1 are 11.30, 12.50, 9.60 nm un-doped; 16.56, 17.38, 16.28 nm 0.005 M C-ZnO; 10.69, 13.68, 9.99 nm 0.01 M C-ZnO; 10.70, 12.40, 9.96 nm 0.015 M C-ZnO; 10.84, 12.63, 9.98 nm 0.02 M C-ZnO; 11.42, 14.03, 10.22 nm 0.025 M C-ZnO. Our analysis has confirmed

peak shift in 2θ angles as shown in Figure 4.2. This observation is in agreement with the calculated crystallite sizes from Equation 4.1 which increase as the amount of C dopant increases as shown in Table 4.1. This is a clear indication of the incorporation of C into ZnO lattice. Thus we can conclude that similarly like N doping [5, 6], C doping into ZnO lattice can be observed through peak broadening and shift of the most prominent peak (101) of the XRD diffractograms of ZnO. Since peak broadening reflects alteration of crystallite size. Figure 4.2 shows the XRD peaks positions for the (100), (002) and (001) planes as a function of C content in the synthesized ZnO NPs

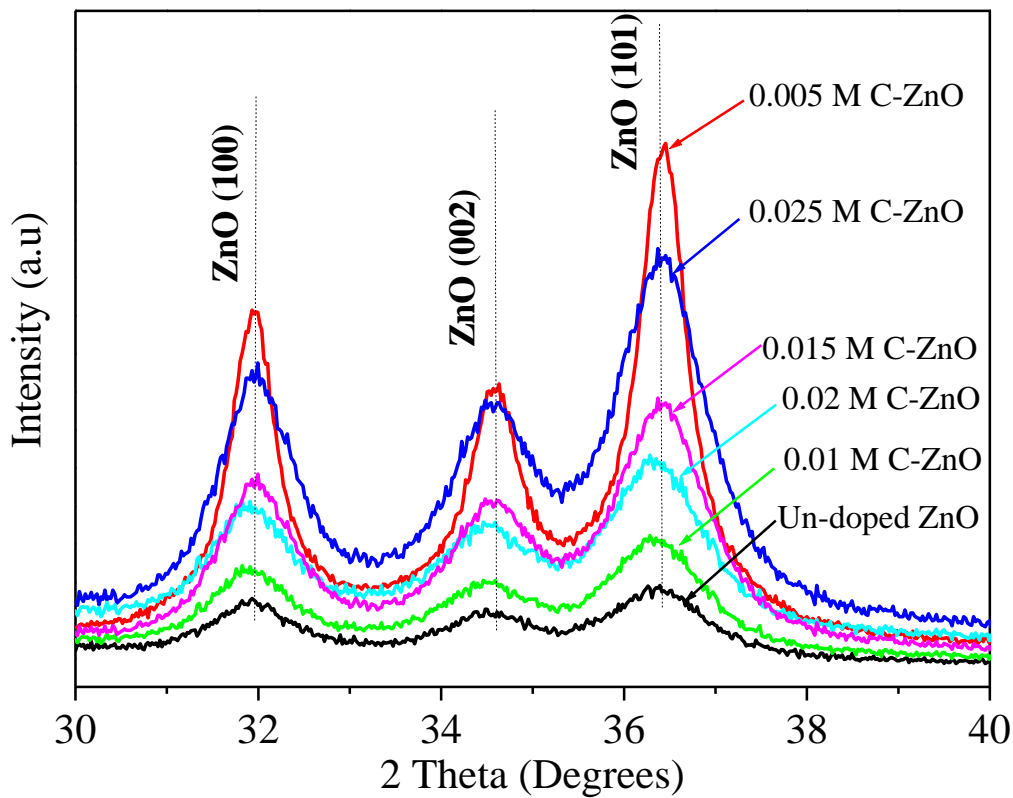


Figure 4.2: XRD peaks positions for the (100), (002) and (001) planes as a function of C content in ZnO NPs synthesized by PSP technique

The incorporation of C species into ZnO lattice and the effect of C doping on the ZnO crystal structure have been cross examined by monitoring the peak positions of the (100), (002) and

(001) planes as shown here in Figure 4. 2. Previous studies on the incorporation of Ag species [7] N [8] in ZnO lattice and C in TiO₂ [11] lattice have revealed that interstitial doping results in peak shift to lower 2θ values, whereas substitutional doping results of either N and C in ZnO lattice results in peaks shifts to higher 2θ values [8, 9 ,11]. The three main peak positions of C-ZnO NPs shown in Figure 4.2 reveal that carbon doping results in a peak shift to higher 2θ values which indicates substitutional doping in ZnO samples. This confirms the results from the calculated crystallite size of the dominant diffraction plane (101) which indicates an increase in crystallite size with increase in carbon doping. The calculation of ZnO NP size by Scherrer equation have revealed that the as synthesized un-doped ZnO NPs, doped 0.005 TBA, 0.01 TBA, 0.015 TBA, 0.02 TBA and 0.025 TBA ZnO NPs have a particle size range of (9.60-12.50 nm); (16.28-17.38 nm); (9.99-13.68 nm); (9.96-12.40 nm); (9.98-12.63 nm) and (10.22-14.63 nm), respectively. Therefore we can conclude that an increase in concentration of the carbon dopant (TBA) has resulted in a correlative increase in ZnO NPs.

The interplaner distance d for the pure and C doped ZnO were calculated by the relation:

$$n\lambda = 2d\sin\theta \quad (4.2)$$

Where n is an interger, λ is the wavelength of the X-rays, d is the distance between crystal planes and θ is the angle between the incident ray and scattering planes [13]. The calculated d values from equation 4.2 revealed that the synthesized ZnO NPs with d spacing (miller indices) of 2.80 (100), 2.61 (002), 2.47 (101) (un-doped); 2.80 (100), 2.60 (002), 2.47 (101) (0.005 M C-ZnO); 2.82 (100), 2.61 (002), 2.48 (101) (0.01 M C-ZnO); 2.61 (002), 2.48 (101) (0.015 M C-ZnO); 2.81 (100) 2.60 (002), 2.48 (101) (0.02 M C-ZnO); 2.80 (100), 2.61 (002), 2.50 (101) (0.025 M C-ZnO); which is in close agreement with literature of the hexagonal Wurtzite ZnO from the JPDS card no: 36-1451 [3,4] with d spacing of 2.81 (100), 2.60 (002) and 2.48 (101), this confirms that the as synthesized ZnO has hexagonal Wurtzite structure [5, 14]. Table 4.2 here shows the calculated interplaner distance d with their 2θ values compared to those found in literature from JPDS card no: 36-1451.

Table 4.2: The calculated interplanar d spacing of un-doped and C-doped compared to those from JPDS.

Sample #	Miller indices (hkl)	2 θ (in degrees)		Interplaner distance (d) (Å)	
		Observed	JCPDS	Observed	JCPDS
Un-doped	(100)	31.90	31.77	2.80	2.81
	(002)	34.43	34.42	2.61	2.60
	(101)	36.34	36.25	2.47	2.48
0.005 M C-ZnO	(100)	31.98	31.77	2.80	2.81
	(002)	34.53	34.42	2.60	2.60
	(101)	36.42	36.25	2.47	2.48
0.01 M C-ZnO	(100)	31.81	31.77	2.82	2.81
	(002)	34.43	34.42	2.61	2.60
	(101)	36.25	36.25	2.48	2.48
0.015 M C-ZnO	(100)	31.98	31.77	2.80	2.81
	(002)	34.43	34.42	2.60	2.60
	(101)	36.42	36.25	2.48	2.48
0.02 M C-ZnO	(100)	31.82	31.77	2.81	2.81
	(002)	34.53	34.42	2.60	2.60
	(101)	36.25	36.25	2.48	2.48
0.025 M C-ZnO	(100)	31.99	31.77	2.80	2.81
	(002)	34.43	34.42	2.61	2.60
	(101)	36.34	36.25	2.50	2.48

4.2.2. SCANNING ELECTRON MICROSCOPY (SEM)

The morphological and elemental properties of the un-doped and C-ZnO NPs prepared using a PSP technique and annealed at 400 °C were investigated using scanning electron microscopy (SEM) with energy dispersive X-ray (EDX) spectroscopy. Figures 4.3, 4.4, 4.5, 4.6, 4.7 and 4.8 show the SEM micrographs of the un-doped and C-ZnO NPs synthesized by PSP technique. SEM images for both un-doped and C-ZnO samples reveal the formation of spherical shaped ZnO NPs. The SEM micrographs reveal that the morphology and shape of both un-doped and C-ZnO change as the dopant level increase. Figure 4.3 exhibits the SEM image of the un-doped ZnO NPs consisting of a mesoporous nanostructure with small spherical nanoparticles (4-5) around a central nanoparticle. In addition, the SEM micrographs of un-doped ZnO NPs clearly reveal well defined individual smooth small nanoparticles that are easily distinguishable from each other. The EDX spectrum of the un-doped has revealed the existence of zinc (Zn), and oxygen (O) atoms in the prepared nanoparticles. The presence of Zn and O in the EDX spectra confirms the successful pyrolysis of zinc ethoxide to form ZnO nanostructures.

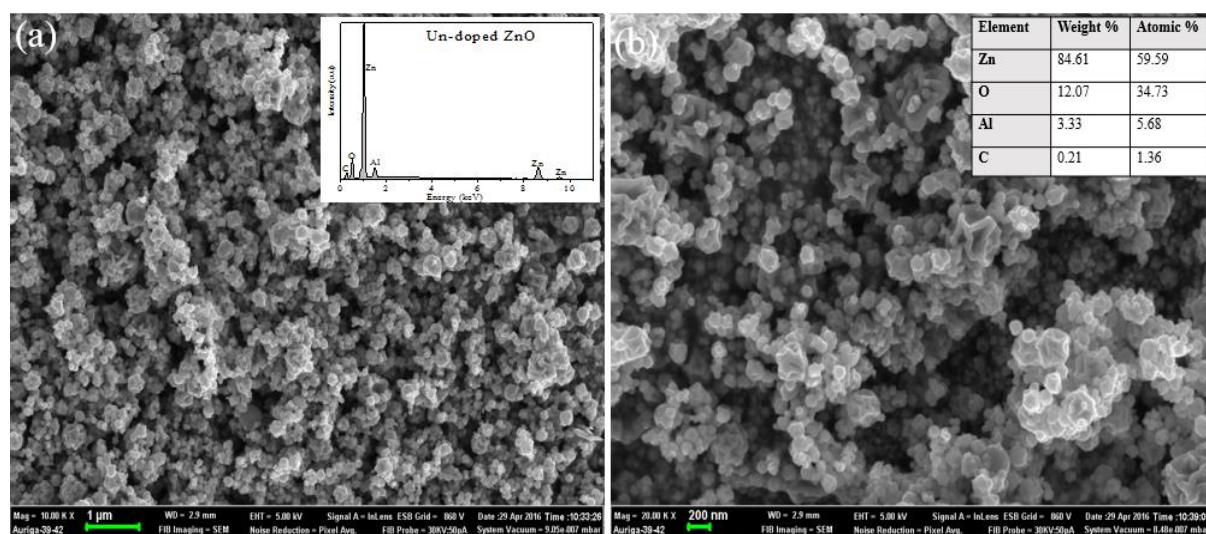


Figure 4.3: SEM micrographs of un-doped ZnO samples at different magnifications. Additionally, insert in (a) and (b) shows the elemental composition analysis by EDX and the percentage composition of elements present in the NPs of the un-doped ZnO sample respectively.

Figure 4.4 shows the SEM micrograph of 0.005 M C-ZnO NPs revealing similar nanostructure arrangement as with the un-doped ZnO sample. However, introduction of carbon into the ZnO

nanostructure results in formation of larger agglomerates. The central atom in C-ZnO NPs is far more larger as compared to the un-doped ZnO sample. Moreover there is increase in agglomeration as evidenced by the larger number of nanoclusters with larger central nanoparticle as compared to the un-doped ZnO sample. This is in support with XRD analysis which showed increase in calculated nanoparticle size with carbon doping. XRD analysis revealed the calculated NPs size for un-doped ZnO was between 11.30-12.50 nm and increased to 16.28-17.38 nm with carbon doping. In addition, close inspection of the three dominate peaks pattern for the un-doped and 0.005 C-ZnO samples revealed that carbon doping resulted in peak shifts to higher 2θ which confirms increase in particle size with carbon doping. This is in close agreement with the SEM images analysis shown in Figures 4.3 and 4.4. Furthermore, the inserts has revealed the existence of zinc (Zn), and oxygen (O) atoms in the prepared nanoparticles. The presence of Zn, O and C in the EDX spectra confirms the successful conversion of zinc ethoxide to form ZnO nanostructures

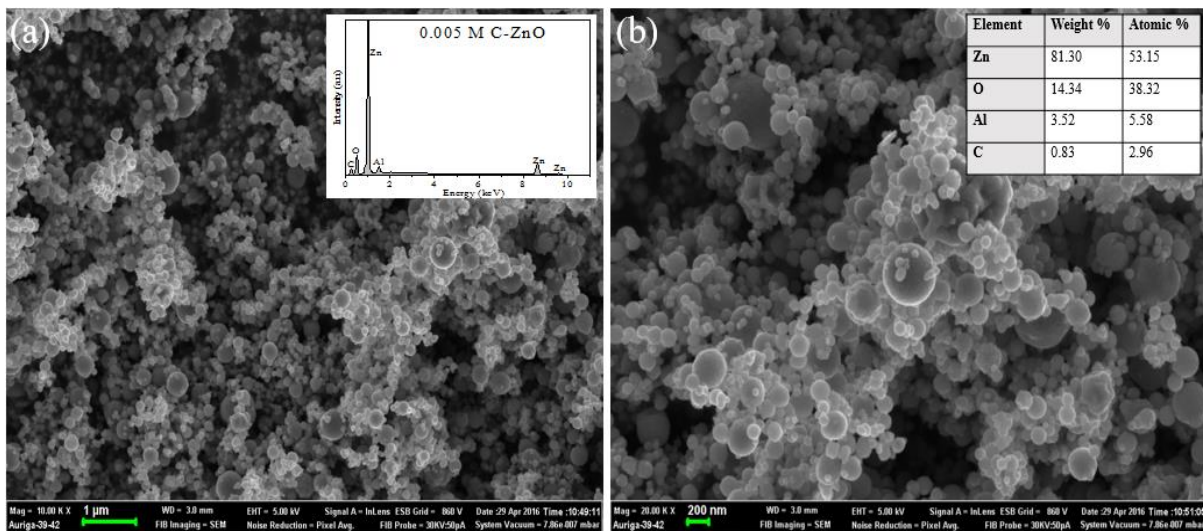


Figure 4.4: SEM micrographs of 0.005 M C-ZnO samples. Additionally insert in (a) and (b) shows the elemental composition analysis by EDX and the percentage composition of elements present in the NPs of the 0.005 M C-ZnO sample respectively.

Figure 4.5 shows SEM micrographs of the (a) 0.01 C-ZnO sample. The SEM micrographs clearly reveal formation of agglomerates consisting of 4-5 small smooth spherical nanoparticles around a much larger central nanoparticle as compared to the SEM micrographs of the un-doped and 0.005 C-ZnO sample in Figures 4.3 and 4.4. From the SEM images it can be seen that increasing carbon concentration up to 0.01 M resulted in increased agglomeration and size

of NPs. This also supports XRD analysis results which showed increase in calculated nanoparticle size with carbon doping. In addition, the EDX spectrum of the 0.01 M C-ZnO revealed the presents of zinc (Zn), and oxygen (O) atoms in the prepared nanoparticles. The presence of Zn, O and C in the EDX spectra confirms the successful pyrolysis of zinc ethoxide to form ZnO nanostructures.

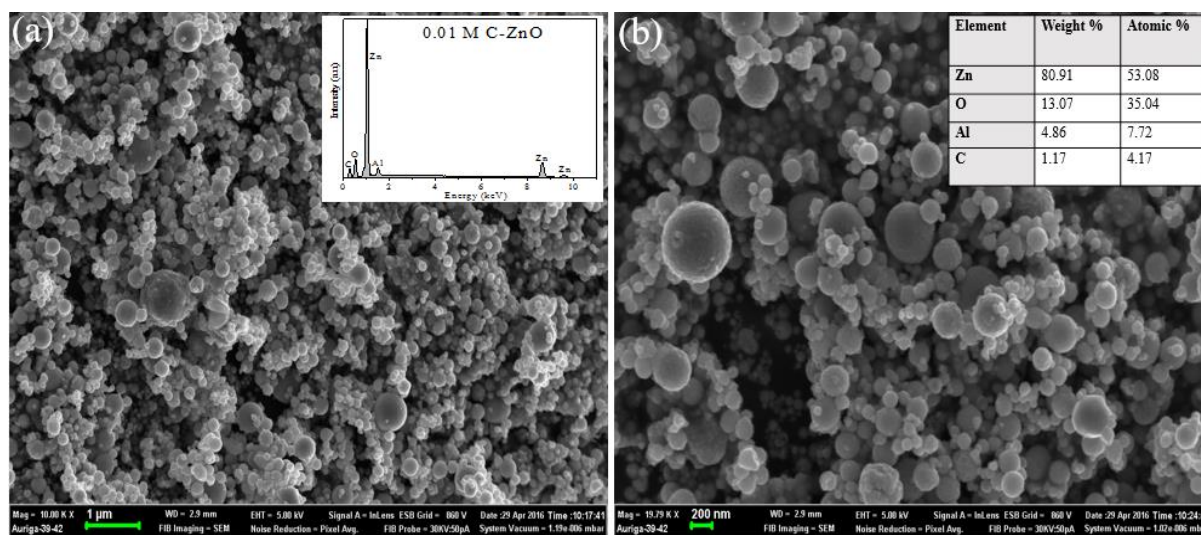


Figure 4.5: SEM micrographs of 0.01 M C-ZnO samples. Additionally insert in (a) and (b) shows the elemental composition analysis by EDX and the percentage composition of elements present in the NPs of the 0.01 M C-ZnO sample respectively.

Figure 4.6 shows SEM micrographs of the 0.015 M C-ZnO samples. The SEM micrographs also revealed the formation of agglomerates consisting of 4-5 small smooth spherical nanoparticles around a much larger central nanoparticle which is almost similar to the SEM micrograph of 0.01 C-ZnO shown in Figure 4.5 which was also observed to have larger central nanoparticle compared to the SEM micrographs shown in Figures 4.3 and 4.4. From the SEM images it can be seen that increasing carbon concentration up to above 0.01 M resulted in increased in agglomeration of NPs. This is due to the kinetic equilibrium process where the high concentration of carbonic species results in accelerated nucleation of zinc atoms with oxygen ions and carbon atoms from the dopant which led to formation of larger particles [13]. Nonetheless nanoparticle enhanced agglomeration in the presence of carbon resulted in formation of a highly mesoporous nanostructure which is the ideal electrode materials for dye sensitized solar cells (DSSC). In addition, the inserts revealed the presence of zinc (Zn), and

oxygen (O) atoms in the prepared nanoparticles. The presence of Zn, O and C in the EDX spectra confirms the successful pyrolysis of zinc ethoxide to form ZnO nanostructures.

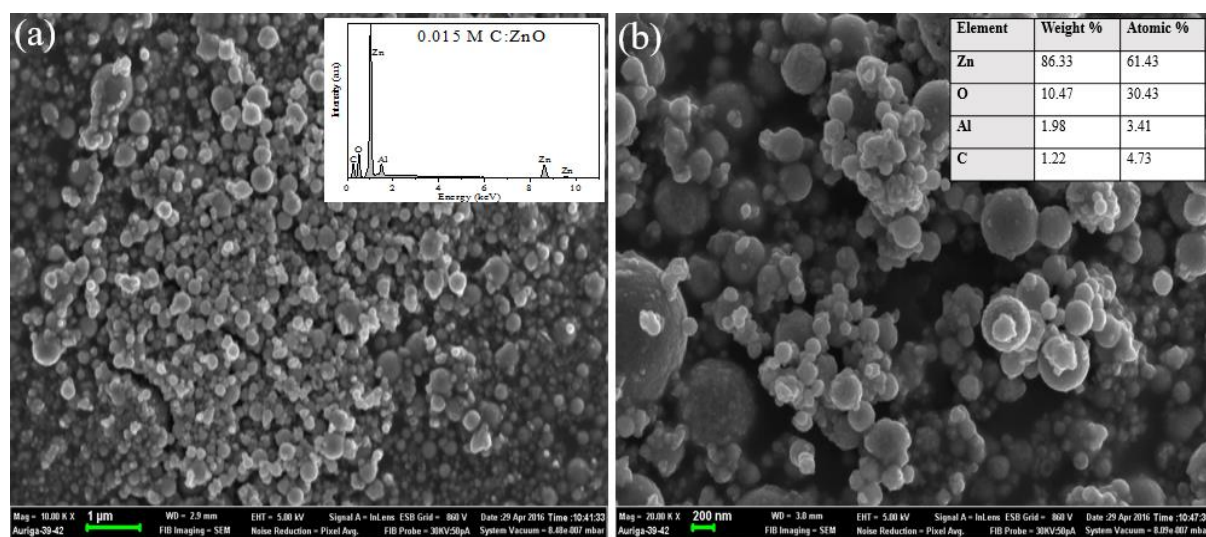


Figure 4.6: SEM micrographs of 0.015 M C-ZnO samples. Additionally insert in (a) and (b) shows the elemental composition analysis by EDX and the percentage composition of elements present in the NPs of the 0.015 M C-ZnO sample respectively.

Figure 4.7 represents the SEM micrographs of the 0.02 C-ZnO sample. The SEM micrographs clearly reveal a loss of the mesoporous morphology and the formation of dense well packed structure. It is noticed that the small spherical shaped nanoparticles have come closer together to form large cauliflower like ZnO nanoparticles. From the SEM images it can be observed that increasing carbon concentration resulted in increased agglomeration and the size of NPs. The SEM analyses of all the ZnO samples shows that the particles are of nanometer size, the particle size of the sample is always overestimated because of the distortion of SEM images [14]. It is observed that the surface morphologies of ZnO nanoparticles are influenced by the concentration of TBA dopant. Furthermore, the EDX spectrum of the 0.02 M C-ZnO has revealed the presents of zinc (Zn), and oxygen (O) atoms in the prepared nanoparticles. The presence of Zn, O and C in the EDX spectra confirms the successful pyrolysis of zinc ethoxide to form ZnO nanostructures.

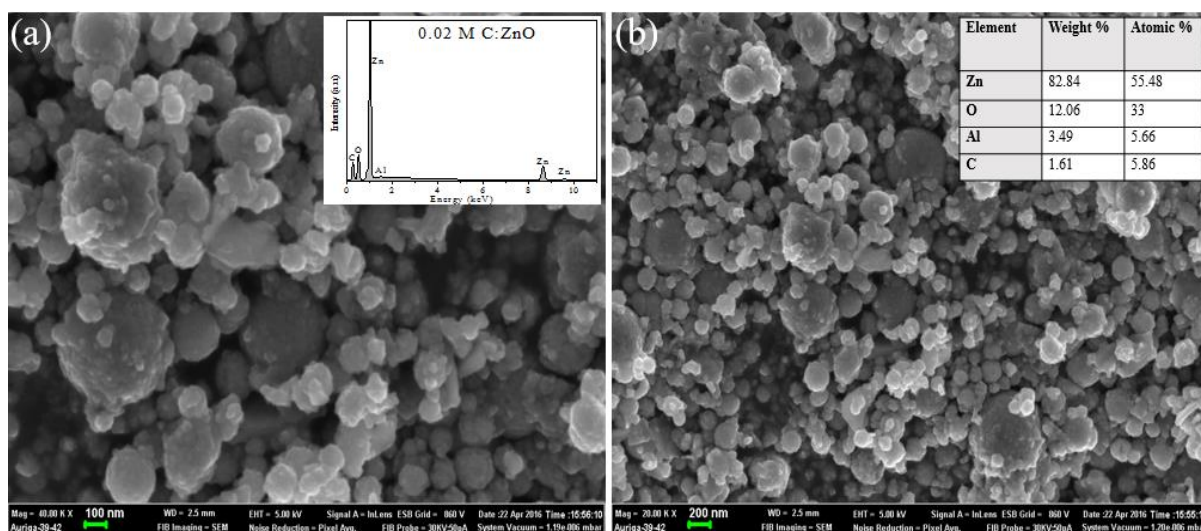


Figure 4.7: SEM micrographs of 0.02 M C-ZnO samples. Additionally insert in (a) and (b) shows the elemental composition analysis by EDX and the percentage composition of elements present in the NPs of the 0.02 M C-ZnO sample respectively.

Figure 4.8 represents the SEM micrographs of the 0.025 M C-ZnO sample revealing similar nanostructure arrangement as with the 0.02 M C-ZnO sample in Figure 4.7. The SEM micrographs have also revealed the formation of cauliflower like ZnO including nanoclusters are observed on the surface of the ZnO nanoparticles. It is noticed that the small spherical shaped nanoparticles have come closer together to form large cauliflower like ZnO nanoparticles. The central atom in the 0.025 M C-ZnO NPs is far more larger as compared to the other PSP synthesized ZnO samples. This suggest that the introduction of carbon catalyses the rate of NPs agglomeration. Moreover, the increase in agglomeration is evidenced by the larger number of nanoclusters with larger central nanoparticle as compared to that of the other ZnO samples. This supports XRD analysis which showed an increase in calculated nanoparticle size with carbon doping. The calculation of ZnO NP size by the Scherrer equation have revealed that the as synthesized ZnO NPs un-doped, 0.005 TBA, 0.01 TBA, 0.015 TBA, 0.02 TBA and 0.025 TBA doped have a particle size range of (9.60-12.50); (16.28-17.38); (9.99-13.68); (9.96-12.40); (9.98-12.63) and (10.22-14.03) respectively. In addition on close inspection of the three dominant peaks pattern for the un-doped and C-ZnO samples revealed that carbon doping resulted in peak shifts to higher 2θ which confirms increase in particle size with carbon doping. This is in close agreement with the SEM image analysis shown in Figures 4.3, 4.4, 4.5, 4.6, 4.7 and 4.8. The SEM analyses of all the PSP synthesized ZnO samples has shown that the particles are of nanometer size, the particle size of the sample is always

overestimated because of the distortion of SEM images [14]. We can conclude that the surface morphologies of ZnO nanoparticles are influenced by the concentration of TBA dopant.

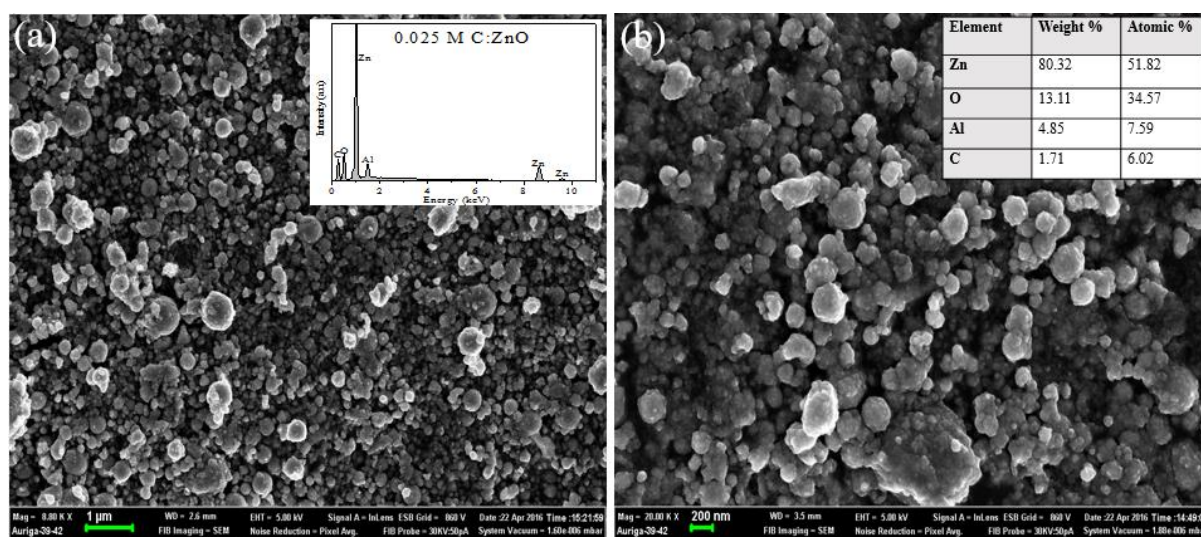


Figure 4.8: SEM micrographs of 0.025 M C-ZnO samples. Additionally insert in (a) and (b) shows the elemental composition analysis by EDX and the percentage composition of elements present in the NPs of the 0.025 M C-ZnO sample respectively.

Elemental analyses of the un-doped and carbon doped ZnO samples were performed by energy dispersive X-ray (EDX) spectroscopy using a scanning electron microscope (SEM). The EDX analysis was used to determine the chemical composition of the ZnO nanoparticles. Inserts in Figures 4.3, 4.4, 4.5, 4.6, 4.7 and 4.8, show the elemental composition analysis of the ZnO samples. The EDX spectra of the un-doped ZnO sample and carbon doped ZnO samples shown in Figures 4.3 (a), 4.4 (a), 4.5 (a), 4.6 (a), 4.7 (a), and 4.8 (a), reveal prominent EDX peaks at 0.51 keV, 1.01 keV, 1.49 keV, 8.87 keV and 9.86 keV. The X-ray energies of 0.51 keV and 1.01 keV represent the emissions from the K-shell of oxygen and L-shell of zinc respectively. The X-ray energies at 8.87 keV and 9.86 keV are additional emissions from Zn core levels [7].

The EDX spectrum of the un-doped and C-doped ZnO revealed the existence of zinc (Zn), and oxygen (O) atoms in the prepared nanoparticles. The presence of Zn, O and C in the EDX spectra confirms the successful pyrolysis of zinc ethoxide to form ZnO nanostructures as illustrated in Chapter 2 by Equations 2.11 and 2.12. The presence of carbon (C) core level emission at 0.28 keV in the un-doped ZnO sample in Figure 4.3 appeared probably due to the carbon tape that was used for the preparation of the sample as it is observed at a very low

intensity compared to those of TBA doped samples. In Figures 4.4, 4.5, 4.6, 4.7 and 4.8, the presence of carbon (C) together with Zn and O atoms were shown by the EDX pattern of the C-doped samples indicating the effective doping of the carbon in the ZnO matrix. In addition, the EDX analysis of the percentage composition analysis (wt %) reveal that the percentage composition of the carbon doped increased from 0.83 up to 1.22 in the carbon doped ZnO samples. Therefore we can confirm effective doping of carbon in our ZnO nanostructures. Additionally the EDX spectra of all the samples reveal the presence of Al in ZnO samples, this is due to the aluminium tube reactors and aluminium substrate holder employed in our spray pyrolysis system.

The weight and atomic percent composition of the elements involved in the ZnO nanoparticles such as oxygen, zinc, aluminium and carbon for each sample are shown in the inserts in Figures 4.3 (b), 4.4 (b), 4.5 (b), 4.6 (b), 4.7 (b), and 4.8 (b). It is clear that the synthesized nanoparticles are composed of C, Zn and O atoms for the un-doped and for the carbon doped ZnO nanoparticles. In the un-doped ZnO sample it observed that carbon occurs at a very low percentage compared to that of doped ZnO samples. The atomic percentage of carbon in the C-ZnO samples increases with an increase in TBA dopant concentration from 2.96 % to 6.02 % [13]. It is noticed from the table that both un-doped and carbon doped samples shows high percentage composition of zinc than other elements which means the prepared ZnO samples are rich in Zn.

4.2.3. HIGH RESOLUTION TRANSMISSION ELECTRON MICROSCOPE (HRTEM)

High resolution transmission electron microscope (TEM) was used to determine the structural properties of ZnO NPs synthesized by PSP technique. In HRTEM, electron beams focused by electromagnetic lines are transmitted through a thin sample of ZnO nanopowders. High resolution transmission electro-microscopy images of the ZnO Samples are shown in Figures 4.9, 4.10, 4.11, 4.12 and 4.13. HRTEM images have revealed that the synthesized nanoparticles are spherical, are clustered and agglomerated which is in close agreement with SEM observations shown in Section 4.2.2 above. In addition, HRTEM analysis revealed that the un-doped ZnO, 0.005 M C-ZnO, 0.01 M C-ZnO, 0.015 M C-ZnO and 0.02 M C-ZnO have spherical modal particle diameter of about 8.80 nm, 8.93 nm, 10.46 ,11.82 nm and 13.79 nm respectively. It is observed that the particle size of the ZnO nanoparticles estimated using HRTEM is in close agreement from those calculated from Scherer equation from XRD analysis

shown in Table 4.3. In addition, the results shown by HRTEM images of the un-doped and carbon doped ZnO samples were in agreement with that of the SEM micrographs in confirming the morphology of the ZnO nanoparticles. Moreover, the selected area electron diffraction (SAED) of all the synthesized ZnO samples revealed the hexagonal pattern of sharp spots which indicates the monocrystalline nature with symmetrical orientation of the ZnO nanoparticles in the sample.

Table 4.3: *The comparison of the particle size calculated from XRD with the particle size estimated by HRTEM.*

Sample #	XRD Particle Size (nm)	HRTEM Particle Size (nm)
Un-doped	9.60 - 11.30	7.54 - 8.80
0.005 M C-ZnO	16.28 - 17.38	6.65 - 11.20
0.01 M C-ZnO	9.99 - 13.68	10.11 - 10.46
0.015 M C-ZnO	9.96 - 12.40	9.93 - 14.21
0.02 M C-ZnO	9.98 - 12.63	7.50 - 13.79

Furthermore, Figure 4.9 (a) shows the highly crystalline structure of the un-doped ZnO nanoparticles with the spacing between adjacent lattice planes of 0.26 nm and 0.28 nm corresponding to the distance between two planes (002) and (001) crystal planes of ZnO, respectively. The lattice spacing of 0.2602 is in good agreement with the d-spacing of (002) planes of hexagonal Wurtzite ZnO structure [15]. The HRTEM analysis is consistent with the XRD results. The corresponding selected area electron diffraction pattern Figure 4.9 (b) (insert) obtained from the same spot of measurement also verifies the presence of (002) and (001) crystal planes of ZnO.

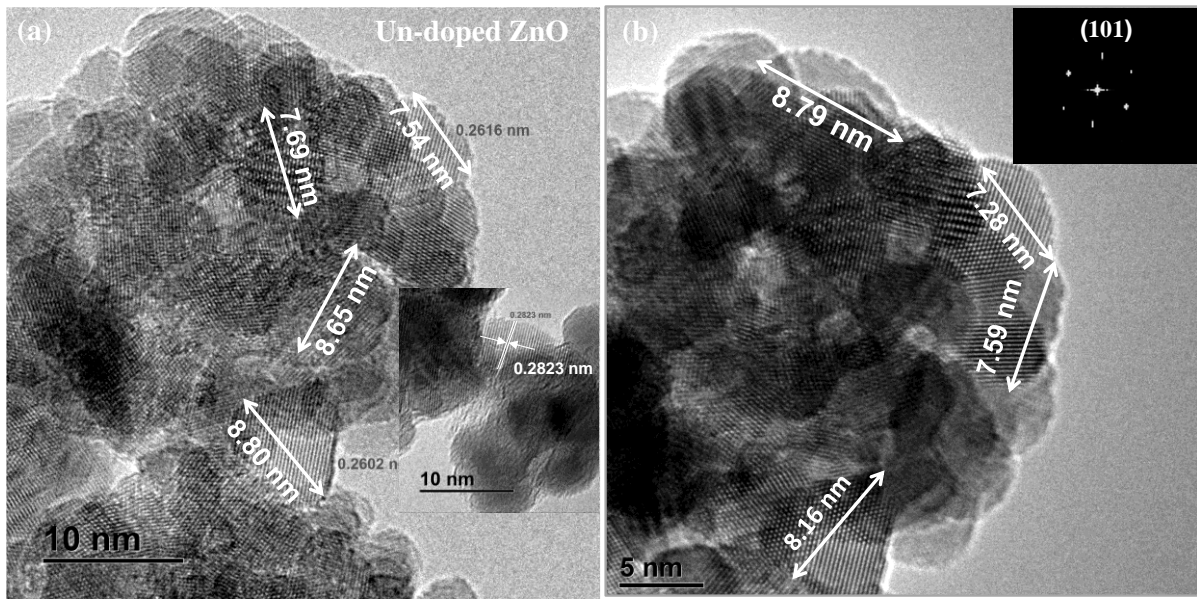


Figure 4.9: HRTEM images of un-doped ZnO nanoparticles showing the same sample at different magnifications. The insert at (a) lattice spacing (b) SAED pattern of the ZnO nanoparticles.

Figure 4.10 shows the HRTEM images of 0.005 C-ZnO samples synthesized by PSP technique. HRTEM image analysis has revealed lattice spacings of 0.2753 nm and 0.2435 nm corresponding to lattice plane of (100) and (101) of hexagonal Wurtzite ZnO structure [15, 16]. The lattice spacing of 0.2753 is somewhat greater than that of pure ZnO (0.26 nm). The HRTEM analysis is consistent with the XRD results, which further confirms substitutional replacement of the oxygen atom with the carbon atom in lattice structure of hexagonal Wurtzite ZnO. Moreover, the selected area electron diffraction image in Figure 4.10 (b) has confirmed the presence of (101) planes of ZnO in the 0.005 M C-ZnO samples.

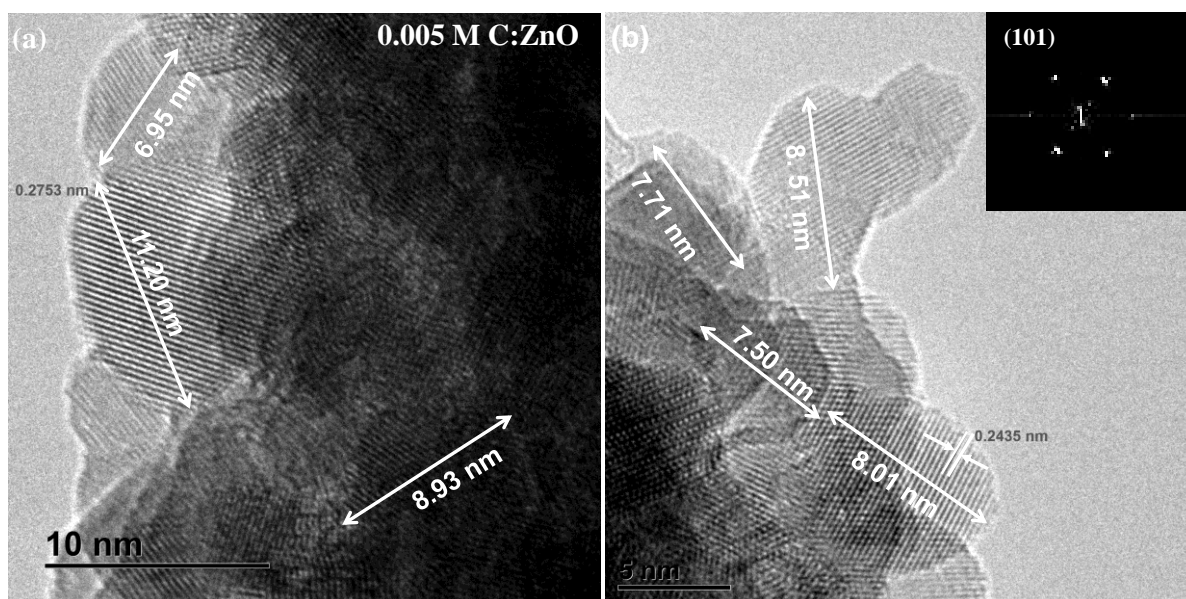


Figure 4.10: HRTEM images of 0.005 M C-ZnO nanoparticles showing the same sample at different magnifications. The insert at (b) shows the SAED pattern of the ZnO nanoparticles.

The lattice spacings for the 0.01 M C-ZnO and 0.015 M C-ZnO nanoparticles are shown in Figures 4.11 and 4.12. HRTEM analysis has revealed lattice spacing of 0.28 nm and 0.25 nm which correspond to lattice plane of (100) and (101) of hexagonal Wurtzite ZnO structure for the 0.01 M C-ZnO sample. In addition, HRTEM analysis has revealed lattice spacing of 0.2776 which is close to the lattice spacing of 0.28 nm of (100) lattice plane of ZnO for the 0.015 M C-ZnO. In fact, all lattice parameters of the PSP synthesized samples remained intact, as all interplanar spacings determined through HRTEM images correspond to the planes of Wurtzite ZnO which already has been confirmed through XRD analysis.

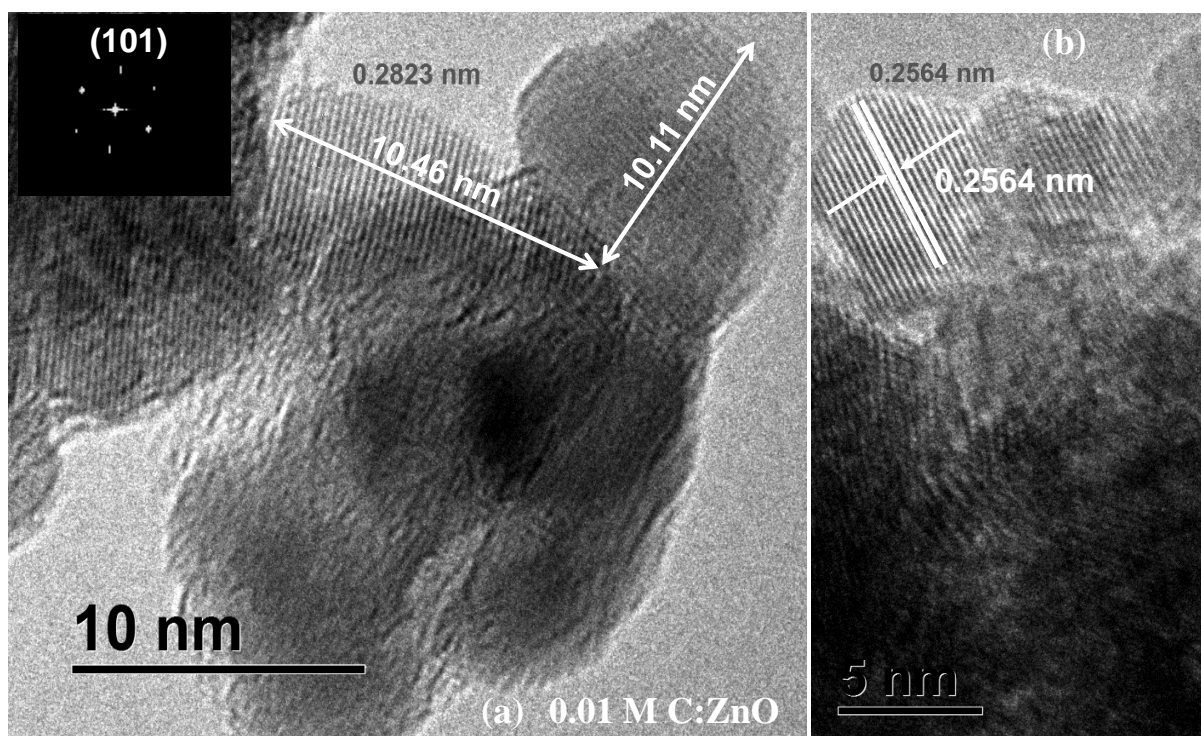


Figure 4.11: HRTEM images of 0.01 M C-ZnO nanoparticles showing the same sample at different magnifications. The insert at (a) shows the SAED pattern of the ZnO nanoparticles.

Furthermore, all the selected electron diffraction (SAED) patterns of the 0.01 M C- ZnO and 0.015 M C-Zn) nanoparticles have revealed a consistent pattern similar to that of the un-doped sample in Figure 4.9 (b) which further confirms that carbon doped ZnO have crystalline Wurtzite ZnO structure. This is in close agreement with the XRD analysis and the lattice spacings of the four samples do not differ that much.

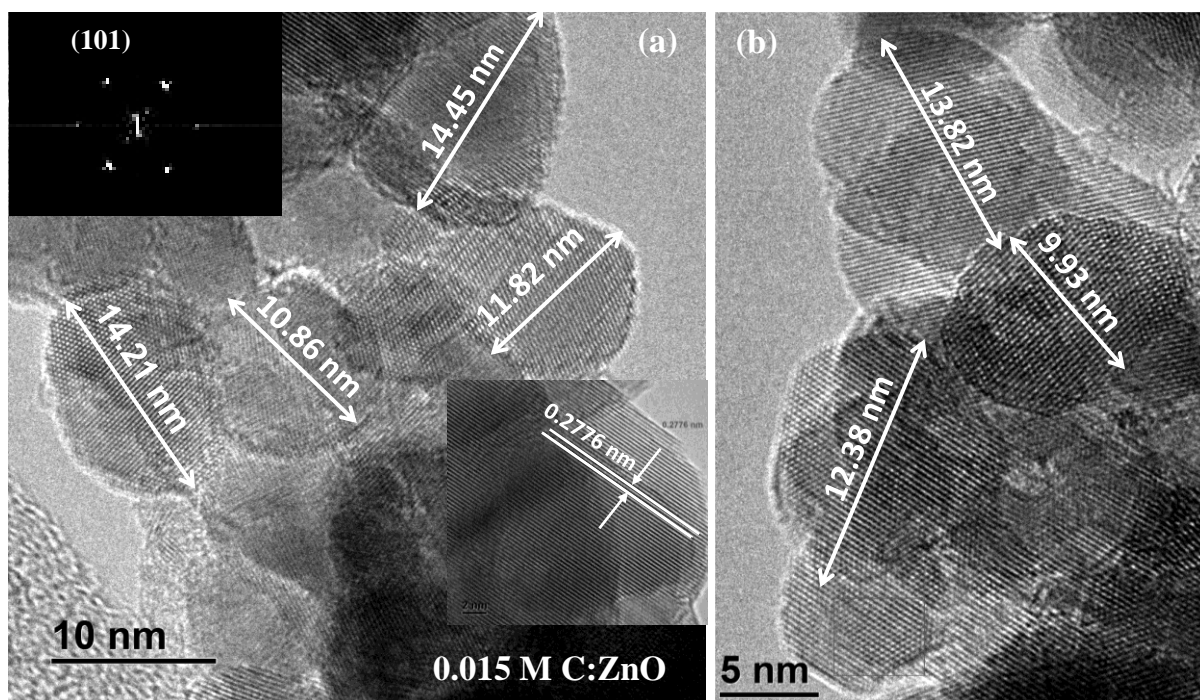


Figure 4.12: HRTEM images of 0.015 M C-ZnO nanoparticles showing the same sample at different magnifications. The insert at (a) shows the SAED pattern of the ZnO nanoparticles.

The TEM images of the 0.02 M ZnO nanoparticles at different magnifications are shown in Figure 4.13. The HRTEM image analysis has revealed a lattice spacing of 0.2517 nm which correspond to lattice plane of (101) of the hexagonal Wurtzite ZnO structure. In addition, the HRTEM analysis is consistent with the XRD results, which further confirms substitutional replacement of the oxygen atom with the carbon atom in the lattice structure of hexagonal Wurtzite ZnO. Moreover, the selected area electron diffraction image in Figure 4.13 (b) has confirmed the presence of (101) planes of ZnO in the 0.02 M C-ZnO samples.

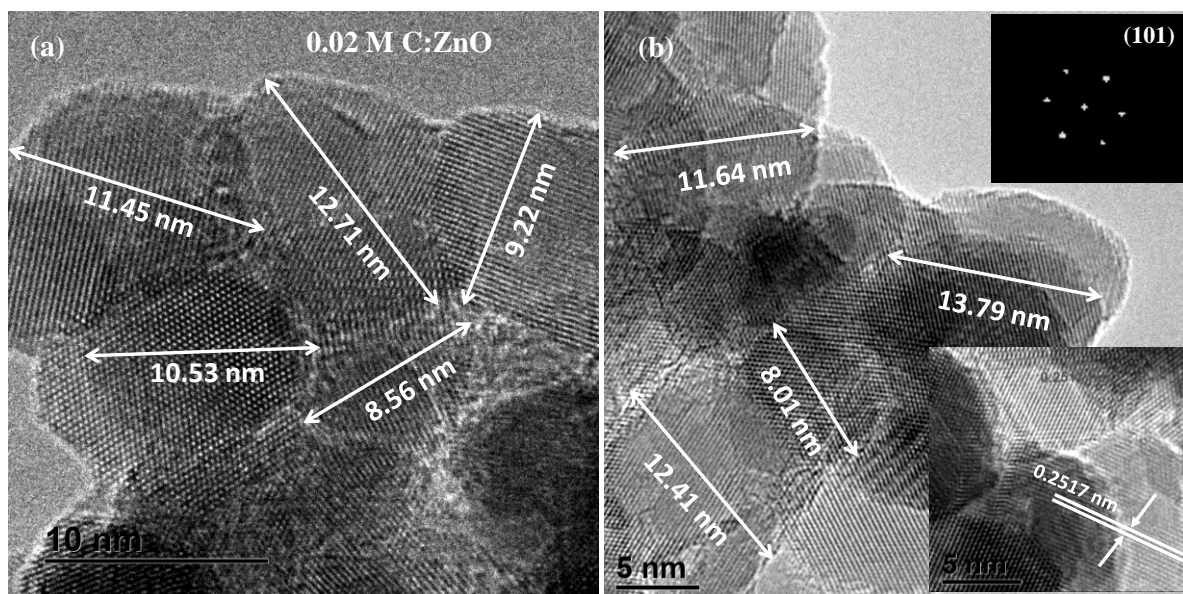


Figure 4.13: HRTEM images of 0.015 M C-ZnO nanoparticles showing the same sample at different magnifications. The insert at (a) shows the SAED pattern of the ZnO nanoparticles.

Moreover, increase in carbon doping with the estimated particle size is consistent with XRD measurements and we also observed an increase in modal particle size as the concentration of carbon increased and this again confirms the successful incorporation of C in ZnO using the PSP technique which is in agreement with XRD observations. In all the TEM images it is observed that the synthesized ZnO samples have the same crystal structure but different particle sizes and this difference in particles size is probably due to the fact that the nanoparticles are being formed or deposited at different times [17]. The crystal sizes of the nanoparticles held at a certain degree of agglomeration are found to be increased while the surface area decreases as concentration of dopant gradually increased. The agglomeration of ZnO nanoparticles became extremely serious at higher dopant concentration hence the particle size increased. This might be described as sample effect result from two main effects: that is the particle size increase from the finite extent and specific morphology of the coherently diffracting areas inside the grains and the microstrain widening, which results from local variations of the d-spacing created by nonuniform crystalline stresses [18]. In conclusion the average particle size of the ZnO nanoparticles as revealed by TEM analysis is less than 40 nm and this indicates clearly that the ZnO nanoparticles are highly crystalline with hexagonal Wurtzite structure.

4.2.4. RAMAN SPECTROSCOPY ANALYSIS

In order to investigate the effect of carbon doping on the structural properties of ZnO NPs we employed Raman spectroscopy to investigate the change in the vibrational modes of C-ZnO NPs. It has been reported that Raman spectra of ZnO nanostructures is sensitive. Hence it shows shift of the bulk phonon frequencies [19]. The shift in Raman spectra can arise due to structural disorder, defects (oxygen deficiency, surface impurities) and phonon confinement [19]. In order to cross examine the vibrational properties of C-ZnO NPs and effect of carbon doping on structure, phase and other related parameters Raman spectroscopy of un-doped and C-ZnO was measured. Theoretically, ZnO has a Wurtzite structure, which belongs to the space group C_{6v}^4 , with two formula units per primitive cell where all atoms are occupying the 2b sites of the symmetry C_{3v} [16, 19, 20]. For a perfect ZnO crystal, only the optical phonons at Γ point group of the Brillouin zone are involved in the first order Raman scattering [20]. Zone centre optical phonons predict the existence of the following modes: $\Gamma_{opt} = A_1 + 2B_1 + E_1 + 2E_2$ [8]. The, A_1 and E_1 modes are polar. The polar modes are split further into transverse optical (A_1 TO and E_1 TO) and longitudinal optical (A_1 LO and E_1 LO) components. E_2 mode consist of two modes of low and high frequency phonons (E_2 low and E_2 high). The E_2 low is related with the vibration of heavy Zn sublattice, whereas the E_2 high mode is related vibration of oxygen atoms only. Additional to the first Raman modes identified above there are also second order Raman vibrational modes. Characteristic of second order Raman modes are the B_1 which is silent. The B_1 (low) and B_1 (high) modes have vibrational frequencies at 260 cm^{-1} and 540 cm^{-1} , respectively [22, 23]. Table 4.4 summarizes the list of the frequency and symmetry first, second and multi-phonon modes found in ZnO nanostructure from various literature sources. For the sake of comparison Table 4.4 also presents the experimental values of Raman vibrational frequencies and symmetry compiled from various literature sources.

Table 4.4 Frequency and symmetry of the fundamental theoretical modes in bulk ZnO and experimental values compiled from various literature sources [7, 21, 25, 26]

Character and Symmetry/ Frequency	Experimental frequencies ZnO nanostructures			
	Bulk (cm ⁻¹)	Films (cm ⁻¹)	ZnO crystals (cm ⁻¹)	Polished crystals
E₂^{low}	101	99	99	101
E₂^{high}	437	440	439	437
A₁(TO)	375	380	382	380
E₁(TO)	405	414	413	408
A₁(LO)	574	-	579	574
E₁(LO)	578	583	591	584
Frequency of the fundamental multi-phonon modes in ZnO found in literature				
208 cm⁻¹ 330, 334 cm⁻¹E_{2H} – E_{2L} broad, from 540-670 cm⁻¹, broad, from 540-670 cm⁻¹, 986 cm⁻¹ Broad starts at 1050 cm⁻¹, peaks at 1084 and 1149 cm⁻¹				

Raman spectra for all samples are shown in Figure 4.14. Table 4.5 shows the peak positions and symmetry of the identified peaks. The Raman spectra of the un-doped ZnO samples show the $B_1(low)$ broad peak at 297.30 cm⁻¹. This mode normally exists in ZnO samples with lattice defects caused by the presence of impurities either of dopant nature or due to growth conditions [21]. The $B_1(low)$ mode has been observed in un-doped ZnO films grown by RF sputtering which was attributed to disorder-activated Raman scattering [21, 22]. Hence we can speculate that this mode in our samples was caused by the presence of defects due to growth conditions. Surprisingly we did not observed the $B_1(low)$ mode in the C-ZnO samples.

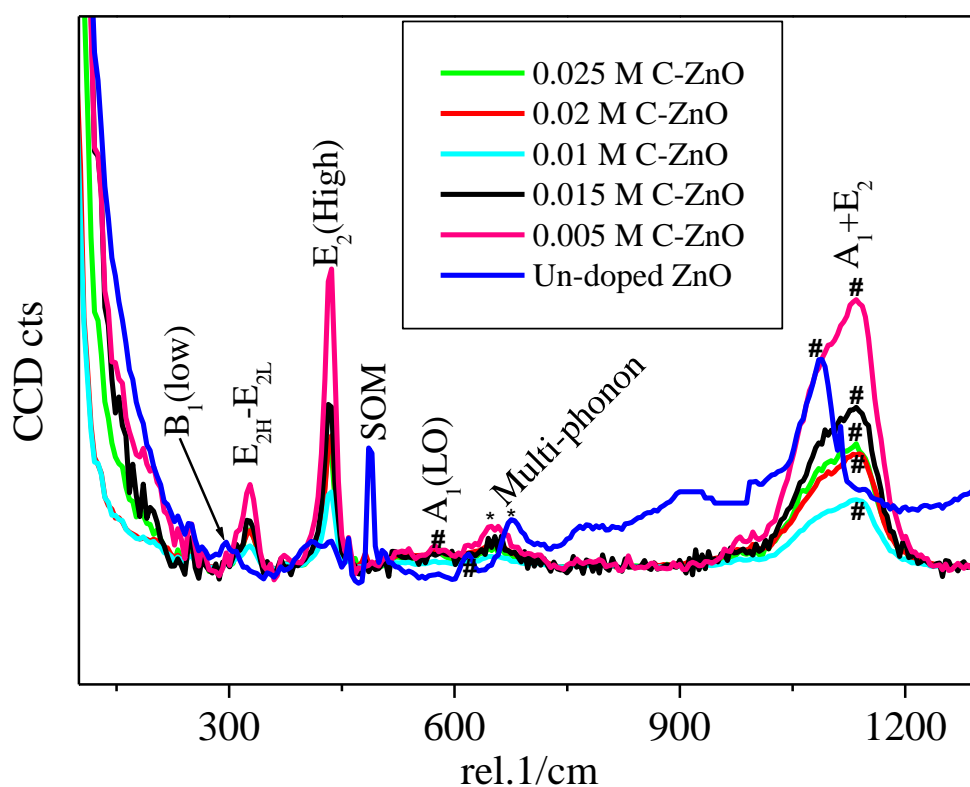


Figure 4.14: Raman spectra of un-doped and C-ZnO samples fabricated by a PSP technique.

The Raman spectra of C-ZnO samples showed the existence of $E_{2H} - E_{2L}$ multi-phonon mode at the same time this multi-phonon mode does not exist in the Raman spectra of un-doped ZnO samples. The $E_{2H} - E_{2L}$ multi-phonon mode commonly observed at 330 cm^{-1} or 334 cm^{-1} for bulk ZnO samples [19, 20, 21] was blue shifted to lower frequencies and was observed for the C-ZnO samples at 325.79 cm^{-1} , 325.80 cm^{-1} , 325.96 cm^{-1} , 326.3 cm^{-1} , and 325.9 cm^{-1} for 0.005 M C-ZnO, 0.01 M C-ZnO, 0.015 M C-ZnO, 0.02 M C-ZnO and 0.025 M C-ZnO NPs respectively. Since the carbon atom is substituting the oxygen atom in ZnO lattice because of the smaller ionic radius of O as compared to that of C, we expected the $E_{2H} - E_{2L}$ multi-phonon to be shifted to higher wavenumbers. Hence we can speculate that the blue shift in our Raman spectra might be due particle size increase. It might also be due to scattering energy loss of the two phonon process due to carbon doping. Notably, from the Raman spectra samples, we observed a characteristic Raman vibration mode of the dominant $E_2(\text{high})$ of Wurtzite ZnO at 438.63 cm^{-1} commonly observed for bulk ZnO samples at 437 cm^{-1} [21] which was also shifted

to higher frequencies for the un-doped ZnO sample as illustrated in Figure 4.15 (a). Figure 4.15 shows carbon dopant concentration dependence of Raman peak shift, full width at half maximum (FWHM), and peak intensity of the $E_2(\text{high})$ mode of Wurtzite ZnO samples synthesized by PSP technique. It is clearly evident from Figure 4.15 that the vibrational frequency, full width at half maximum (FWHM) and intensity are strongly dependent on the concentration carbon dopant. It is also evident from Figure 4.15 (b) that there were vibrational frequency shifts to lower frequencies in presence of carbon dopant. Our Raman spectra of C-ZnO NPs showed Raman peaks at 433.99 cm^{-1} , 434.36 cm^{-1} , 433.78 cm^{-1} , 434.37 cm^{-1} and 433.65 cm^{-1} for 0.005 M C-ZnO, 0.01 M, 0.015 M C-ZnO, 0.02 M C-ZnO and 0.025M C-ZnO respectively. Furthermore it has also been reported that $E_2(\text{high})$ in ZnO shows a significant change of the vibrational frequency more especially in the presence of foreign species (dopants/impurities). The presence of dopants in the ZnO lattice can cause a significant shift in the Raman vibrational frequency of the $E_2(\text{high})$ mode. Since the vibrational frequencies of the $E_2(\text{high})$ mode is related with vibration of oxygen atoms, substitutional doping of the oxygen atoms in the ZnO lattice might change the vibrational frequencies of the C-ZnO samples. Hence we can speculate at this stage that the red shift to lower frequency numbers can be correlated with the concentration of carbon. We can also conclude that the decrease in phonon frequency is due to both the presence of carbon dopants/impurities and inter molecular stress due to the presence of carbon atoms in the ZnO matrix. On the basis of these observations we conclude C doping in ZnO NPs is also evident through Raman peaks shift to lower frequencies.

Figure 4.15 (c) shows the carbon dopant concentration dependence of the Raman line width/ (FWHM). It is clearly evident from Figure 4.15 (c) that the FWHM decreases slowly with increase in concentration of carbon. It has also been reported that an increase in FWHM causes weakening of the Wurtzite ZnO structure [23]. Hence the decrease in the FWHM with increase in carbon concentration simply implies that doping with carbon does not weaken or distort the ZnO structure. This is agreement to other experimental observations by Kumar *et al.* [25] where they observed an increase in the FWHM with increase in the doping concentration of cobalt, this attributed to ZnO lattice distortions and hence cause weakening of Wurtzite ZnO structure due to incorporation of metal dopant cobalt. Our Raman analysis which have shown a decrease in the FWHM with increase in carbon concentration did not show any distortions or weakening of the Wurtzite ZnO structure. These findings are in mutual agreement with the HRTEM analysis that have revealed a more consistent and almost the same d spacing for our C-ZnO

samples. In fact, all of the C-ZnO samples revealed a d spacing of 0.2753 nm (0.005 M C-ZnO), 0.2823 nm and 0.2464 nm (0.01 M C-ZnO), 0.2823 nm and 0.2564 (0.015 M C-ZnO), 0.2821 nm (0.02 M C-ZnO), and 0.2776 (0.025 M C-ZnO) which in close agreement to the lattice spacings of 0.2813 nm and 0.2462 nm for bulk ZnO which corresponds to the lattice plane of (100) and (101) of hexagonal Wurtzite ZnO structure. This could be due to preferential substitution of oxygen (O) atom with carbon (C) atom in the ZnO lattice. Since the C atom has an atomic radii of 0.26 nm which is almost similar size to the oxygen atom which has an atomic radii of 0.14 nm. Substitutional doping of O with C is not expected to cause significant lattice distortions as compared to metal dopants like cobalt or nickel with atomic radii of 0.0745 nm and 0.69 nm, respectively. It has been previously reported that for Ni doped ZnO nanostructures, FWHM value for the E_2 (high) mode of less than 11 cm^{-1} signifies that the doped samples retained a good Wurtzite ZnO structure [26]. However, for our C doped ZnO samples the FWHM was estimated to be 22.578 cm^{-1} , 16.234 cm^{-1} , 15.590 cm^{-1} , 15.197 cm^{-1} , 14.684 cm^{-1} and 16.098 cm^{-1} for the un-doped ZnO, 0.005 C-ZnO, 0.01 C-ZnO, 0.015 C-ZnO, 0.02 C-ZnO and 0.025 C-ZnO samples respectively. Our samples had line shapes greater than 11 cm^{-1} and still retained the perfect ZnO Wurtzite structure. Additionally, we observed as shown in Figure 4.15 (d) that there is an increase in peak intensity with increase in C dopant concentration.

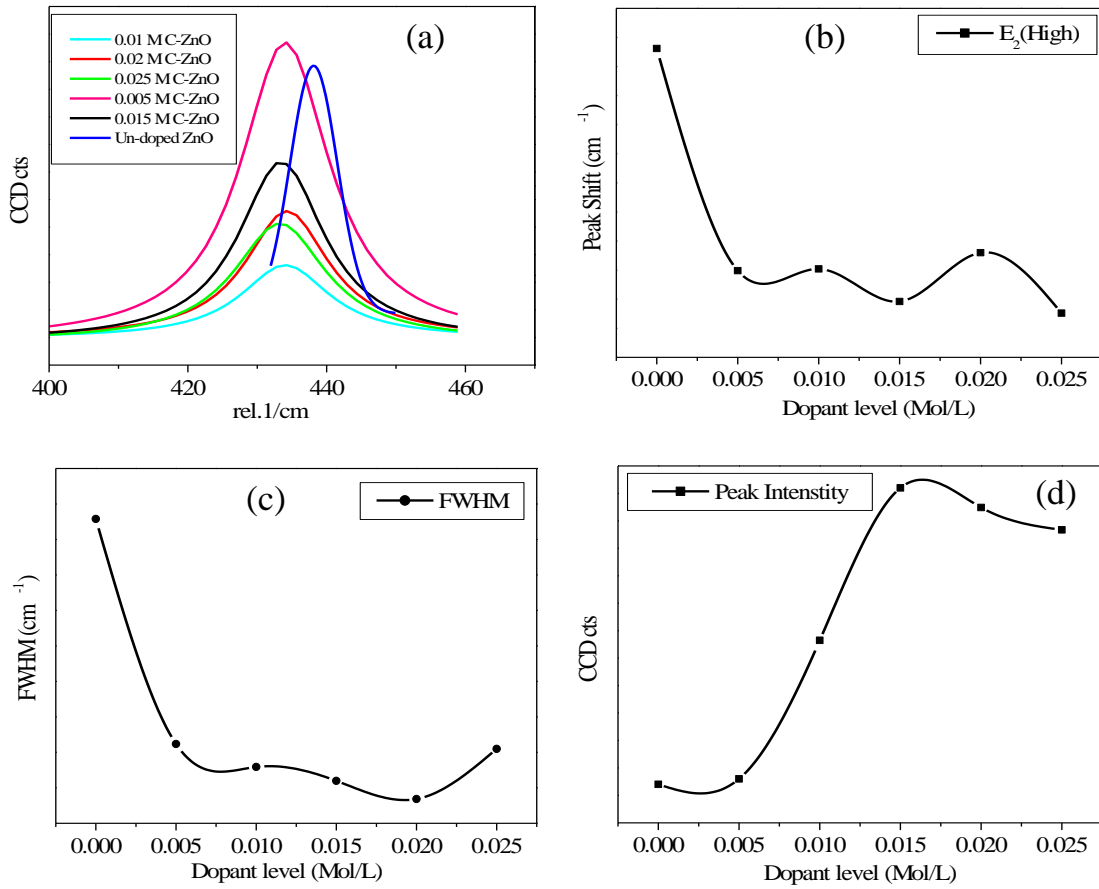


Figure 4.15: Carbon dopant concentration dependence of Raman peak shift, (a) peak of the E_2 (high) mode, (b) peak shift in E_2 (high) mode, (c) full width at half Maximum (FWHM), and (d) peak intensity of the E_2 (high) mode of Wurtzite ZnO samples synthesized by PSP technique.

It has been reported that intrinsic defects (vacancies, interstitials, anti-site) as compared to extrinsic defects are less beneficial for photo-catalysis application mainly because extrinsic defects are located at the grain boundaries hence accessible during photo catalysis reactions [27]. In bulk ZnO, the Raman mode at 680 cm^{-1} is associated with intrinsic defects. We have observed a less beneficial defect in our un-doped ZnO sample with a vibration frequency of 678.62 cm^{-1} which is rather red shifted which shows that there is reduction of lattice defects in the PSP fabricated samples. Further analysis of carbon dopant concentration dependence of Raman peak shift, full width at half maximum (FWHM), and peak intensity of this intrinsic defect is shown in Figure 4.16. It is clearly evident from Figure 4.16 (a) and 4.16 (b) that there is a significant peak shift to lower wave numbers on introduction of carbon dopant. This mode

shifts for C doped samples to 653.32 cm^{-1} , 653.09 cm^{-1} , 654.12 cm^{-1} , 653.56 cm^{-1} , and 652.47 cm^{-1} for 0.005 M C-ZnO, 0.01M C-ZnO, 0.015 M C-ZnO, 0.02M C-ZnO and 0.025 M C-ZnO NPs, respectively.

This simply indicates that the introduction of carbon decreases the presence of intrinsic defects in our ZnO samples, this is beneficial for solar cell applications. Moreover analysis of the FWHM of this mode has revealed an increase with increase in carbon dopant level and it decreases again as shown in Figure 4.15 (c). This increase is attributed to substitutional carbon doping in our samples and a decrease in intrinsic defects in our PSP fabricated ZnO samples. The decrease in intrinsic defects can be correlated to increase in extrinsic defects which are caused by the impurities due to carbon doping which are much more beneficial for solar cell applications. The relationship between peak intensity and carbon dopant level shown in Figure 4.16 (d) shows a similar pattern. Hence the relationships between Raman peak shifts, FWHM and peak intensity of the intrinsic mode can also be used as indicative evidence to support substitutional carbon doping in ZnO NPs and an indication of decrease of intrinsic defects in ZnO samples.

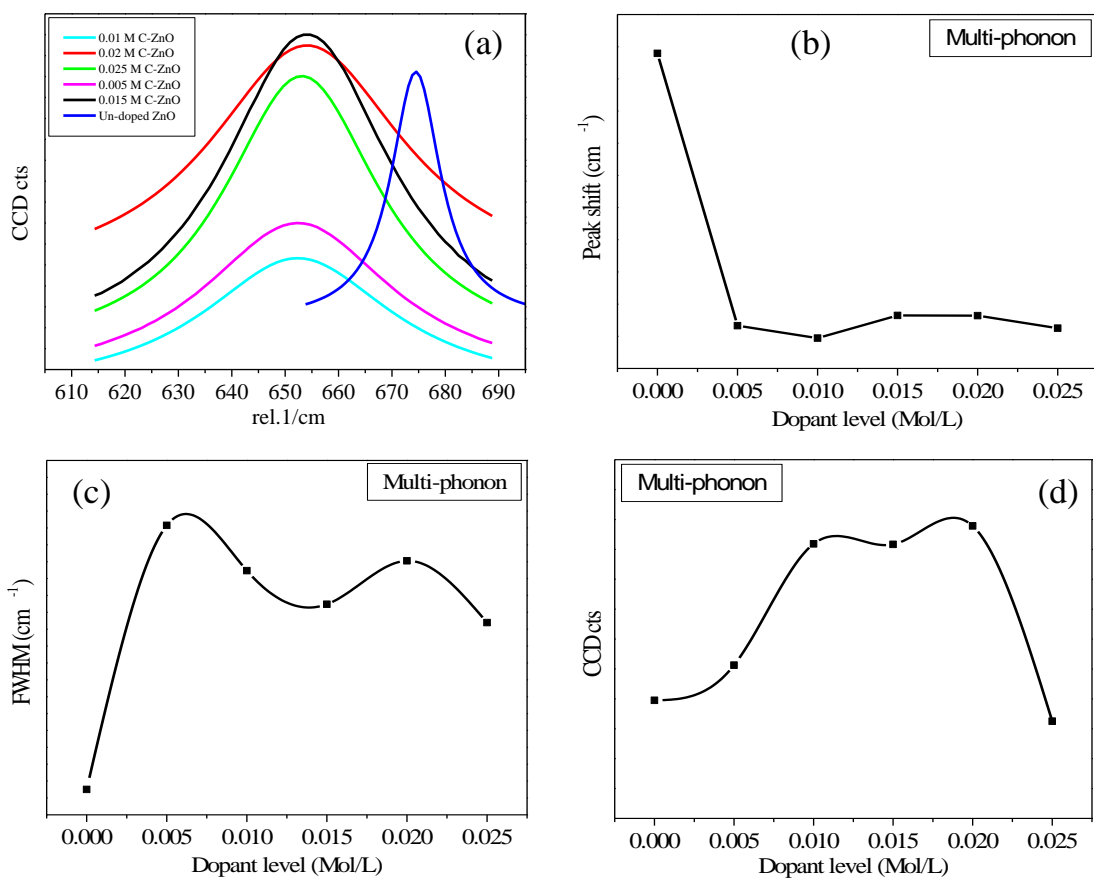


Figure 4.16 Carbon dopant concentration dependence of Raman peak shift, (a) multi-phonon peak, (b) peak shift in the multiphonon, (c) full width at half Maximum (FWHM), and (d) peak intensity of the Raman mode at 678.62 cm⁻¹

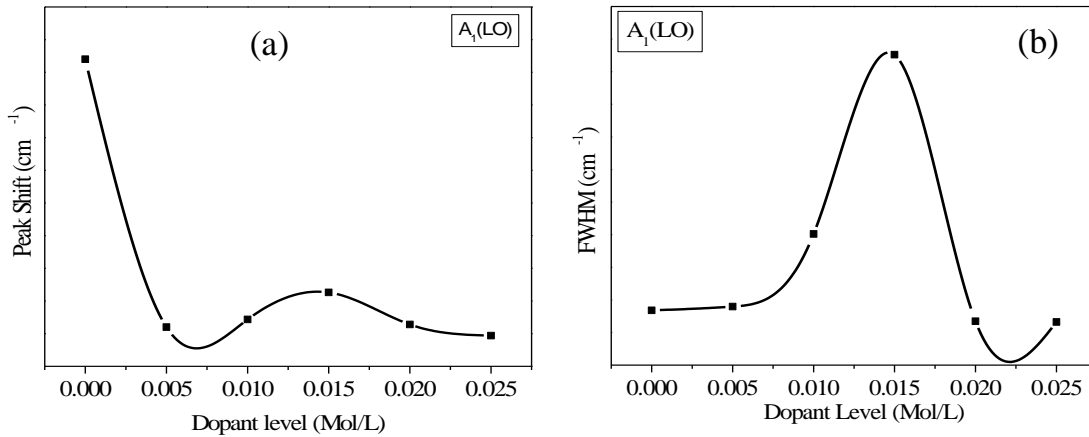


Figure 4.17: Carbon dopant concentration dependence of, (a) Raman peak shift and (b) full width at half Maximum (FWHM) of the Raman mode at 618.68 cm^{-1}

The $A_1(\text{LO})$ mode at 618.68 cm^{-1} for the un-doped ZnO samples illustrated in Figure 4.17 (a) has shown a similar shift to $E_2(\text{high})$ mode, which has revealed a Raman peak shift to lower frequencies with increase in carbon dopant concentration. The FWHM for the $A_1(\text{LO})$ has revealed a similar pattern to the multi-phonon in Figures 4.16 (c) and 4.16 (d) which has shown an increase with respective increase in carbon dopant concentration. Therefore, we can conclude that the decrease in phonon frequency of these modes accompanied by an increase in FWHM confirms the presence of carbon dopant (impurities) in our ZnO samples. It has been reported that the presence of dopants in the ZnO lattice can cause a significant shift in the Raman vibrational frequency of the $E_2(\text{high})$ mode. According to literature, the combination of acoustic phonons of the $A_1 + E_2$ is normally detected at about 1101 cm^{-1} in bulk ZnO samples [20, 21, 22, 24]. The Raman spectra of the PSP synthesized samples has shown a wide peak from 1017 cm^{-1} to 1134 cm^{-1} which is attributed to multi-phonon modes. Table 4.5 provides a summary of the symmetry and Raman modes found in PSP fabricated un-doped ZnO and C-ZnO NPs.

Table 4.5 Raman vibrational frequency of un-doped and C-ZnO NPs fabricated by PSP technique.

Sample	Frequency cm ⁻¹						
ZnO_0	297.30		438.63	488.10	618.68	678.62	1089.22
0.005 C-ZnO		325.79	433.99		575.03	653.32	1134.25
0.01 C-ZnO	-	325.81	434.36	-	574.00	653.09	1133.55
0.015 M C-ZnO		325.96	433.78		576.32	654.12	1132.40
0.02 C-ZnO	-	326.37	434.37		574	653.56	1136.03
0.025 C-ZnO	-	325.91	433.65	-	574.14	652.47	1129.94
Symmetry & Identity	B ₁ ^{low}	E _{2H} - E _{2L}	E ₂ ^{high}	SOM	A ₁ (LO)	Multi-phonon	A ₁ , E ₂ symmetry

4.3. OPTICAL CHARACTERIZATION

4.3.1. DIFFUSE REFLECTANCE SPECTROSCOPY

It is well known that the photosensitivity of semiconductors is related to their band gap [9]. The UV-Vis diffuse reflectance spectra (DRS) of the as PSP synthesized C-ZnO samples are shown in Figure 4.18 and for comparison the spectra of un-doped ZnO sample is also shown. UV-Vis DRS analysis has revealed that there is a shift in the absorption edge with increase in carbon concentration. Figure 4.18 (b) revealed an increase in absorption properties with increase in the concentration of carbon dopant. The change in absorption properties is due to the fact that the un-doped ZnO samples as calculated from XRD and HRTEM have a smaller particle size which increases with increase in carbon concentration. This confirms that introduction of carbon into ZnO lattice introduced defect states of C above the valence band or below the conduction band. [28, 29]. Moreover, it has been reported that introduction of N into ZnO lattice i.e. ZnO NO, (N substituting O) pairs was responsible for shallow acceptors that lie near the valence band edge. Similarly in this work, substitution of C also introduced the same phenomena. [28].

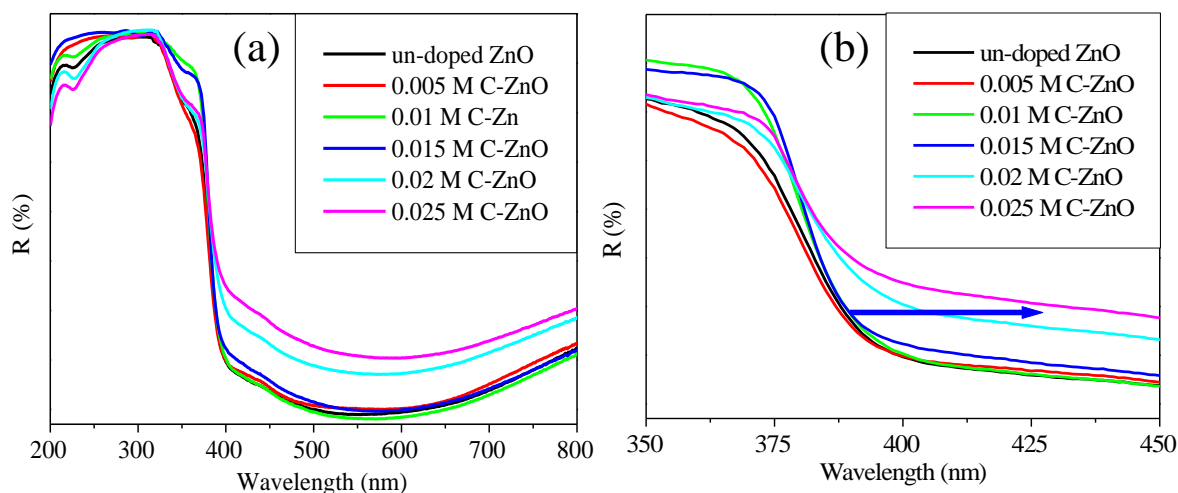


Figure 4.18: (a) The DRS spectra of the un-doped and C-ZnO samples synthesized by PSP technique (b) the extended DRS spectra 375 - 450 nm.

To quantitatively establish the type of band gap transition of the ZnO samples, the DRS data were fitted to equations for both direct and indirect band gap transitions. The profiles showed perfect fit for direct band gap transition. The energy band gaps of the thin films were estimated by using Equation (4.3) in this work.

$$E_g = \frac{1239}{\lambda_{Edge}} \quad (4.3)$$

The analysis has revealed that un-doped ZnO with modal nanoparticle size of 9.9 nm have an absorption edge at 374 nm and energy band gap of 3.31 eV. Which is larger than for bulk ZnO nanoparticle with an absorption edge at 388 nm and an energy band gap of 3.2 eV. The blue shift in the energy band gap of our PSP synthesized samples as compared to bulk ZnO as previously reported is due size confinement effect [9, 29]. However, the absorption edges for the 0.005 M, 0.01 M, 0.015 M, 0.02 M and 0.025 M C-ZnO revealed a red shift with band gap energies of 3.29 eV; 3.28 eV; 3.26 eV; 3.29 and 3.30 respectively. The red shift in absorption properties for the PSP synthesized sample in this work has been attributed to increase in particle size (as evidenced from XRD and HRTEM analysis). It can also be due substitutional carbon doping as is evident from HRTEM analysis which revealed increase in lattice parameters with increase in carbon doping and the XRD analysis which has revealed peak shift of the dominant peak to higher 2θ values with increase in carbon doping. However, we would like to point out

that for these samples to be effective materials for solar cell electrodes, there is a need to increase the nanoparticle size to above 25 nm. This can be achieved by increasing the concentration of the precursor solution to above 0.1 M.

4.4. CONCLUSION

In this study C-doped ZnO NPs have been synthesized using a pneumatic spray pyrolysis technique. SEM images for both un-doped and C-ZnO samples reveal the formation of spherical shaped ZnO NPs. The SEM micrographs revealed that the morphology and shape of both un-doped and C-ZnO changed as the dopant level increased. Moreover, SEM-EDX analysis have confirmed the presence of Zn, C and O in our samples which confirms the successfully pyrolysis of our precursor samples to ZnO nano-structures. XRD patterns of both un-doped and carbon doped ZnO samples have revealed characteristic hexagonal peaks of Wurtzite ZnO structure. XRD lines were observed at 31.90° , 34.50° , 36.34° , 47.73° , 56.88° , 63.04° , 68.20° , and 77.33° . These lines were indexed, respectively, as (100), (002), (101), (102), (110), (103), (200), and (112). XRD and HRTEM analysis have revealed an increase in nanoparticle size with increase in C-dopant concentration. Additionally, XRD analysis has revealed peak shift to higher 2θ values which is indicative of substitutional carbon doping. RS spectra of the PSP synthesized ZnO samples have shown a prominent peak at 434 cm^{-1} that is the characteristic peak of the Raman-active dominant $E_2(\text{high})$ mode of Wurtzite ZnO. Furthermore, the effect of carbon doping through Raman spectroscopy peak shifts of the E_2 high mode, $A_1(\text{LO})$ mode and multi-phonon were also examined. UV-Vis DRS analysis has revealed a red shift with increase in carbon doping.

4.5. REFERENCES

1. E. Zaleta-Alejandre, J. Camargo-Martinez A. Ramirez-Garibo M.L. Pérez-Arrieta, R. Balderas-Xicohténcatl, Z. Rivera-Alvarez, C. Falcony, C, Structural, electrical and optical properties of indium chloride doped ZnO films synthesized by ultrasonic spray pyrolysis technique, *Thin Sol. Film.*524 (2012) 44–49.
2. N. S. Kumar, K.V Bangera, G.K Shivakumar, Effect of annealing on the properties of Bi doped ZnO thin films grown by spray pyrolysis technique. *Superlatt. Microstruc.* 75 (2014) 303–310.
3. K. Rekha, M. Nirmala, M. G. Nair, A. Anukaliani, A. Structural, optical, photocatalytic and antibacterial activity of zinc oxide and manganese doped zinc oxide nanoparticles. *Physica B: Condensed Matt.* 405 (2010), 3180–3185.
4. S.S. Kumar, P. Venkateswarlu, V.R. Rao, G.N. Rao, Synthesis, characterization and optical properties of zinc oxide nanoparticles. *Int. Nano Lett.* 3 (2013) 2–6.
5. H. Sarma, D Chakraborty, K.C Sarma, Optical and structural properties of ZnO thin films fabricated by Sol-Gel method. *Mater. Sci. Appl.* 02 (2011) 340–345.
6. K. Rekha, M. Nirmala, M.G Nair, A. Anukaliani, Structural, optical, photocatalytic and antibacterial activity of zinc oxide and manganese doped zinc oxide nanoparticles. *Physica B: Condensed Matt.* 405 (2010) 3180–3185.
7. R. Kumari, A. Sahai, N. Goswami, Effect of nitrogen doping on structural and optical properties of ZnO nanoparticles. *Progress in Natural Science: Mater. Int.* 25 (2015), 300–309.
8. Y. Qiu, H. Fan, G.Tan, M. Yang, X. Yang, S. Yang, Effect of nitrogen doping on the photo-catalytic properties of nitrogen doped ZnO tetrapods, *Mat. Lett.* 131 (2014) 64–66.
9. S.M. Hosseini, I.A. Sarsari, P. Kameli, H. Salamati, Effect of Ag doping on structural, optical, and photocatalytic properties of ZnO nanoparticles, *J. Alloy. Comp.* 640 (2015) 408-415.
10. D. Zhang, M. Wang, J. Ma, G. Han, S. Li, Enhanced photocatalytic ability from carbon-doped ZnO photo-catalyst synthesized without an external carbon precursor, *F. Mater.Lett.* 7 (2014).
11. S. Aydin, G. Turgut, M. Yilmaz, M. Ertrugul, Fabrication of ZnO nanorods by simplified spray pyrolysis. *Bitlis Eren University J. Sci. Technol.* 1 (2011), 1–3.

12. S.A. Yousif, Effects of Cd, F and Fe dopants on the physical properties of ZnO thin films synthesized by spray pyrolysis. *Int. J. Appl. Inn. Eng. Man. (IJAIEEM)*, 3 (2014), 1–7.
13. T. L. Tan, C.W. Lai, S.B.A. Hamid, Tunable band gap energy of Mn-Doped ZnO nanoparticles using the coprecipitation technique, *J. Nanomater.* 2014 (2014) 1-6.
14. M.R. Arefi, S. Rezaei-Zarchi, Synthesis of zinc oxide nanoparticles and their effect on the compressive strength and setting time of self-compacted concrete paste as cementitious composites. *Int. J. Molecular Sci.* 13 (2012), 4340–4350.
15. M.I. Khalil, M.M. Al-Qunaibit, A.M. Al-zahem, J.P. Labis, Synthesis and characterization of ZnO nanoparticles by thermal decomposition of a curcumin zinc complex. *Arabian J. Chem.* 7 (2014) 1178–1184.
16. A. Bagabas, A. Alshammari, M.F. Aboud, H. Kosslick, Room-temperature synthesis of zinc oxide nanoparticles in different media and their application in cyanide photodegradation. *Nanoscal. Res. Lett.* 8 (2013), 516.
17. K. Prasad, A.K. Jha. ZnO Nanoparticles: Synthesis and adsorption study. *Natural Sci.* 1 (2009) 129–135.
18. M. Thirumavalavan, K.L. Huang, J.F. Lee, Preparation and morphology studies of nano zinc oxide obtained using native and modified chitosans. *Mater.* 6 (2013) 4198–4212.
19. P. K. Giri, S. Bhattacharyya, D.K. Singh, R. Kesavamoorthy, B.K. M. Panigrahi, Nair Correlation between microstructure and optical properties of ZnO nanostructures synthesized by ball milling, *J. Appl. Phys.* 102 (2007) 0935151.
20. A. V. Fonoberov, A. A. Balandin, ZnO quantum dots: Physical properties and Optoelectronic applications, *J. Nanoelectro. Optoelectro.* 1 (2006) 19.
21. F. J. Manjon, B. Mari, J. Serrano, A. H. Romero, Silent Raman modes in zinc oxide and related nitrides, *Chem. Rev.* 43 (2008) 33-47.
22. M. Tzolov, N. Tzenov, D. Dimova-Malinovska, M. Kalitzova, C. Pizzuto, G Vitali, G Zollo, I. Ivanov, *Thin Sol. Film.* 379 (2000) 396.
23. J. Mu, Z. Guo, H Che, H, Electrospinning of C-doped ZnO nanofibers with high visible-light photocatalytic activity, *J. Sol-gel Sci. Technol*, 78 (2016) 3925.
24. M. Tzolov, N. Tzenov, D. Dimova-Malinovska, M. Kalitzova, C. Pizzuto, G. Vitali, G. Zollo, I. Ivanov, *Thin Solid. Film.* 396 (2001) 274.
25. Y. Kumar, A. Sahai, Sion F. Olive Mendez, N. Goswami, V. Argarwal, Morphological transformation in cobalt doped zinc oxide nanostructures: effect of doping concentration, *Ceramics Int.* 42 (2016) 5184.

26. N. Goswami, A. Sahai, Structural transformation in nickel doped zinc oxide nanostructures, *Mater. Res. Bull.*, 48 (2013) 346.
27. F. Kayaci, S. Vempati, I. Donmez, N. Biyikli, T. Uyar, Role of zinc interstitials and oxygen vacancies of ZnO in photocatalysis: a bottom-up approach to control defect density, *Nanoscal.* 6 (2014) 10224.
28. Y. Qiu, H. Fan, G. Tan, M. Yang, X. Yang, S. Yang, Effect of nitrogen doping on the photo-catalytic properties of nitrogen doped ZnO tetrapods, *Mater. Lett.* 131 (2014) 64–66.
29. D. Zhang, M. Wang, J. Ma, G. Han, S. Li, Enhanced photocatalytic ability from carbon-doped ZnO photo-catalyst synthesized without an external carbon precursor, *F. Mater. Lett.* 7 (2014) 1-7.

CHAPTER 5

CONCLUSIONS AND RECOMMENDATIONS

5.1. SPRAY PYROLYSIS

In conclusion, this study has employed a spray pyrolysis method, more particularly, pneumatic spray pyrolysis method for fabricating ZnO nanoparticles. The system consist of a PSP vessel, pneumatic pump, furnace and substrate holder. The system operates at standard atmosphere pressures without the need of a clean room facility. Furthermore, the method of fabricating ZnO NPs using PSP technique has presented a cheap, economical, easy to operate and efficient fabrication of ZnO NPs and is capable of industrial scaling. Additionally, the PSP technique provides a relatively simple low cost way to introduce non-metal dopants at ratio required through the proportions of the precursor solutions. Using the PSP technique, we have fabricated un-doped and C-ZnO NPs for solar cell application.

5.2. X-RAY DIFFRACTION (XRD) ANALYSIS

The un-doped and C-ZnO nanoparticles have been synthesized by a cost effective chemical spray pyrolysis technique. The XRD analysis of the synthesized un-doped and C-ZnO nanopowders revealed peaks at 31.90° , 34.50° , 36.34° , 47.73° , 56.88° , 63.04° , 68.20° , and 77.33° . The XRD peaks are indexed (100), (002), (101), (102), (110), (103), (200), and (112) respectively, belonging to the hexagonal Wurtzite structure of ZnO. The XRD diffractograms of the C-ZnO NPs have also revealed additional peaks that are indexed as (004) and (202) which were due to the incorporation of carbon in the ZnO matrix. XRD analysis has shown an increase in nanoparticle size with increase in TBA concertation. Additionally, XRD analysis have revealed peak shift to higher 2θ values which is indicative of substitutional carbon doping.

5.3. SCANNING ELECTRON MICROSCOPY (SEM)

SEM analysis has revealed that the as PSP synthesized ZnO NPs consist of spherical shaped nanoparticles with uneven grain size distribution. The un-doped ZnO NPs consist of a mesoporous morphology with a multiple porous net-work structure. Moreover, SEM analysis has revealed the change in surface morphology with the introduction of carbon. This was

evidenced by increase in particle size and agglomeration with increase in carbon dopant levels. Introduction of carbon in ZnO lattice resulted in a loss of the mesoporous morphology and formation of a dense well packed structure. In conclusion, we can safely say that introduction of carbon in ZnO samples resulted in change in surface morphology of as prepared ZnO samples. Compaction and impurity contamination of the as PSP fabricated ZnO NPs was examined using energy dispersive X-ray (EDX) spectroscopy. The EDX analysis has revealed the presence of Zn, O and C in the EDX spectra. This confirms the successful pyrolysis of the ZnO precursor to form ZnO and C-ZnO NPs. The PSP fabricated samples consist of Zn and O atoms with additional Al impurity from substrate holder.

5.4. HIGH RESOLUTION TRANSMISSION ELECTRON MICROSCOPE (HRTEM)

The HRTEM analysis has revealed that the synthesized ZnO nanoparticles are spherical in shape. The analysis has also revealed that the ZnO nanoparticles synthesized by PSP have a particle size range of 6.65 – 14.21 nm. HRTEM analysis has also revealed an increase in particle size with increase in TBA concentration. The particle size estimated using HRTEM is in close agreement from those calculated using Scherer equation from XRD data. Moreover, the HRTEM analyses have shown that the lattice fringe separation for the un-doped and C-ZnO are 0.24 nm, 0.26 nm and 0.28 nm which corresponds to main diffraction (reflection) planes of Miller indices (101), (002) and (001) in the ZnO, respectively. Additionally, the results shown by HRTEM images of the un-doped and carbon doped ZnO samples were in agreement with the SEM micrographs in confirming the morphology of the ZnO nanoparticles. Furthermore, the selected area electron diffraction (SAED) of all the synthesized ZnO samples revealed the hexagonal pattern of sharp spots which indicates that the synthesized samples have crystalline Wurtzite ZnO structure. In conclusion HRTEM and SEM have confirmed the presents of spherical ZnO NPs. Additionally, HRTEM and XRD have confirmed that PSP fabricated ZnO has a hexagonal Wurtzite ZnO structure.

5.5. RAMAN SPECTROSCOPY ANALYSIS

The Raman spectroscopy analysis revealed that the PSP fabricated ZnO NPs have a prominent peak at 438.63 cm^{-1} , 434.42 cm^{-1} , 434.36 cm^{-1} , 434.76 cm^{-1} , 434.37 cm^{-1} and 433.65 cm^{-1} for un-doped, 0.005 M, 0.01 M, 0.015M, 0.02M and 0.025M C-ZnO, respectively, which is the characteristic peak of the Raman-active dominant $E_2^{(2)}$ (*high*) mode of Wurtzite ZnO. The

$E_2^{(2)}$ (*high*) mode of the un-doped has been blue shifted as compared to that found in bulk ZnO sample which is at 437 cm^{-1} . Moreover, the $E_2^{(2)}$ (*high*) mode of the C-ZnO samples has been red shifted compared to that of the un-doped sample which is probable due to the incorporation of C in the ZnO matrix. The incorporation of C in the ZnO lattice has an effect on the original structure of ZnO, which is in mutual agreement with the SEM results that showed the change in morphology as the dopant level changes.

5.6. UV-VISIBLE SPECTROSCOPY

UV-Visible spectroscopy has shown that the synthesized ZnO nanoparticles revealed that un-doped ZnO with modal nanoparticle size of 9.9 nm have an absorption edge at 374 nm and energy band gap of 3.31 eV, which is larger than for bulk ZnO nanoparticle with an absorption edge at 388 nm and an energy band gap of 3.2 eV. UV-Vis spec has revealed a blue shift in the energy band gap of PSP synthesized samples as compared to bulk ZnO. The absorption edge of the C-ZnO revealed a red shift in band gap energies that can be attributed the doping effect. The red shift in absorption properties for the PSP synthesized sample has been attributed to increase in particle size (as evidenced from XRD and HRTEM analysis). In conclusion, UV-Vis spectroscopy has shown a blue shift with increase in carbon dopant for the PSP synthesized samples.

5.7. RECOMMENDATIONS

The SEM has revealed the synthesized un-doped ZnO, 0.005 M C-ZnO, 0.01 M C-ZnO, 0.015 M C-ZnO has mesoporous morphology which is good for solar cell applications. The average particles size of the ZnO nanoparticles as revealed by XRD and TEM analysis is less than 40 nm and this indicates clearly that the ZnO nanoparticles are highly crystalline with hexagonal Wurtzite structure. Additionally, the Raman spectroscopy has revealed dominant $E_2^{(2)}$ (*high*) mode of Wurtzite ZnO. The UV-Vis DRS spectroscopy has revealed slight shift in absorbance. However we would like to point out for these samples to be effective materials for solar cell electrodes, there is a need to increase the nanoparticle size to above 25 nm. This can be achieved by increasing the concentration of the precursor solution to above 0.1 M.

APPENDIX A

RESEARCH OUTPUTS

The appendix presents the research outputs of the candidate which includes local oral presentations in local conferences, poster presentations as well as future conferences that are going to be attended.

A.1. LOCAL CONFERENCES

The candidate attended and presented at the following conferences:

1. L Ntozakhe, D Katwire, R Taziwa and E Meyer (2016), effect of carbon doping on the structural, optical and electronic properties of zinc oxide nanoparticles synthesized by Pneumatic spray pyrolysis technique, SAIP conference, 61st annual conference of the South Africa Institute of Physics at University of Cape Town in July 2016. (04 – 08 July 2016, Poster presentation).
2. L Ntozakhe, D Katwire, R Taziwa and E Meyer (2016), Combined confocal Raman and AFM characterization of ZnO nanoparticles synthesized by pneumatic spray pyrolysis technique, Renewable and sustainable energy symposium conference at University of Fort Hare (04 – 06 September 2016, Oral presentation).

A.2. LIST OF PUBLICATIONS

1. L Ntozakhe, D Katwire, R Taziwa and E Meyer (2016), Effect of carbon doping on the structural, optical and electronic properties of zinc oxide nanoparticles synthesized by Pneumatic spray pyrolysis technique.
2. R Taziwa, L Ntozakhe, E Meyer, and D Katwire (2016), Combined confocal Raman and AFM characterization of ZnO nanoparticles synthesized by pneumatic spray pyrolysis technique.
3. D Katwire L Ntozakhe, R Taziwa and E Meyer (2016), Design and optimization of PSP for fabrication of ZnO photo electrodes for solar cell application.
4. E Meyer, R Taziwa, L Ntozakhe, D Katwire, and (2016), Structural, morphological and Raman scattering studies of carbon doped ZnO nanoparticles fabricated by pneumatic spray pyrolysis technique.

A.3. MANUSCRIPT IN PROGRESS IN PEER REVIEWED JOURNALS

1. L Ntozakhe, D Katwire, R Taziwa and E Meyer (2016), Thin solid films, Effect of carbon doping on the structural, optical and electronic properties of zinc oxide nanoparticles synthesized by Pneumatic spray pyrolysis technique.
2. E Meyer, R Taziwa, L Ntozakhe, D Katwire, and (2016), Journal of Nanomaterials, Structural, morphological and Raman scattering studies of carbon doped ZnO nanoparticles fabricated by pneumatic spray pyrolysis technique.

A.4. GENERAL PRESENTATIONS

1. Chemistry Department series proposal presentations: Synthesis of modified ZnO nanoparticles using pneumatic spray pyrolysis for solar cell application 2015
2. Chemistry Department series progress report: Effect of carbon doping on the structural, optical and electronic properties of zinc oxide nanoparticles synthesized by Pneumatic spray pyrolysis technique 2016
3. FHIT department seminar series: Combined confocal Raman and AFM characterization of ZnO nanoparticles synthesized by pneumatic spray pyrolysis technique

A.5. ACCEPTED ABSTRACTS

Contribution ID : 181

Effect of carbon doping on the structural, optical and electronic properties of zinc oxide nanoparticles synthesized by pneumatic spray pyrolysis technique.

Wednesday 06 Jul 2016 at 16:10 (01h50')

Abstract :

This work reveals the effect of doping on the structural, optical and electronic properties of zinc oxide nanoparticles synthesized by pneumatic spray pyrolysis technique (PSP) using zinc ethoxide as the precursor. The prepared samples were characterized by XRD, HRTEM, SEM-EDX, UV-Vis spectroscopy, Four point probe (I-V characterization) and Combined Confocal Raman & AFM spectroscopy. Raman spectroscopy (RS) analysis has revealed that the un-doped ZnO and doped ZnO samples have a characteristic Raman optic modes at 325 per cm, 373 per cm, and 432 per cm belonging to wurtzite ZnO structure. The XRD patterns of un-doped and doped ZnO also exhibited the characteristic peaks of hexagonal wurtzite structure. The incorporation of Carbon species into ZnO lattice has been cross examined by monitoring the peaks positions of the (100), (002) and (001) planes. These three main peaks of Carbon doped ZnO NPs show a peak shift to higher 2 theta degrees values which indicates substitutional doping in zinc oxide samples. XRD analysis has revealed that the PSP synthesized nano particles have particles sizes ranging from 9.60 nm for Undoped to 9.96 nm for 0.015M C-ZnO samples. EDAX spectra of both undoped and doped ZnO nanoparticles have revealed prominent peaks at 0.51 keV, 1.01 keV, 1.49 keV, 8.87 keV and 9.86 keV. Peaks at X-ray energies of 0.51 keV and 1.01 keV respectively represent the emissions from the K-shell of oxygen and L-shell of Zinc. The occurrence of these peaks in the EDAX endorses the existence of Zn and O atoms in the PSP prepared samples.

OA5-22: Correlative Confocal Raman-AFM characterization of ZnO nanoparticles synthesized by pneumatic spray pyrolysis technique for solar cell application (M)

L Ntozakhe^{1,2}, R Taziwa^{1,2}, E Meyer¹, and D Katwire²

¹Fort Hare Institute of Technology, University of Fort Hare, Alice

²Chemistry Department, University of Fort Hare, Alice

Abstract: ZnO is a transparent semiconductor and can be used as transparent semiconducting oxide in solar cell devices. Optical & structural properties of modified ZnO closely depend on crystallite size, morphology, defects, and the presents of dopants. To realize the use of ZnO in solar cells, it is vital to investigate changes in the nanomaterial properties due to doping. Furthermore understanding the optical phonon spectrum change in Wurtzite nanoparticles is important because phonons affect the light emission and absorption properties of ZnO nanoparticles (NPs). Here we present a comparative combined confocal Raman-AFM optical and structural properties of modified ZnO NPs fabricated by spray pyrolysis (SP). The structural, morphological and optical properties of the SP synthesized ZnO NPs have been additionally scrutinized by SEM, XRD, TEM and UV-Vis spectroscopy. SEM analysis revealed that the morphology and shape of NPs change with increase in dopant levels. XRD spectra has revealed sharp and intense peaks at 31.90°, 34.50°, and 36.34° indexed (100), (002), and (101), respectively which shows characteristic peaks of hexagonal Wurtzite ZnO structure with particle size range of 9.60–15 nm. Raman Spectroscopy analysis has revealed that the ZnO samples have characteristic Raman modes at 325 cm⁻¹, 373 cm⁻¹, and 432 cm⁻¹ belonging to Wurtzite ZnO structure.

Keywords: ZnO, Spray pyrolysis, Confocal Raman, doping level

Structural, morphological and Raman scattering studies of carbon doped ZnO nanoparticles fabricated by pneumatic spray pyrolysis technique.

Summary :

Abstract

Zinc oxide (ZnO) nanoparticles (NPs) were prepared by pneumatic spray pyrolysis technique (PSP) using zinc ethoxide as a precursor and tetrabutylammonium as a dopant. The morphological, structural and optical properties of PSP synthesized NPs were evaluated using SEM, XRD, HRTEM, RS and UV-Vis spectroscopy. SEM analysis has revealed the formation of spherical shaped ZnO NPs. XRD analysis has revealed the peaks belonging to hexagonal Wurtzite ZnO crystal structure. HRTEM analysis has shown the presence of spherical NPs with a NP size of range of 8.65-13.79 nm. RS analysis has shown prominent peaks at 434 cm^{-1} which is the characteristic peak of $E_2^{(2)}$ (high) mode of the Wurtzite ZnO and it has been red shifted by 4 cm^{-1} , as compared to that of the bulk ZnO. The obtained results can be used for identification of phonons in Raman spectra of C-ZnO NPs.

Keywords: Zinc Oxide, Pneumatic Spray Pyrolysis, Raman Spectroscopy

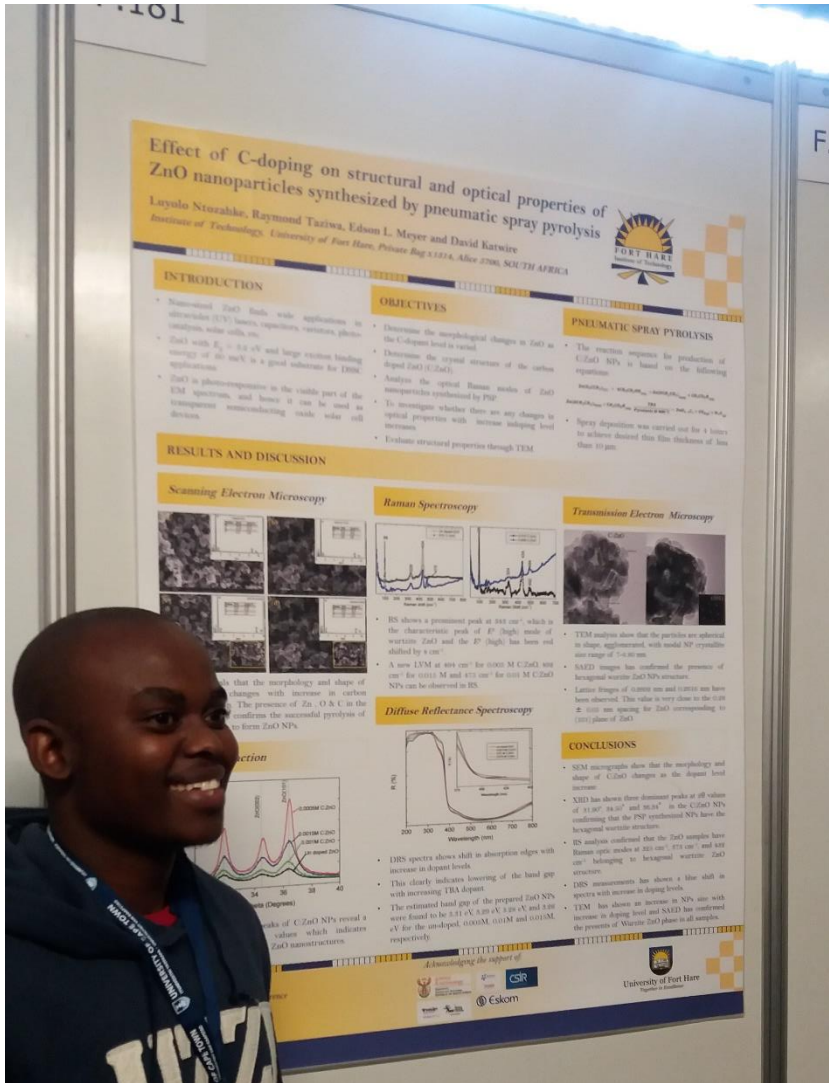


Figure #: A poster that was presented at 61st SAIP annual conference at University of Cape Town in July 2016